THE ACCURATE ULTRASONIC MEASUREMENT OF THE VOLUME FLOW OF BLOOD BY TIME DOMAIN CORRELATION

BY

PAUL MICHAEL EMBREE

B.S., Lehigh University, 1981
M.S., University of Illinois, 1982

THESIS

Submitted in partial fulfillment of the requirements
for the degree Doctor of Philosophy in Electrical Engineering
in the Graduate College of the
University of Illinois at Urbana-Champaign, 1986

Urbana, Illinois

THE ACCURATE ULTRASONIC MEASUREMENT OF THE VOLUME FLOW OF BLOOD BY TIME DOMAIN CORRELATION

Paul Michael Embree, Ph.D.
Department of Electrical and Computer Engineering
University of Illinois at Urbana-Champaign, 1986
William D. O'Brien, Jr., Ph.D., Advisor

A new ultrasonic flow measurement method employing time domain correlation of consecutive pairs of echoes has been developed. An ultrasonic data acquisition system determines the time shift between a pair of range gated echoes by searching for the time shift with the maximum correlation between the RF sampled waveforms. This shift indicates the distance a group of scatterers has moved between pulses. Because the time between pulses is known, the velocity estimate is accurate and self calibrating.

Experiments with a 5 MHz transducer indicate that the standard deviation of the estimate of steady fluid velocity through 6 mm diameter tubes is less than 10% of the mean when the signal-to-noise ratio is 20 dB. Flow rates from 50 to 500 ml/min have been measured with an accuracy better than 10%. Experiments which verify that the time domain correlation method works with whole blood have been completed. The 2-D velocity field is estimated by slowly sweeping the ultrasonic beam across the blood vessel phantom. Total volume flow through the vessel is estimated from the 2-D velocity field. This volume flow estimate is then compared to accurate hydrodynamic flow measurements in order to determine the overall experimental accuracy of the time domain method.

UNIVERSITY OF ILLINOIS AT URBANA-CHAMPAIGN

THE GRADUATE COLLEGE

APRIL 1986

WE HEREBY RECOMMEND THAT THE THESIS BY

PAUL MICHAEL EMBREE

ENTITLED THE ACCURATE ULTRASONIC MEASUREMENT OF THE VOLUME FLOW OF BLOOD BY TIME DOMAIN CORRELATION

BE ACCEPTED IN PARTIAL FULFILLMENT OF THE REQUIREMENTS FOR

THE DEGREE OF DOCTOR OF PHILOSOPHY

William D. O'Brien, Jr. Director of Thesis Research

Timothy N. Trick Head of Department

Committee on Final Examination†

William D. O'Brien, Jr. Chairperson

Charles A Cain

W. Kenneth Jenkins

† Required for doctor's degree but not for master's.

O-517

ACKNOWLEDGEMENTS

I would like to most gratefully thank my advisor, Professor William D. O'Brien, for pointing me toward this project, for providing insight and encouragement (and funding), and for his patience in this entire matter.

I gratefully acknowledge the assistance of Bob Cicone, Wanda Elliott, Billy McNeill, Joe Cobb and Professor M. E. Clark in the technical aspects.

TABLE OF CONTENTS

CHAPTER 1

INTRODUCTION AND BACKGROUND

1.1 INTRODUCTION

The measurement of human blood flow by ultrasonic means has proved to be a valuable tool for clinical diagnosis of vascular disease. Unfortunately, current Doppler based measurement techniques are plagued with practical as well as theoretical difficulties which result in inaccurate and imprecise flow measurements.

Doppler blood flow measurement has been well researched from a practical [1-7] as well as a theoretical [8-10] point of view. Unfortunately, the Doppler frequency shift of high frequency ultrasound (typically 7.5 MHz is used clinically) is rather small and hard to measure with useful accuracy. While most investigators have studied the Doppler techniques which were originally used in radar systems [11], another group has chosen to use high speed time domain correlation techniques [12]. Briefly, the time domain correlation technique correlates two successive echoes at a particular range distance from the transducer. The time shift where the maximum correlation occurs is used to determine the distance a section of blood scatterers has moved between the two echoes.

Some important clarifications in terminolgy are in order at this point. Flow is a term with many definitions. In this thesis, the term volume flow will be used to distinguish flow from flow velocity. Volume flow is the volume of a fluid passing through a given area per unit time. Normally, the area of the confining vessel or tube is used in the flow calculation. The term flow velocity will be reserved for measurements where the direction of the vector quantity, velocity, is important. Thus, axial flow velocity (or just axial velocity) is the component of the flow velocity along the axis of the ultrasound beam. Axial velocity is the velocity which can be measured by most ultrasonic flow measurement techniques including pulsed Doppler and the time domain technique described herein.

Other often confused concepts are accuracy, uncertainty, and precision. Accuracy is a comparison of a measured quantity to the true value obtained from a standard unquestioned experiment. For example, in this research the ultrasonic determination of volume flow will be compared to a highly accurate and independent determination of volume flow, namely, measuring the time required to fill a known volume. Since relatively long times (> 60 s) and large volumes (0.25 liters) can be measured very accurately (within 1%), this hydrodynamic flow measurement is used for the standard reference or true value.

Numerical definitions of accuracy also vary. Experimental inaccuracy (often called error) is often expressed as $X \pm D$ where X is the measured value and D is the "maximum difference" from the measurement and the true value. Since any measurement is subject to random variations with some probability density function, a "maximum difference" is not a quantitative measure of accuracy unless the probability of the exact value being outside the ± D limits is zero. In this thesis, accuracy expressed as X ± D will imply that ± D is the 95% confidence limits of the measurement. For normally distributed measurement populations, D is approximately two standard deviations. Thus, a stop watch time measurement of 60.0 ± 0.5 seconds implies that 95% of the time the stop watch measurement is accurate to within 0.5 seconds. Another way to express accuracy is as a percent deviation from the true value, that is, "accurate to within 0.83% of 60 seconds." Once again, the deviation must be expressed as a confidence limit; a 95% confidence limit is used in this thesis.

The concept of uncertainty is the degree of unpredictablity or lack of confidence in a particular measurement. Uncertainty is also closely related to accuracy in the sense that accuracy is also a way of expressing the confidence of a measurement. Uncertainty will be expressed in the same way as accuracy (X ± D) where D is the 95% confidence interval. The uncertainty of a measurement process is often estimated from a knowledge of the experimental method or skill of the person making the measurement. The accuracy of an experiment is often estimated from the uncertainties of the various measurements needed to obtain an experimental result. The experimental results reported herein are dependent on the uncertainties of the fundamental measurements of time, volume, and distance.

Precision is the extent to which a given set of measurements of a quantity agree with their mean. It is a measure of the repeatability, spread, or variation of the quantity measured. An estimate of the precision of a measurement can be obtained by simply repeating the experiment a number of times and examining the results. In order to quantify precision it is defined numerically as the ratio of the estimate of the standard deviation to the mean of the set of measurements. This ratio will be expressed in percent for convenience. Other authors [10] have called this ratio the "relative standard deviation" and expressed it as a fraction. In both cases, better precision corresponds to a lower number and higher imprecision corresponds to a higher number.

The previous work by Foster [12] considered the one dimensional measurement of flow along an ultrasonic beam passing through a vessel. The experimental and computer simulation results showed that precise estimates of the speed of the scatterers along the beam axis can be obtained. The experimental measurement of volume flow was acomplished by attempting to align the ultrasonic beam so that it passed directly through the center of the vessel. The flow profile was assumed to be parabolic in shape and axially symmetric. Considerable difficulty was encountered in determining the measurement angle and the position where the beam intersected the vessel. Both of these difficulties resulted in quite large experimental errors (greater than 20%) in the volume flow measurement.

This research continues the development of the time domain correlation method and investigates the measurement of the two dimensional flow profile in a blood vessel phantom. From these two dimensional measurements, an accurate volume flow estimate is determined.

1.2 BLOOD FLOW MEASUREMENT BACKGROUND

This section is intended to provide some background on the current Doppler flow measurement methods. No attempt has been made to provide a complete review of Doppler ultrasound or all of the limitations of Doppler flow measurement methods. More detailed reviews of Doppler flow measurement methods can be found in [1,2] as well as [12]. The first blood flow measurements were obtained by using a continuous ultrasound signal; such devices are called CW Doppler flow meters. The CW Doppler flow measurement method will be briefly described in the next section. The primary limitation of CW methods is that no velocity versus range information can be obtained. By using short bursts of ultrasound, pulsed Doppler flow measurement methods can be used to generate velocity versus range data. Pulsed Doppler methods will be considered in section 1.2.2.

1.2.1 CW Doppler

Continuous wave Doppler flowmeters use two transducers to measure the frequency shift in the scattered ultrasound signal. One transducer transmits continuous, single frequency ultrasonic energy, and the other transducer receives the energy scattered from the blood contained within the vessel as well as all other scatterers within the receive transducer's beam. The difference frequency between the received and the transmitted signal can be used to estimate the mean flow velocity [13-16]. Any moving scatterer in the ultrasound beam will have an influence on the received Doppler spectrum. Since the transducers are generally focused, the region of flow measurement is confined to a reasonably small area. This method of flow measurement is identical to moving target indication (MTI) methods used in radar systems [11] where the radar antenna directivity selects the moving target to be measured. Thus, all moving scatterers within the ultrasonic beam, regardless of range, influence the measured Doppler frequency shift. Since the range of the moving scatterer is unknown, flow versus range measurements are impossible.

Because a single frequency is transmitted, the frequency dependent attenuation of the intervening tissue will not affect the presence of a particular frequency component. The average flow across the vessel measured by CW Doppler is therefore unbiased due to the intervening tissue. However, transit time and beam size effects both bias the flow estimate [13]. Even with these difficulties, the shape of the mean flow estimate versus time from CW Doppler meters has been used to diagnose vascular system defects [1,2,20]. However, since the Doppler angle and blood vessel size are not measured, no quantitative flow information is available.

1.2.2 Pulsed Doppler

Early investigators used long ultrasonic pulses to measure the mean Doppler shift as a function of range [4-7]. Since the variance of the Doppler estimate increases with increasing bandwidth [10], long ultrasonic pulses were required to produce precise flow estimates. Unfortunately, the long pulse length also spatially averaged the flow profile and resulted in poor range resolution of the flow estimate. These pulsed Doppler devices typically consisted of one phase detection circuit for each range gate where the average flow velocity was estimated [5]. Such analog methods were limited to analog frequency domain methods. When inexpensive digital signal processors became available, much of the attention was directed to discrete time spectral estimation techniques [8-10].

Real time flow mapping systems using phased array sector scanners have recently become available [3]. An ultrasonic beam is swept rapidly across the image area. Each line in the sector image is divided into range cells and a flow velocity estimate is determined. The velocity estimate is determined from the Doppler spectrum by a simple autocorrelation technique. The spectral bandwidth and mean frequency of the Doppler spectrum are color coded and displayed with the gray scale image of the surrounding tissue. Flow toward the transducer is coded as red and flow away from the transducer is coded as blue. Since only the direction of the flow is displayed, no accurate flow rate information is provided by this system.

1.3 RESEARCH PURPOSE

The purpose of this research is twofold. First, the measurement of flow in one dimension along the beam axis will be refined and generalized in order to improve the precision of the time domain correlation method when a wide range of flow velocities is present. Second, a method will be developed to accurately measure the volume flow in a typical vessel. Flow measurement in a plane across the vessel will be used to determine the measurement angle and the total volume flow. The accuracy of this ultrasonic volume flow measurement method will be determined experimentally by comparison with independent hydrodynamic flow rate measurements.

Some of the theoretical and practical problems with pulsed Doppler ultrasound flow measurement are described in Chapter 2. The time domain correlation flow measurement technique is discussed in Chapter 3. The equipment and methods used in the flow measurement experiments are discussed in Chapters 4, 5, and 6. The experimental results, discussion and conclusions are presented in the remaining chapters.

CHAPTER 2

PULSED DOPPLER ULTRASOUND

This chapter is intended to provide background information about pulsed Doppler flow measurement and indicate some important drawbacks of Doppler frequency domain approaches to flow measurement. Considerable interest in blood flow imaging is indicated by the sophistication of blood flow measurement devices which have recently become available [3]. It is therefore important to understand and determine the quantitative limitations of Doppler flow measurement methods. The following discussion addresses the two primary limitations of Doppler blood flow measurement: accuracy and precision. In later chapters the accuracy and precision of the time domain correlation method will be compared to the values obtained for Doppler flow measurement.

One of the major accuracy problems with the current Doppler flow measurement techniques is that the volume flow is estimated, not measured [21]. The typical Doppler flowmeter measures the average flow velocity along the beam direction at a particular distance from the transducer. Both the blood vessel size and the measurement angle are unknown. The vessel size is estimated from a knowledge of an average size for the particular vessel being measured or by pulse-echo scanning methods [1,2]. Some researchers have suggested using two or more different measurement positions (by moving the transducer or by having more than one transducer) and thus determining the Doppler angle by using a number of range estimates of the peak flow [7,16]. Since arterial vessel walls are constantly moving (due to the pulsatile flow of blood), it is difficult to determine the position of the vessel at a given time. Also, since the paths for each measurement are different, the two measurements could have different biases due to different tissue effects. Since each patient has different size blood vessels and it is difficult to measure the Doppler angle with precision, quantitative comparisons between normal and abnormal flow are nearly impossible.

As shown in [10] the typical pulsed Doppler flow meter measures the mean frequency in the echo. The optimum correlation receiver method of Doppler flow measurement suggested in [31] measures the frequency of the component with the largest amplitude. In [31] a number of correlation receivers are shown to be the optimum Doppler frequency shift detector in the maximum likelihood sense. Other devices such as the zero crossing detector can be used to estimate the Doppler shift. For large signal-to-noise ratios the zero crossing detector has been shown to follow the root mean square frequency of the return echo [32]. Since most Doppler flow meters which are currently available measure the mean frequency in the received echo, the mean frequency will be considered in all simulations presented in this chapter.

The bias of the mean Doppler frequency estimate due to the frequency dependent attenuation of tissue will be used in the next section to demonstrate one accuracy limitation of Doppler flow velocity measurements. Section 2.2 addresses the other major limitation of Doppler flow measurement: precision. By reviewing several theoretical and experimental results presented in the literature, the precision of typical Doppler blood flow axial velocity measurements will be determined. The Doppler precision values obtained from the literature will be compared to the time domain correlation precision results in Chapter 7 (see section 7.1.4).

2.1 ERRORS INTRODUCED BY TISSUE ATTENUATION

Most current clinical blood flow measurement techniques are based on qualitative comparisons of measurements from the same patient [16-21]. This is primarily because the variation of the vascular system from patient to patient can be significant. The thickness and characteristics of the intervening tissue between the skin surface and the flow to be measured affects the accuracy of Doppler frequency estimate. Different tissues have different frequency dependent attenuations [22-29] and will therefore change the measurement of the mean frequency of the received echo which is used to estimate the Doppler shift [30]. The presence of more tissue between the transducer and the flowing blood in a particular patient may not only increase the variance of the Doppler frequency estimate (because of a lower signal-to-noise ratio due to a longer tissue path length) but may also bias the estimate in an unpredictable way. This is because the received ultrasonic echo spectrum can have a different power spectrum than that of the transmitted signal.

To determine the effect of frequency dependent attenuation on a Doppler flowmeter output, this simulation assumes that the flow meter measures the mean frequency of the ultrasonic backscattered signal. Gerzberg [33] has shown that the pulsed Doppler spectral estimate is biased due to a finite signal-to-noise ratio. In this simulation, it is also assumed that no noise is present in the received echo. For simplicity, the blood motion is modeled to be moving at a constant, uniform velocity toward the transducer. An approximation valid for long pulses ($M \geq 5$) of the spectrum of the pressure signal is given by [35],

$$T(f) = H(f)\ \mathrm{Sinc}\left(M \left(\frac{f}{f_o} - 1 \right) \right) \tag{1}$$

$$H(f) = \frac{f\ f_o}{Q \sqrt{(f^2 - f_o{}^2)^2 + (f\ f_o/Q)^2}} \tag{2}$$

where

$T(f)$ = spectrum of transmitted pressure waveform.
$H(f)$ = transducer second order transfer function.
$\mathrm{Sinc}(f)$ = $\sin(\pi f)/\pi f$.
M = number of cycles of center frequency excitation.
f_o= center frequency (Hz).
Q = transducer quality factor.

A typical transmitted signal spectrum ($T(f)$) with $M=5$ is shown in Figure 1. The magnitude in decibels is shown for a center frequency of 5 MHz. In this simulation the transducer is modeled as a second order bandpass filter with a Q of 3. This transmitted signal spectrum, T(f), will be used throughout the simulation to demonstrate the errors introduced by the tissue attenuation.

A suitable tissue model determined by several investigators [22-29] with CW measurements of many tissues is given by

$$\mathrm{atten}(f) = A_o\, f^b \tag{3}$$

where

atten(f) = attenuation of ultrasound as a function of frequency (dB).
A_o = attenuation in dB at 1 MHz (typically 0.5-2 dB).
f = frequency in MHz.
b = frequency independent constant (typically 1-1.4).

The distance traveled by the ultrasonic beam is included in A_o. If a_o is the attenuation coefficient (dB/cm, for example), then at 1 MHz A_o is $a_o d$ for a one way tissue path length d. The value of a_o for various materials varies from nearly zero for water to 1 dB/cm for some soft tissues [26-29]. For peripheral vascular blood flow measurements, the one way path length may be less than 1 cm. Thus, in many soft tissue cases, reasonable values of A_o are between 0.5 dB and 1.0 dB. The value of b varies from 1.0 to 1.4 for many soft tissues [27,28]. The magnitude of the pressure signal which is incident at the blood vessel is

$$B(f) = T(f)\ 10^{-\frac{\mathrm{atten}(f)}{20}} \qquad (4)$$

As the ultrasonic wave passes through the tissue the mean ultrasonic frequency is shifted. When the ultrasonic wave reaches the moving scatterers, each of the frequency components in the scattered waveform has been shifted according to the Doppler relation,

$$f_{scat} = f\ \left(1 - \frac{2\ V}{c} \right) \qquad (5)$$

where

f_{scat} = frequency backscattered by blood.
f = frequency incident on blood.
V = blood speed (positive is toward the transducer).
c = speed of sound in blood.

As the wave propagates back through the tissue, it is again attenuated according to equation (3). The transducer then filters the received pressure signal. The received electrical signal, R(f), is

$$R(f_{scat}) = H(f_{scat})\ B(f_{scat})\ 10^{-\frac{\mathrm{atten}(f_{scat})}{20}} \qquad (6)$$

The magnitude of each of these signals is shown in Figure 1 for $A_o = 1$ dB and $b = 1.4$. These values are typical for soft tissues (liver, for example) [27,28]. The axial flow velocity for this case is 10 m/s and $c = 1500$ m/s. For the case illustrated, the mean frequency which is incident at the scattering target is 4.933 MHz (see the curve labeled "AFTER

TISSUE FORWARD TRANSIT" in Figure 1). The tissue has caused a -66.67 kHz shift in the transmitted spectrum (mean 5.000 MHz). The Doppler shift caused by the 10 m/s scatterer motion in this case is -66.66 kHz as determined from equation (5). This shift is indicated in Figure 1 for the curve labeled "DOPPLER SHIFTED." During the reverse transit back to the transducer the tissue causes a further -66.65 kHz shift in the mean frequency of the ultrasonic signal (see the curve labeled "AFTER TISSUE REVERSE TRANSIT"). The received echo signal after the transducer filtering (see the curve labeled "RECEIVED SIGNAL") has a mean frequency shift of -153 kHz. Thus, a Doppler shift of -66.66 kHz results in a mean frequency shift of -153 kHz in the received echo signal. The example shown in Figure 1 illustrates the method used to simulate the effects of the tissue attenuation.

Figure 2 is a graph of the mean frequency shift of the received echoes for a 10 cycle transmitted pulse and b = 1.4. Three different A_o values ($A_o = 0.0, 0.5, 1.0$) are shown to illustrate the relationship between target velocity and mean frequency shift of the received echoes. This figure shows a linear relationship between frequency shift and target velocity. The bias for $A_o = 1.0$ is -40 kHz indicates a bias greater than the shift caused by an axial velocity of 6 m/s. At 5 MHz the shift without tissue effects for V = 6 m/s would be 40 kHz. The slopes of all of the frequency shift curves are equal and have a magnitude less than $2 f_o/c_o$, which is what would be expected from equation (5). This is caused by the slight filtering by the transducer (Q = 3) of the ultrasonic signal spectrum. After the frequency spectrum is Doppler shifted, the transducer filtering causes the mean received frequency to be closer to the center frequency of the transducer. Because of the transducer filtering, if the bandwidth of the excitation is large compared to the bandwidth of the transducer, the slope will approach $-f_o/c_o$. If the number of cycles is large compared to the Q of the transducer (ten or greater in this case), the slope is determined by equation (5). The bias of the frequency shift curve is determined by the tissue parameters.

Figure 3 shows the frequency shift of the received echo signal versus target velocity for three different b values (b = 1.0, 1.2, and 1.4). Ten cycles of excitation (M = 10) is simulated for $A_o = 0.5$. Again, a linear relationship with target velocity is shown. The bias of the mean frequency shift changes with the tissue paramenter b. The bias due to b = 1.0 is only -9 kHz and increases to -23 kHz for b = 1.4.

Figure 4 shows the bias of the mean frequency shift versus the number of cycles for three different A_o values with b = 1.4. The upper most curve for $A_o = 0.0$ indicates no bias when there are no tissue effects. The other two curves show the bias of the mean frequency shift for $A_o = 0.5$ and 1.0. The mean frequency bias of the received echoes decreases with decreasing A_o. Since the tissue path length is included in A_o, a shorter tissue path length will have a smaller mean frequency bias. Also, a larger number of transmitted cycles results in a smaller transmitted bandwidth resulting in a less severe mean frequency bias due to the tissue path.

Figure 5 shows the bias of the mean Doppler frequency estimate versus the number of cycles for b = 1.0, 1.2, and 1.4 with $A_o = 0.5$. For these cases, the bias due to the tissue decreases as the number of transmitted cycles increases and the transmitted bandwidth decreases. This is consistent with the CW case where a single frequency, zero bandwidth signal is used. Even when 20 cycles are used, the bias is still -4 kHz for $A_o = 0.5$ and b = 1.0.

These simulation results show that a large bias results when the mean Doppler frequency is used to estimate the blood flow velocity. Even if 20 cycles of the 5 MHz transmitted signal were used with $A_o = 0.5$ and b = 1.0, the bias in the mean frequency estimate would be -4 kHz. If the axial velocity was -2 m/s (a rather large blood velocity), then the Doppler shift would be 13.33 kHz. Because of the -4 kHz bias, the received echo signal would have a 9.33 kHz frequency shift. Thus, if the frequency shift of the received echoes were used to indicate an axial velocity of -2 m/s the resulting velocity estimate would be -1.4 m/s, assuming the tissue attenuation model given by equation (3). The poor accuracy of this example Doppler axial velocity measurement indicates the large error (30% in this case) in the Doppler flow velocity estimate which may be introduced by the frequency dependent attenuation of typical soft tissue.

2.2 DOPPLER ESTIMATE PRECISION

This section describes several theoretical and experimental results presented in the literature which indicate the precision of Doppler axial flow velocity measurements. Although most authors do not include information about the precision of Doppler flow measurements, one recent publication has addressed this issue exclusively [34]. For purposes of comparison with the time domain correlation method, the Doppler flow estimate precision will be defined as the precision of a flow estimate obtained from one received echo. The reported precision of a Doppler flow meter includes the averaging effect of the output lowpass filter or integrator. Proper comparison of Doppler results to the time domain correlation method requires compensation for the effect of these output filters. Often only the -3 dB frequency of analog filters is stated, making the modeling of the output filter difficult. Theoretical results [9,34] are easier to compare since the averaging time is usually stated. Other theoretical results [31] suggest a different approach to the measurement of the Doppler frequency by using a series of correlators.

The maximum correlation method suggested by Olinger [31] used a number of correlation receivers all set at different frequencies. The correlation receiver with the largest output was used to determine the most likely Doppler shift. Olinger shows that as the number of correlation receiver elements increases above an optimum number, the correlator with the maximum output was equally likely to be either of the adjacent frequencies. Olinger states that three correlators are a reasonable number for the typical transducer configuration. Thus, the flow rate was represented by three quantization levels.

Let the correlator set to the transmit frequency be correlator 0, the middle correlator set to a 1 kHz shift be correlator 1, and correlator 2 be set to a 2 kHz shift. Suppose the frequency shift to be measured was half way between the frequency of correlators 1 and 2. The correlator with the greatest output is equally likely to be correlator 1 or 2. The probability mass function for this case is 0, 0.5, 0.5 for correlators 0, 1, and 2 respectively. The mean flow velocity measured by the levels is 1.5 as desired. The variance is 0.25 for this simple example. The precision of this discrete flow estimate is therefore 33%. This theoretical result for an optimum bank of correlators indicates the approximate precision of the best Doppler blood flow measurement methods.

Angelsen and others have published results concerning the precision of the Doppler flow estimate. The continuous time estimators of the mean frequency of a pulsed Doppler spectrum are considered in [10] and discrete time methods are considered in [9,34]. In both cases, the output of the mean Doppler frequency estimator is low-pass filtered before the standard deviation is calculated. For a typical case in [10] with a low-pass filter with two poles at 20 Hz and a parabolic flow profile, the theoretical precision is 9%. Experimental data in [10] show the precision was 11% for the same conditions. The discrete time implementation using a single pole 15 Hz low-pass filter [9] has a theoretical precision of approximately 10% for Doppler shifts greater than 600 Hz. Several theoretical mean frequency estimators are compared in [34]. Fifty outputs of all these estimators are averaged together. The precision of all the estimates is 10-12% for a 10 dB signal-to-noise ratio. In all cases compared, a pulse repetition frequency of 4000 Hz was chosen and the angle between the ultrasonic beam and the flow was 45^{o}. A large number of Doppler frequency estimates are averaged together to obtain the given precision. An approximate expression of the averaging time caused by a first order low-pass filter is [35],

$$T_{ave} = \frac{2}{\pi f_3} \tag{7}$$

where f_3 is the cutoff frequency (Hz) of the filter. Filters of higher order have a longer averaging time, so this is an optimistic estimate of the averaging time. Because the received echoes are known to be approximately Gaussian, the output of the Doppler flow meter can be considered Gaussian [10]. Since the flow rate being considered in this comparison is constant over the measurement time interval, the Doppler flow meter output can also be assumed to be a wide sense stationary process [10]. The standard deviation of the output of the filter is reduced by the factor $1/\sqrt{M}$ where M is the number of input samples averaged together by the filter.

The three cases indicated above [9,10,34] can now be compared to other flow measurement methods by determining the standard deviation of the unfiltered flow estimate. The results are shown in Table 1.

Table 1 - Doppler Flow Estimate Precision.

Case	Precision Reported (%)	Filter Cutoff (Hz)	Average Time (sec)	Number Averaged (M)	Unfiltered Precision (%)
Theory [10]	9	16	0.04	170	117
Experiment [10]	11	20	0.03	127	124
Discrete Theory [9]	10	15	0.04	170	130
Discrete Theory [34]	12	51	0.01	50	85

The best unfiltered Doppler precision listed in Table 1 for a discrete theoretical result [34] is 85%. This result did not include the effects of velocity gradients in the analysis. The other results [9,10] did include some velocity gradient effects in the Doppler flow estimate precision. Since a range of axial flow velocities is present in a typical flow measurement region, the precision values for the other three cases shown in Table 1 are considerably larger (117 to 130%) and may be more typical of Doppler blood flow measurement.

In summary, the approximate unfiltered precision of typical Doppler axial flow velocity measurements has been determined for theoretical and experimental cases published in the literature. The unfiltered precision is the precision of consecutive Doppler frequency shift estimates obtained from each echo. The unfiltered precision of Doppler will be compared to the precision of the time domain correlation method in Chapter 7 (section 7.1.4).

CHAPTER 3

TIME DOMAIN FLOW MEASUREMENT

3.1 TIME DOMAIN CORRELATION

The measurement of distance by the time of arrival of electromagnetic energy has been used in radar for many applications [11]. Early radar systems used a threshold detector to indicate the position of a target on the radar screen. Later in the development of radar, optimal time domain correlation or "matched filtering" was suggested as the best way to estimate the time of arrival of the radar pulse [11]. If a radar antenna is made to track a target (as it is in fire control radar [11]), the change in the time of arrival of the received echoes can be used to determine the axial velocity of the target. The essence of the time domain flow measurement technique is to track scatterers within an ultrasonic beam and determine how far they move by the time shift between the echoes.

Because the ultrasonic beam is fixed in space and can not follow the flow, the time domain method requires that the time between echoes must be made sufficiently small so that most of the scatterers stay within the beam and the correlation between the two echoes remains high. The time shift between one echo and the next can therefore be estimated by searching for the time shift which yields the maximum correlation. The time domain correlation method estimates the time shift between two successive echoes in order to determine the amount the scatterers have moved during the time between the two echoes.

Other investigators [36] have suggested using time domain correlation to measure flow. However, their work used two different transducers separated by a small distance along the tube. Although the technique used in [36] was shown to have an accuracy of ± 2% when relatively fast slurry flow was being measured, it would be difficult to physically displace two identical transducers by a small enough amount (1-5 mm) in order to still have a high correlation between the two received signals from the slow blood flow in veins and the smaller arteries. Also, blood vessels are not straight, resulting in different angular positions that the two beams would intersect the vessel.

This section discusses the time domain correlation method by using a set of ultrasonic measurements to illustrate the time domain correlation method. Further details of the time domain correlation method and simulation results illustrating many of the concepts described in this chapter can be found in the previous work [12].

Figure 6 shows three consecutive ultrasonic echoes measured using a 5 MHz transducer directed at a 6 mm diameter dialysis tube containing flowing water and Sephadex^R. The time between these echoes was 0.384 ms (PRF=2604 Hz) and the angle between the ultrasonic beam and the flow velocity was approximately 45^o. The one way path length traveled by the ultrasonic beam from the front wall to the back wall was approximately 8.5 mm. The round trip time for the ultrasonic wave to travel across the tube was approximately 13 μs as indicated in Figure 6 by the length of the received ultrasonic signal. Careful examination of these echoes reveals that the echoes look very similar. Also, the center sections of the echoes appear to move to the right slightly and echo sections near the wall positions do not move.

The lower portion of Figure 6 illustrates the time domain correlation method used to determine the amount of motion in three 0.8 μs range gated sections of the three echoes. The discrete time correlation between two zero mean echo sections, $e_1(n)$ and $e_2(n)$ is given by

$$\rho(s) = \frac{\sum_{i=0}^{N-1} e_1(r+i)\, e_2(r+i+s)}{\sqrt{\sum_{j=0}^{N-1} [\, e_1(r+j)\,]^2 \quad \sum_{k=0}^{N-1} [\, e_2(r+k+s)\,]^2}} \qquad (8)$$

where

s = shift between echoes (samples).
r = range to beginning of section to be measured (samples).
$\rho(s)$ = correlation between echoes (-1 to 1).
N = correlation length.

Each pair of the echo sections is correlated resulting in the nine sample correlation functions shown. In the sample correlation functions shown in Figure 6, the correlation length was 40 samples. The sampling rate was 50 MHz so that 40 samples corresponds to 4 wavelengths at 5 MHz. The work by Foster [12] indicated that this correlation length is a good compromise between range resolution and measurement precision.

As the correlation examples in Figure 6 show, the maximum correlation of the center section of the echo is at a positive time shift. This corresponds to flow velocity away from the transducer. The correlation peak between echo 1 and echo 3 is at a shift which is twice that of echo 1 and echo 2. The other two correlation examples for echo sections near the tube walls show less shift, as expected. The proposition introduced in [12] is that the velocity of the flowing fluid is given by

$$V = \frac{E[smax]\ c}{2\ T\ \cos(\Theta)} \tag{9}$$

where
V = magnitude of the velocity of the scatterer at a particular range.
smax = time shift with maximum correlation.
E[smax] = expected value (mean) of time shift.
T = time interval between the transmitted pulses.
c = speed of sound in the scattering fluid.
Θ = angle between sound beam and velocity vector (measurement angle).

Since the time domain correlation method compares two successive echoes which have both passed through the same intervening tissue, frequency dependent attenuation of the tissue path will not affect the mean flow measurement. Considering the effects on the frequency spectrum due to typical tissues, this is a major advantage of the time domain correlation technique. Thus, the average time shift determined by time domain correlation is unbiased by the frequency response of the tissue. This will be shown in the next section along with the derivation of the variance of the time domain correlation method.

3.2 PRECISION OF TIME DOMAIN CORRELATION METHOD

Foster's work [12] measured the precision of the time domain correlation flow estimates experimentally for a particular transducer configuation. These experimental precision values illustrate the importance of understanding the factors which influence the variance of the time domain correlation flow estimates. Table 2, which was adapted from a graph in [12], shows the effect of changing the time between echoes:

Table 2 - Precision and Relative Variance for a 5 MHz Transducer Measuring Buttermilk Flow at a 45° Measurement Angle (adapted from [12]).

Shift (wavelengths)	Precision (%)	Relative Variance
0.125	12	5.8
0.250	10	4.0
0.375	8	2.6
0.500	6	1.4
0.625	5	1.0
0.750	5	1.0
0.875	7	2.0
1.000	10	4.0
>1.000	>10	>4.0

The first column shows the shift in wavelengths between the two consecutive echoes. The same midstream velocity was used in order to minimize the other errors due to the finite beam size and the flow velocity gradient in the experimental measurement. The data shown in Table 2 were obtained with a 5 MHz transducer having a beamwidth of 2 wavelengths at the focal point (49 mm from the transducer front surface). The relative variance versus shift curve depends on the transducer beamwidth and the measurement angle (45° for the above data). For each shift, the pulse repetition rate was changed until the mean shift was the value shown. The precision of the time shift (the second column) was then calculated from the standard deviation and mean time shift values obtained from the graph in [12]. The last column shows the variance of the estimate relative to the minimum precision (5% at 0.625 wavelengths). Each precision value was divided by 5% and then squared to obtain the relative variance values. More detailed measurements of the experimental precision of the time domain correlation method are presented in Chapter 7. Although experimental results can show trends in the measurement precision, it is difficult to establish the relationship between the parameters which change the precision value.

The remainder of this section is a theoretical derivation of the precision of the time domain correlation method. By making certain approximations about the statistical properties of the ultrasonic echoes, a relationship is established between the measurement precision and the transducer characteristics, measurement angle and signal-to-noise ratio.

This derivation of the precision of the time domain method is almost identical to the derivation of the time of arrival of a radar signal presented by Helstrom [37]. A similar radar result was also found by Woodward [38]. The overall assumption in this derivation is that the signal level is large compared to the noise level. The precision derivation assumes that the correlation length is infinite and that the correlation peak can be estimated from a continuous correlation estimate. Many of the simulation results in [12] addressed the validity of these assumptions and showed that a four wavelength long discrete correlation had little additional variance than infinite continuous correlations.

Consider two echoes,

$$r1(t) = f1(t-\tau_o) + n1(t), \qquad (10)$$
$$r2(t) = f2(t) + n2(t),$$

where f1(t) is the backscattered signal from a moving fluid at one instant in time and f2(t) is the signal from the same region of the fluid at a latter time T. The time shift to be estimated is τ_o. n1(t) and n2(t) are samples of uncorrelated, zero mean, Gaussian random processes due to the radio frequency interference and electrical noise present in the measurement system. The correlation function which is maximum near $\tau=\tau_o$ is given by

$$G(\tau) = \int_{-\infty}^{\infty} r2(t-\tau)\, r1(t)\, dt \qquad (11)$$

$$\cong \int_{-\infty}^{\infty} [f2(t-\tau)f1(t-\tau_o) + n2(t-\tau)f1(t-\tau_o) + n1(t)f2(t-\tau)]dt \qquad (12)$$

The n1(t)n2(t) term was neglected due to the fact that it is quadratic in noise and will therefore be much smaller than the signal components. G(τ) can be written as follows:

$$G(\tau) = h(\tau) + m(\tau) \qquad (13)$$

where

$$h(\tau) = \int_{-\infty}^{\infty} f2(t - \tau) f1(t - \tau_o)\ dt \qquad (14)$$

$$m(\tau) = \int_{-\infty}^{\infty} n2(t - \tau) f1(t - \tau_o) + n1(t) f2(t - \tau)\ dt \qquad (15)$$

Note that $h(\tau)$ is the deterministic portion of $G(\tau)$ and $m(\tau)$ is subject to random variation due to the noise components in the received echoes. Since $n1(t)$ and $n2(t)$ are zero mean Gaussian random variables, the maximum of $G(\tau)$ will occur near $\tau=\tau_o$ with an expected value $G_o(\tau_o)$ defined by

$$G_o(\tau_o) = h(\tau_o) = \int_{-\infty}^{\infty} f2(t) f1(t)\ dt \qquad (16)$$

The amount that the noise terms $n1(t)$ and $n2(t)$ change the location of the maximum correlation can be modeled as a Gaussian random variable and characterized by its variance and mean. By setting the derivative of $G(\tau)$ equal to zero, the maximum correlation solution can be determined, that is,

$$G'(\tau) = h'(\tau) + m'(\tau) = 0 \qquad (17)$$

Because $n1(t)$ and $n2(t)$ are zero mean random variables, the solution for τ in (17) will be near τ_o [37]. To determine the error in the estimate of the time shift, the equation is expanded in powers of $(\tau - \tau_o)$. Keeping first order terms and using the fact that $G'(\tau_o)=0$ [37], gives the result,

$$(\tau - \tau_o)\ G''(\tau_o) + m'(\tau_o) = 0 \qquad (18)$$

so that

$$\tau - \tau_o = \frac{- \frac{d}{d\tau} [\ f1(t+ \tau - \tau_o)n2(t) + f2(t-\tau)n1(t)\ dt] \Big|_{\tau = \tau_o}}{G''(\tau_o)} \qquad (19)$$

Since n1(t) and n2(t) are zero mean random variables, the estimate of τ_o is unbiased. The denominator is a constant for a particular measurement system. Since n1(t) and n2(t) are independent, the numerator is a random variable composed of two independent parts. The variance is given by

$$\mathrm{Var}[\tau - \tau_o] = \frac{\mathrm{Var}[\int_{-\infty}^{\infty} h1(t)n2(t)\ dt] + \mathrm{Var}[\int_{-\infty}^{\infty} h2(t)n1(t)\ dt]}{[G''(\tau_o)]^2} \qquad (20)$$

where

$$h1(t) = \frac{d}{d\tau} f1(t + \tau - \tau_o) \qquad (21)$$

$$h2(t) = \frac{d}{d\tau} f2(t - \tau) \qquad (22)$$

Using well known results for the response of a linear system to a Gaussian noise source [37], the variance can be expressed in terms of frequency domain quantities as

$$\mathrm{Var}[\tau - \tau_o] = \frac{\frac{1}{2\pi} \int_{-\infty}^{\infty} [\ |H1(\omega)|^2 + |H2(\omega)|^2]\ \eta(\omega)\ d\omega}{[G''(\tau_o)]^2} \qquad (23)$$

where

$$H1(\omega) = j\omega e^{j\,(\tau - \tau_o)}\ F1(\omega) \tag{24}$$

$$H2(\omega) = -\ j\omega\ e^{-j\omega\tau}\ F2(\omega) \tag{25}$$

$\eta(\omega)$ = power spectrum of n1(t) and n2(t)

Equation (23) can be simplified as follows:

$$\mathrm{Var}[\ \tau - \tau_o] = \frac{\frac{1}{2\pi}\int_{-\infty}^{\infty} \omega^2\ [F1^2(\omega) + F2^2(\omega)]\ \eta(\omega)\ d\omega}{[-\ \frac{1}{2\pi}\int_{-\infty}^{\infty} \omega^2 F2^*(\ )\ F1(\ )\ d\ \ ]^2} \tag{26}$$

For white noise $\eta(\omega) = N_o$ so that

$$\mathrm{Var}[\ \tau - \tau_o] = \frac{\frac{N_o}{2\pi}\int_{-\infty}^{\infty} \omega^2 [F1^2(\omega) + F2^2(\omega)]\ d\omega}{[-\ \frac{1}{2\pi}\ \omega^2 F2^*(\omega)\ F1(\omega)\ d\omega\ ]^2} \tag{27}$$

$$\mathrm{Var}[\ \tau - \tau_o] = \frac{\frac{N_o}{2\pi}\int_{-\infty}^{\infty} [F1^2(\omega) + F2^2(\omega)]\ d\omega}{(\ \overline{\omega^2} - \bar{\omega}^2)\ \ \rho^2\ E1\ E2} \tag{28}$$

where

$$\rho = \frac{\int_{-\infty}^{\infty} f2(t)\ f1(t)\ dt}{E1\ E2} \tag{29}$$

and the energy of each echo is defined as follows:

$$E1 = \int_{-\infty}^{\infty} f1^2(t)\ dt \qquad E2 = \int_{-\infty}^{\infty} f2^2(t)\ dt \tag{30}$$

The RMS bandwidth of the received echoes, b, is defined as

$$\beta^2 = \overline{\omega^2} - \overline{\omega}^2 = \frac{\int_{-\infty}^{\infty} [\,\omega^2 F^2(\omega) - F^2(\omega)\,]\, d\omega}{\int_{-\infty}^{\infty} F^2(\omega)\, d\omega} \tag{31}$$

and o is the correlation coefficient as defined in (29). By applying Parseval's relation on the numerator of (28), the variance of the shift estimate can be simplified to

$$\mathrm{Var}[\,\tau - \tau_o\,] = \frac{N_o\ (E1 + E2)}{\beta^2 \rho^2 \quad E1\ E2} \tag{32}$$

Since each echo travels through the same medium and the echoes are highly correlated, the two energies are approximately equal, so that $E \cong E1 \cong E2$. The precision of the time shift estimate (τ) is therefore

$$\mathrm{Precision}\ [\,\tau\,] = \frac{1}{\beta \rho\, \tau_o \sqrt{\dfrac{E}{2\ N_o}}} \tag{33}$$

Figure 7 shows the precision of the time shift estimate versus the mean time shift (τ_o) for the case where $\rho = 1$. This is the case when the two signals, f1(t) and f2(t), are identical waveforms (with possibly different energies). The signal-to-noise ratio is $\sqrt{E/N_o}$ in equation (33). As indicated by equation (33), the precision of the time shift estimate is inversely related to the product of the signal-to-noise ratio and the RMS bandwidth. The precision improves with increasing bandwidth or increasing signal-to-noise ratio. Signal-to-noise ratios of 10 dB, 20 dB and 30 dB for an RMS bandwidth (β) of

2.5 MHz are illustrated in Figure 7. The precision value for each time shift improves by an order of magnitude when the signal-to-noise ratio is increased from 10 dB to 30 dB. A similar improvement would also be observed if the RMS bandwidth were increased by an order of magnitude. Figure 7 suggests that the precision of the time shift estimate can be improved by simply increasing the pulse repetition period (T) resulting in a larger mean time shift for the same axial flow velocity. Although the precision continues to improve with τ_0 when the correlation coefficient is unity, the motion of the scatterers through the ultrasonic beam changes the correlation coefficient and the resulting precision relationship.

As more new scatterers enter the beam during the time between echoes, the maximum correlation of the consecutive echoes decreases. For a given scatterer speed, the maximum correlation will decrease as the time between echoes increases and the precision of the velocity estimate will decrease. On the other hand, if the time between echoes decreases to a very small value, the point of maximum correlation and the corresponding velocity estimate will vary randomly due to the random noise in the backscattered signal.

Foster [12] measured the correlation coefficient for a 5 MHz transducer (25.4 mm aperture) and also derived an approximate expression for the correlation coefficient for a cylindrical beam. In both cases a nearly linear decrease in the correlation function with scatterer motion is observed. From measurements and the cylindrical theory, when the scatterers have moved into half of the beam the correlation coefficient was reduced from 1.0 to 0.3. Thus, according to the results in [12], a good approximation for the correlation between echoes is

$$\rho(a) = 1 - 1.4\ a$$

where

$$a = \frac{V\ T\ \sin(\theta)}{BW} \qquad 0 < a < 5/7 \qquad (34)$$

and BW is the 3 dB beamwidth of the transducer at the measurement range and VT Sin(θ) is the distance the scatterers move perpendicular to the ultrasonic beam axis. The measurement angle (θ), defined in equation (9), changes the correlation between echoes greatly. At $\theta = 0^{\circ}$ the same scatterers are always in the beam and the correlation coefficient is always unity (if beam effects are ignored). In this somewhat impractical case (the beam is inside the vessel), the precision of the time shift estimate is as illustrated in Figure 7. Figure 8 shows the precision versus time shift between echoes using the above model for the correlation between echoes. When equations (9), (33) and (34) are combined, the precision of the time domain correlation method is as follows:

$$\text{Precision}[\tau] = \frac{\sqrt{2}}{\beta\ \tau_o \sqrt{\frac{E}{N_o}}\ \left(1 - \frac{1.4\ \tau_o\ c\ \tan(\theta)}{2\ BW}\right)} \qquad (35)$$

Figure 8 shows equation (35) as a function of τ_o for measurement angles of 45, 60 and 75° for a 20 dB signal-to-noise ratio. A beamwidth (BW) of two wavelengths (0.6 mm at 5 MHz) and an RMS bandwidth of 2.5 MHz were used to generate Figure 8.

These values are typical for the experimental measurements with the 5 MHz transducer to be used in many of the flow measurements discussed in Chapter 7. Figure 8 shows that for each measurement angle the precision value decreases to a minimum (about 5% at 45°) and then begins to increase due to the decorrelation of the echoes. The minimum precision value increases with increasing measurement angle, and the time shift with the minimum precision value decreases. This measurement precision could be expected at midstream where velocity gradients within a range cell are small (a variation of less than 1%) compared to the measurement precision indicated with no velocity gradient. Near the vessel walls, the wide range of flow velocities within a range cell make the precision of the velocity estimate much larger than that indicated in Figure 8.

In summary, the theoretical precision of the time domain correlation method depends on the measurement angle, the system RMS bandwidth, the transducer beamwidth, the mean time shift between echoes, and the signal-to-noise ratio. In Chapter 7, the experimental precision of midstream flow measurements at different measurement angles will be compared to the theoretical precision curves shown in Figure 8.

CHAPTER 4

EQUIPMENT

4.1 BLOOD VESSEL PHANTOM

Figure 9 shows a schematic diagram of the blood vessel phantom system. It consists of a temperature controlled water bath (Excal model EX-500), peristaltic pump (Masterflex model 7520) and fluid flow regulator system. Dialysis tubing with an inside diameter of approximately 6.3 mm was used to mimic the blood vessel in order to minimize the effects of the tube on the ultrasonic beam.

4.1.1 Fluid Flow Regulator

The flow regulator shown in Figure 9 works by maintaining a constant difference (or height, H) in the fluid level in the upper and lower glass reservoirs. Any overflow above the top of inner cylinders of the upper and lower reservoirs is returned back to the pump reservoir. The height of the upper resevoir is adjusted to set the head lost by the fluid (H). After a period of time the flow velocity reaches a steady state value where the viscous losses in the fluid equal the potential energy gained by the fluid. This equilibrium flow can be determined from Poiseuille's law [39] for laminar flow.

Laminar flow occurs when each streamline flows independently with no eddies or turbulence [39]. Laminar flow can be steady or pulsatile. Pulsatile laminar flow is characterized by periodically varying flow velocities at each streamline [39]. Steady laminar flow in a fixed size pipe has a constant velocity at each point in the tube. This property of steady flow makes it easier to measure and quantify. It will therefore be used for all ultrasonic volume flow measurements. The constant laminar flow rate [39] is given by

$$Q = \frac{D^4 \, g \, \rho_o \, H}{128 \, \mu \, L} \tag{36}$$

where

Q = laminar flow rate (m^3/s).
D = tube diameter (m).
g = acceleration of gravity ($9.8\ m/s^2$).
ρ_o = fluid density (kg/m^3).
H = head loss (m).
μ = viscosity of fluid ($N\text{-}s/m^2$).
L = total tube length (m).

For water (viscosity = $0.001\ N\text{-}s/m^2$), a tube diameter of 6 mm and the 1.9 m total tube length (L), a 2 cm head gives a 197 ml/min flow rate. For smaller flow rates (less than 100 ml/min) an extra 2 m long 3 mm diameter plastic tube is added just after the upper resevoir in series with the tube. The larger head required for this long 3 mm tube provides better control and regulation of the flow rate. Since the flow rate is partially determined by the temperature dependent viscosity of the fluid, the temperature is maintained at 25°C throughout the experiment by the water bath heater.

The volume flow rate is measured by closing the return valve on the lower graduated reservoir and measuring the time to fill a given volume. The volume of the outside portion of the graduated cylinder is 253 ml. The time to fill this volume can be measured with an accuracy of approximately ± 0.5 seconds. Thus, a 100 ml/min flow rate can be measured with an accuracy of ± 0.7%. This volume flow measurement is called the hydrodynamic flow rate and is the reference flow rate used to estimate the accuracy of ultrasonically determined volume flow rates.

4.1.2 Fluid Flow Relationships

As flow comes out of the upper reservoir the flow velocities are constant across the tube. This type of flow is called plug flow [39]. As the distance along the tube away from the reservoir is increased, the flow velocity profile changes and becomes more parabolic in shape with the maximum flow at the center of the tube and zero flow velocity at the wall of the tube. Beyond a certain length of straight tube, called the entrance length, the flow is fully developed laminar flow. The fluid velocity profile for fully developed steady laminar flow is parabolic and axially symmetric. The required entrance length (E in Figure 9) is given in [39] as

$$E = 0.073 \frac{\rho_0 Q}{\mu} \tag{37}$$

The entrance length for the fluid regulator system is 29 cm (much less than the total length, L) so the maximum fully developed laminar flow rate (determined by solving (28) for Q) is limited to 238 ml/min. Below this rate the actual entrance length is greater than that required, and fully developed laminar flow is established. Above 238 ml/min some degree of plug flow will be present at the ultrasonic measurement point.

The Reynolds number must also be considered. For laminar flow to exist, the Reynolds number must be less than 2000 [39]. Reynolds numbers above 2000 indicate an increased probability of turbulent flow. In very smooth pipes with no external vibration, laminar flow can be established with a Reynolds number as high as 10,000 [39]. The Reynolds number is defined as follows:

$$R = \frac{4\, Q \rho_o}{D \mu} \tag{38}$$

For water and the maximum fully developed laminar flow rate of 238 ml/min and a tube diameter of 6 mm, the Reynolds number is 841. This indicates that turbulent flow is very unlikely. At a flow rate of 566 ml/min the Reynolds number is 2000 indicating that turbulent flow may exist in the tube.

4.2 TRANSDUCER POSITIONING SYSTEM

This section describes the mechanical system used to position the transducer such that the ultrasonic beam can be scanned across the dialysis tubing at a fixed measurement angle (the angle between the flow direction and the ultrasonic beam).

The measurement angle can be set for a particular experiment by moving the transducer along a circular track which holds the transducer. The transducer and curved track structure are rotated about the scan axis which is approximately 40 mm away from the center of the dialysis tube and is parallel to the tube. The scan angle is the relative angle about which the track assembly is rotated about the scan axis and determines the position where the ultrasonic beam intersects the dialysis tube. During a volume flow measurement experiment, the scan angle is changed so that the ultrasonic beam samples the two dimensional flow velocity profile inside the dialysis tube.

Figure 10 is a schematic diagram of the angle measurement system employed to determine the scan angle. A Helium-Neon 1 mW laser is directed at a front surface mirror which is mounted so that the scan axis is contained in the plane of the mirror. The transducer is mounted to the scan axis shaft via a curved measurement angle track. The scan axis shaft is held by a long Teflon^R bearing and the mirror is mounted on the top of this shaft. When the transducer is rotated by the scan angle α, as shown in Figure 10, the projection of the laser beam on the meter stick moves an angle 2α. The scan angle, α, is given by

$$\alpha = \frac{1}{2} \arctan\left(\frac{X - 50}{D_M} \right) \tag{39}$$

where

X = meter stick reading (cm).
D_M = minimum distance from meter stick to scan axis (cm).

The transducer is rotated about the scan axis by hand, using a spring-loaded micrometer adjustment. Since the meter stick is used to measure the position of the laser beam, the scan angle measurement accuracy is approximately ± 0.2% (2 mm out of 1 m). This accuracy can be obtained if the entire length of the meter stick is traversed by the laser beam. The precision of a full scale (X=100) scan angle measurement is less than or equal to 0.2%, since the operator should be able to repeatedly read the meter stick within 1 mm standard deviation. For the 6 mm diameter dialysis tube, the ultrasonic beam intersects the tube for a scan angle range of approximately $\pm 4^{o}$. Thus, the accuracy of the scan angle measurement is approximately $\pm 0.016^{o}$ (0.2% of 8^{o}).

The measurement angle (θ) can be changed by sliding the transducer along a specially machined circular track which holds the transducer. Figure 11 shows a cross section of the transducer, dialysis tube and track structure. The radius of the track and the distance from the vessel to the scan axis were designed such that the focus of the transducer remains close to the vessel center. This has been verified by placing a point reflector at the tube center and adjusting the transducer mount for a minimal change in the time of arrival of the reflector's echo as the measurement angle was changed. Typically less than 2% variation in the round trip time of the echo from the point target was obtained for a measurement angle change from 45^{o} to 75^{o}.

4.3 TRANSDUCER ELECTRICAL CHARACTERISTICS

Accurate pulse-echo ultrasound experiments require the transducer to be shock excited with a very short high voltage pulse. This will provide a wideband large ultrasonic pulse and therefore the best axial resolution and energy level. Proper design of the transducer pulser and receiver circuits, described in the next section, requires a detailed knowledge of the electrical characteristics of the ultrasonic transducers to be used.

A simple and practical model of a typical highly damped transducer is shown in Figure 12a. The series RLC circuit represents the acoustic resonance of the piezoelectric material. The electrical resonant frequency of these elements is the same as the acoustic resonant frequency. The resonant frequency for damped, low Q, transducers [40] is primarily determined by the thickness of the pizeoelectric material. The quality factor (Q) of the transducer is determined by the properties of the transducer materials. The parallel capacitor (C_o) is determined by the size of the transducer, the dielectric constant of the piezoelectric material and the length of the cable connected to the transducer.

The values of the equivalent electrical elements (R, L, C, C_o) have been determined for each of the three transducers used in this study. The complex impedance of the transducers at many frequencies between 400 kHz and 20 MHz was measured using a vector impedance meter (HP model 4193A). The impedance functions (magnitude and phase) were then used to calculate the element values for each transducer. At low frequencies (400 kHz) the series RLC circuit has a negligible effect on the overall transducer impedance so that the magnitude of the impedance at 400 kHz was used to determine the value of C_o. At the resonant frequency of the transducer the RLC circuit is resistive and provides the maximum phase transducer impedance. The quality factor of the RLC circuit was determined by subtracting the admittance of C_o from the transducer admittance. The resulting admittance function represents the admittance of the series RLC circuit alone. The peak of this admittance curve is the admittance of R. The two frequencies at which the admittance falls -3dB (0.707) below the peak admittance was used to determine the bandwidth of the transducer. The quality factor and the RLC elements were then determined.

The values of the transducer model elements for each of the three focused transducers (Panametrics models V307, V309, and V3323) are shown in Figures 12b, 12c and 12d, respectively. The transducers will be referred to by number, as indicated in Figure 12. Note that the 10 MHz transducer (transducer number 3) has an inductor inside the body of the transducer in order to improve the electrical matching when long cables are used. All three transducers have a two inch focal length. Table 3 summarizes the characteristics of each transducer.

Table 3 - Characteristics of Three Panametrics Transducers.

Transducer Number	Aperture Size (mm)	Center Frequency (MHz)	Quality Factor	Capacitance at 400 kHz (pF)
1	25.4	5.0	2.0	1250
2	12.7	5.0	2.8	1120
3	25.4	10.0	2.8	330

4.4 TRANSDUCER PULSER-RECEIVER

The circuit used to shock excite and receive the ultrasound echoes from the transducers described above is shown schematically in Figure 13. A vertical field effect transistor (VFET, RFP15N15) is used to develop a large current, I_o, in an inductor, L1. A driver integrated circuit (DS0026) is used to turn the VFET off when the trigger signal from the ultrasound data acquisition system (UDAS, see section 4.5) goes high. When the magnetic field established in L1 collapses, the voltage on the drain of the VFET is given by the following equation:

$$V = I_o \sqrt{\frac{L1}{C_t}} \ \mathrm{Sin} \frac{t}{\sqrt{L1 \ C_t}} \quad , \ 0 \leq t \leq \pi \sqrt{L1 \ C_t} \qquad (40)$$

where C_t is the total capacitance of the VFET, transducer and diode circuits. After the half cycle of the sinewave is completed, D1 conducts and the VFET is turned back on when the trigger pulse returns to zero. During the transmit phase just described, D2 is conducting so that the voltage on the transducer is almost the same as the voltage on the drain of the VFET.

After the VFET is on and the transducer voltage is near zero, D2 opens and any voltage appearing on the transducer appears across the wideband toroidal transformer, T1. The impedance of the transducer (20-30 ohms at center frequency) is transformed to 50 ohms by T1 for easy transmisson to the wideband amplifiers located several meters away. This transformation also increases the signal level without increasing the relative noise level. The inductance of the primary winding of T1 also insures that D2 turns off (after about 20μS) causing the pulser-receiver to switch from transmit to receive mode.

The received signal from transformer T1 is fed into an amplifier (Aydin Vector MHD-175) with a gain of 50 dB and a bandwidth of 40 MHz. The amplified echoes are then directed to the UDAS for further signal processing.

Figure 14 shows the result of a SPICE simulation [41] of the pulser output and acoustic pressure output for each of the three transducers. The measured values of the transducers shown in Figure 12 were used in each case. Each of the simulated results have two waveforms superimposed on each plot. The shorter waveform in each plot is the simulated pulser output in volts at the transducer terminals. In each case the peak voltage is limited to 150 V, which is the breakdown voltage of the VFET. A different initial inductor current (I_o) for each transducer is indicated for each case. This current is adjusted by changing the VFET power supply voltage. The longer duration waveform is the voltage across the radiation resistor (R in Figure 12a) which is proportional to the acoustic pressure emitted by the transducer. It can be seen from Figure 14 that the acoustic pressure waveform is primarily determined by the transducer acoustic quality factor. Because the pressure waveform is longer than the excitation, the bandwidth of the excitation is larger than the pressure waveform and does not significantly affect the bandwidth of the transmitted waveform.

4.5 ULTRASOUND DATA ACQUISITION SYSTEM

The Ultrasound Data Acquisition System (UDAS) provides the basic requirements to collect and analyse ultrasound echoes in the frequency range between 0.5 MHz and 15 MHz [42]. An overall block diagram of the UDAS is shown in Figure 15. A 1 V peak-to-peak signal can be sampled every 20 ns with the 8 bit A/D converter. The unit provides a periodic short pulse to trigger an ultrasound pulse generator at a rate up to 30 kHz. At a programmable time after the trigger, a number of samples are stored in the high speed memory. This programmable range gate can be repeated a given number of times as requested. Up to 393,216 (384 Kbytes) total samples can be stored in the data memory.

A Z-80 microcomputer controls the operation of the UDAS. This computer has a serial interface for communication with a larger host computer, a DMA controller for data memory transfers, an external data bus interface for communication with other devices and an ASCII keyboard interface for data entry. All of these circuits are contained on the UDAS CPU board and control the remaining circuit boards.

The A/D converter interface board contains a TRW TDC1026E1C 50 MHz 8 bit A/D converter, high speed data registers, and clock generation circuits. The 8 bit ECL output of the A/D converter is stored in eight, 4 bit shift registers every 20 ns. At the end of four clock cycles, the four data bytes are transferred to a 32 bit register. The output of this register appears on the 32 bit high speed DMA bus for storage in the memory. This technique reduces the bandwidth requirement of the DMA bus by a factor of 4.

Data appear on the 32 bit DMA bus every 80 ns. In order to store these data, memory with a cycle time of 80 ns or less would be required. This type of memory is very expensive and has a low density (bits/package). For these reasons, slower NMOS static memory was chosen for this application. To allow these slower memories to be used, data on the 32 bit DMA bus are latched into 4 different memory boards in a sequential fashion.

Since a large memory size is required for many ultrasound experiments, each memory board was designed to contain 32 Kbytes of data memory. The cycle time of each individual memory board is 320 ns. Since each dual port memory board is addressed as one of four consecutive bytes, a minimum of four memory boards are required in order to have continuous memory. In the current system, 12 memory boards were fabricated for a total of 384 Kbytes. Unlike the other components of the system, the memory boards are printed circuit boards to reduce the cost of construction.

The dual port memory boards can be accessed in one of two ways. As described above, data from the A/D converter DMA board are transferred into the memory via the 32 bit DMA bus. The Z-80 microcomputer can also read and write any location in the data memory via the 8 bit bidirectional (tri-state) data bus. This allows for analysis as well as storage of the data. The high speed correlator board also uses this 8 bit bus to fetch the values to be correlated from data memory.

The display board contains two types of video display devices. The alphanumeric portion provides 80 columns by 24 lines of characters with cursor addressing and other standard terminal functions. The graphic portion of the display board provides a computer addressable 256 x 192 pixel black and white display mode or a lower resolution color display mode. These two commericially available boards are mounted together on the UDAS display board.

In order to analyze the ultrasound echoes, a high speed correlator board was designed. This board acts as a DMA device and accesses the data memory directly at a 2 Mbyte/sec rate. Every microsecond, two samples can be multiplied and added to the previous result. Thus, one million multiply-accumulate operations are performed each second. The DMA address generator on the multiplier-accumulator board provides two addresses and can sequence through up to 256 locations. Thus the high speed correlator board performs the function

$$C = \sum_{i=0}^{N-1} X(a + i) \quad Y(b + i) \tag{41}$$

where

X(a) = first data value fetched (8 bits: -128 to 127)
Y(b) = second data value fetched (8 bits: -128 to 127)
a = start address of first data
b = start address of second data
i = address sequence value
N = number of values to accumulate (1 to 256)
C = final result

This function is a discrete correlation and can be used to perform a variety of signal processing tasks [43]. Absolute time of flight can be estimated by searching for the maximum correlation of the echo data with a stored waveform. A short length DFT can be implemented by precalculating the DFT coefficients and storing them in memory. Digital filtering or convolution can also be accomplished in a straightforward manner. All of the preceding tasks would require excessive computation on a host computer, especially if the data set size were large. Furthermore, the time required to send the data to another computer over serial communication lines may be orders of magnitude greater than the computation time using the multiplier accumulator. Other tasks, such as floating point operations, can be accomplished much easier on a host machine.

4.6 CALIBRATION OF MEASUREMENT SYSTEM

Any ultrasonic measurement of distance is dependent on two factors: the speed of sound of the medium and the measurement of the time delay. One uncertainty in the measurement of delay is the delay introduced by the transducer, pulser-receiver and UDAS. Since this delay is difficult to estimate, it has been measured experimentally as described in the next section. Section 4.6.2 describes a time of flight method used to measure the speed of sound of the materials used in this study.

4.6.1 Range Estimate Accuracy

The time delay from the UDAS trigger pulse to the time an echo signal is sampled by the A/D converter is determined by counting the number of 50 MHz clock periods with a simple counter circuit. The counter value at the time the range gate starts indicates the number of 20 ns periods which have occurred since the trigger. The time of arrival of the ultrasonic echo reflected from a target is dependent on the speed of sound in the medium, the speed of sound of the transducer material, the delay introduced by the pulser-receiver electronics and the length of the cables between the UDAS and the pulser-receiver. Since some of these delay elements do not change from one experiment to the next, they can be lumped together into a single constant, t_o. The time of arrival of a hypothetical target at the front face of the transducer is t_o. Thus, the datum or reference of the range measurement is the front face of the transducer.

Figure 16 shows the results of a known position versus time of arrival experiment. A mill base (which is calibrated in inches) was used to accurately position a 1.4 mm diameter stainless steel pointed target. The point target was first positioned at the front face of the transducer in the center of the transducer aperture. The target was then moved away from the transducer a distance of 1.600 inches (40.64 mm). The echo was sampled by the UDAS and sent to the host computer for later processing. The target was moved 0.01 inches (0.254 mm) away from the transducer and this echo was sampled and sent to the host computer. This process was repeated until the signal was reduced to less than a tenth of the peak amplitude near the focus at approximately 1.92 inches (48.768 mm). The signal level at the UDAS input was adjusted so that the peak echo amplitude was within 10 A/D converter levels of the maximum clipping level (127 or -128). The time of the first transition away from the average signal level of the echo was used to estimate the time of arrival of the echo. In order to be considered as the arrival time, the transition away from the average must be greater than three quantization levels and must be followed by a large peak (greater than 50 quantization levels away from the average). Since the signal-to-noise ratio is very large (greater than 40 dB) this simple technique can be used to determine the time of the first ultrasonic response due to the target. Figure 16 is a plot of the resulting time of arrival of the echo versus distance from the transducer face and will be used to estimate the absolute distance at each range cell. This result, shown for transducer number 1 at 25^{o}C, gives an approximate speed of sound (1.496 mm/μs) and the time from the trigger pulse for a hypothetical target at the transducer face (t_o= 3.331 μs). Both of these estimates are determined from a linear least squares fit of the mill base experimental data. The t_o estimate is the time axis intercept of the best fit line from the 51 data points, and the speed of sound is the inverse of the slope estimate. The standard deviation of the time of arrival estimate obtained from the regression is 0.0233 μs. The mill base positioning system is accurate to ± 0.04 mm (± 0.001 inches). Thus, the 95% confidence interval of the least squares zero time of arrival estimate is ±0.0823 μs [45]. The estimate of the range distance from the face of the transducer to the center of a particular range cell is given by

$$R = c_o \ (t/2 + t_g/4 - t_o) \tag{42}$$

where

R = range from face of transducer to the range cell (mm).
t = start time of range gate (μs).
t_g = range gate length (μs).
t_o = time of arrival at front face (μs).
c_o = speed of sound in medium (mm/μs).

4.6.2 Speed Of Sound Measurement

The speed of sound was measured for each of the fluids used in this study. The time of flight of a 5 MHz ultrasonic pulse (about five cycles) was measured for distilled water, normal saline, a 50% glycerin-water mixture, and porcine blood. Distilled water and normal saline were used as a surrounding fluid (speed of sound c_0). In all cases, the temperature of the 40 liters of surrounding fluid was held at a constant temperature of 25°C (± 0.5°C) by the temperature controlled water bath (EX-500). Distilled water, a 50% glycerin-water mixture and porcine blood were used as scattering fluids (speed of sound c_1) inside the tube. The 50% glycerin-water mixture was made by mixing 500 ml of glycerin with 500 ml of distilled water.

Water with Sephadex^R particles and the 50% glycerin-water mixture with Sephadex^R (Sephadex^R G-50, particle size 20-70 μm) were measured. Sephadex^R was added to distilled water and the glycerin-water mixture in order to scatter ultrasound in a similar way that red blood cells scatter ultrasound. Approximately 2 grams of Sephadex^R per liter of fluid (either water or glycerin) were added in each case. This amount of Sephadex^R resulted in strong ultrasonic backscattering (greater than 20 dB signal to noise ratios) and, additionally, remained suspended in the fluid. Approximately one liter of porcine blood was collected into 200 ml of anti-coagulant solution, and this mixture was measured within one hour. The anti-coagulant solution was 2.2% sodium citrate and 2.5% dextrose.

Each speed of sound measurement proceeded as follows. A small Plexiglas^R tube (0.75 inch inner diameter by 1.00 inches long) with a transducer mounted on one end of the tube was used to hold the fluid to be measured. The transducer was an unfocused transducer with a 0.75 inch (1.91 cm) diameter aperture and a resonant frequency of 5 MHz (Panametrics model number A308). The fluid to be measured was poured into the open end of the inverted Plexiglas^R tube on top of the front face of the transducer. The transducer and Plexiglas^R tube assembly was mounted so that gravity makes the top surface of the fluid perpendicular to the tube wall and the ultrasonic beam. The UDAS and pulser receiver were used to record the first two echoes caused by reflection of the ultrasound by the top surface of the fluid being measured. The first echo occurs at the time required for the ultrasound to travel from the transducer to the fluid surface and back. The second echo occurs at the time the first echo reflects off the front of the transducer, travels to the fluid surface, and back to the transducer. As indicated in [44] the time between the first and second echoes is a good indication of the round trip time required for the ultrasonic pulse to travel twice the length of the fluid being measured. A total of 2048 samples were stored by the UDAS (representing 40.96 μs) and then sent to the host computer where the time between the first two echoes was estimated. This round trip time was estimated by locating the time shift between the echoes which gave a maximum correlation. This time shift was estimated to the nearest sample period (0.02 μs) providing a very accurate (± 0.07% of 35 μs) estimate of the time between echoes.

The uncertainty in this speed of sound measurement can be traced to the ability of the experimenter to maintain the fluid level of each liquid equal to the total length of the Plexiglas^R tube. The length of the Plexiglas^R was measured to be 1.035 inches (26.29 mm) with an accuracy of ± 0.01%. The round trip length is therefore 52.58 mm. The measurement of the time of flight by the correlation method is accurate to better than ± 0.02 μs (one sample period). Thus, the uncertainties of the distance measurements and the time of flight measurements are small compared to the uncertainty in setting the column height to the length of the tube.

By doing a series of time-of-flight experiments with water, the fluid level uncertainty appears to be about ± 0.9%. Thus, the speed of sound results shown in Table 4 reflect this uncertainty:

Table 4 - Speed of Sound of Materials Used in This Study.

Material	Temperature (^{o}C)	Round Trip Time (μs)	Speed of Sound (mm/μs)
Water	24.8	35.1	1.50 ± .01
Normal Saline	25.0	34.7	1.51 ± .01
Porcine Blood	24.9	33.9	1.55 ± .01
50% Glycerin	24.4	30.9	1.70 ± .02

The values for water, saline, and 50% glycerin agree with published values [44]. The speed of sound measurement obtained from the slope of the mill base experimental data (1.496 mm/μs, see the previous section) also agrees with the measured value for distilled water. The values in the literature for various kinds of blood at 25^{o}C vary from 1.52 to 1.58 mm/μs depending on the species and type of anti-coagulant used [27,28,46,47].

In order to determine the change in the speed of sound due to adding Sephadex^{R} particles to the distilled water and the glycerin-water mixture, two experiments were performed. Both experiments measured the change in the speed of sound caused by the addition of the Sephadex^{R} to one of the fluids. Since the column height remains virtually unchanged by adding the Sephadex^{R}, the change in the time of flight can be used as a good indicator of a change in the speed of sound. With the fluid in the measurement tube (volume 8 ml), 0.16 grams of Sephadex^{R} was added (2 grams/l). The round trip time before and after the Sephadex^R was added was then compared. The round trip time of the distilled water changed less than 0.5% when the Sephadex^R was added. Sephadex^R was added to the glycerin-water mixture resulting in less than 0.5% change in the round trip time. Thus, the speed of sound of each fluid is assumed to be the same with Sephadex^R as without Sephadex^R.

CHAPTER 5

AXIAL FLOW VELOCITY MEASUREMENT METHOD

This chapter introduces the methods used to measure the axial flow velocity by the time domain correlation technique. The axial flow velocity is the component of the flow velocity in the direction of the ultrasound beam axis. All ultrasound measurements of motion determine the velocity of the scatterers in the direction of propagation of the ultrasonic energy [10,12]. Thus, the flow velocity must be calculated from the axial flow velocity measurement and the angle between the axis and the direction of flow (measurement angle, Θ, as defined in section 3.1). In Chapter 6, methods to estimate the measurement angle from a collection of axial velocity measurements will be discussed; in the current chapter methods to measure the axial flow velocity versus range are described.

The axial flow velocity can be determined at different positions within the vessel, at different times, or both. In this thesis, axial flow velocity measurements versus time are defined as pulsatile flow measurements independent of the type of flow being measured (steady or pulsatile). The pulsatile flow measurement method used in this research will be described in section 5.3. One dimensional flow measurement is defined as the measurement of the axial flow velocity versus range along the ultrasonic beam axis. The previous research [12] was limited to one dimensional flow velocity measurements. Two dimensional flow measurements are determined from the axial flow velocity measurements versus range along the beam as a function of scan angle. The two dimensional flow measurement method, described in the next chapter, will be used to determine the measurement angle (Θ) and the volume flow. This section provides the details of the axial flow velocity measurement method developed by using the ideas presented in Chapter 3 and [12].

The theoretical precision of the time domain correlation method derived in Chapter 3 and illustrated in Figure 8 indicates that significant changes in the precision of the axial flow measurement occur as the mean time shift or measurement angle is changed. The precision value for each measurement angle also depends on the signal-to-noise ratio. The signal-to-noise ratio only scales the precision curve; the shape of the curve remains the same. Because of this scaling property, the relative variance curve (variance divided by the minimum variance throughout all time shifts) of a flow estimate for a particular transducer and particular measurement angle can be determined *a priori*.

Since the relative variance curve does change with measurement angle, the location of the minimum variance cannot be determined unless the measurement angle is known. By using a series of flow measurements of constant flow the variance of the flow estimates can be determined for the particular transducer configuration. The estimate of the variance by this method assumes that the flow remains constant throughout the measurement interval. This is a reasonable assumption when steady flow is measured, but clearly not valid when pulsatile flow is measured. For this reason, pulsatile flow measurements (to be considered in more detail later) require prior knowledge of the measurement angle.

The next section describes the method used to determine a flow estimate of steady flow so that the minimum variance is obtained throughout all range positions. Section 5.2 describes the programs used to determine the time shift of the echoes by discrete time domain correlation.

5.1 MINIMUM VARIANCE FLOW

If only two echoes are used to measure the axial velocities at many range positions, the precision of the measurement at the midstream position can be made small (by proper choice of the time between echoes) but at ranges near the vessel walls, the shift will decrease and the imprecision of the flow estimate will increase dramatically. This increase in the imprecision was illustrated in Table 2 obtained from [12].

In order to provide a flow estimate with the minimum variance throughout all range positions, a series of N consecutive echoes each separated by the pulse repetition period, T, can be used effectively. At a particular range the axial flow velocity estimate for a pair of echoes is given by

$$V_{AE} = \frac{c\ S(i,j)}{2\ (j - i)\ T} \qquad (43)$$

where

V_{AE} = magnitude of the axial flow velocity of the scatterers at a particular range estimated from two echoes.
$S(i,j)$ = time shift between the ith and jth echo ($j>i$).
T = pulse repetition period.
c = speed of sound in the scattering fluid.

By averaging these estimates together in an optimum weighted fashion, a minimum variance axial flow velocity estimate $\hat{V}_A$ can be determined (method to be described below). From this optimum axial flow velocity value, the magnitude of the flow velocity in the tube, $\hat{V}$, is

$$\hat{V} = \hat{V}_A \ / \ \mathrm{Cos}(\theta_M) \qquad (44)$$

where θ_M is the estimate of the angle between the ultrasound beam axis and the velocity vector (measurement angle).

The relationship between $\hat{V}_A$ and V_{AE} is determined by the method used to average the V_{AE} values. One solution for $\hat{V}_A$ is simply to average all the V_{AE} estimates with equal weight applied to each. This is not practical because the precision of each V_{AE} value varies as a function of position and time shift. For example, if the average shift between consecutive echoes ($j-i=1$) were 50 ns, then the average shift between every other echo ($j-i=2$) would be 100 ns. The precision of the shift estimate with a 100 ns mean shift would be considerably smaller in the typical case illustrated in Figure 8.

As shown in [10,12,34] the backscattered ultrasound signal from a scattering fluid is approximately Gaussian and each echo is an independent measurement. Since new scatterers with different random orientations and positions are constantly entering the ultrasonic beam, the echoes should be independent. As was assumed in the theory and by other results [12], the axial flow velocity estimates, V_{AE}, are assumed to be independent Gaussian random variables which can be completely specified by a variance and a mean.

Since each V_{AE} estimate is assumed to be an independent measurement, all pairs of echoes can be used to determine a shift value and corresponding velocity value at each range position. There are N consecutive echoes resulting in N-1 pairs of consecutive echoes (j-i=1) which can be used to determine N-1 V_{AE} estimates of the axial flow velocity. Also, there are N-2 pairs of echoes separated by 2T (using every other echo), N-3 pairs of echoes separated by 3T (using every third echo), and so on. Thus, at each range position, a total of N(N+1)/2 axial velocity values (V_{AE}) can be determined from N echoes. Because the mean time shift for each S(i,j) changes with the number of periods between echoes, some of the axial velocity estimates will have much larger variances than other V_{AE} values. It is, therefore, desirable to weight axial flow velocity estimates with a small variance more heavily than other axial flow velocity values with a larger variance. Let W(i,j) be a set of weighting coefficients. The axial flow velocity estimate is given by

$$\hat{V}_A = \frac{c}{2\ T} \sum_{i=1}^{N-1} \sum_{j=i+1}^{N} \frac{W(i,j)\ S(i,j)}{j - i} \tag{45}$$

$$\text{where} \quad \sum_{i=1}^{N-1} \sum_{j=i+1}^{N} W(i,j) = 1 \tag{46}$$

The variance of this estimate is

$$\mathrm{Var}[\hat{V}_A] = \frac{c^2}{4\quad T^2} \sum_{i=1}^{N-1} \sum_{j=i+1}^{N} \frac{W(i,j)^2}{(j - i)^2} \mathrm{Var}[S(i,j)] \tag{47}$$

or,

$$\hat{V}_A = \sum_{i=1}^{N-1} \sum_{j=i+1}^{N} W(i,j)\ V_{AE}(i,j) \tag{48}$$

$$\mathrm{Var}[\hat{V}_A] = \sum_{i=1}^{N-1} \sum_{j=i+1}^{N} W(i,j)^2\ \mathrm{Var}[V_{AE}(i,j)] \tag{49}$$

Since all the echoes are assumed to be independent samples of Gaussian random processes [10,12], the flow estimates obtained from steady flow are stationary to order 2 since during the N echoes the mean and the variance of the process will not change. This assumption greatly simplifies the optimum axial velocity estimate for steady flow. Therefore, the variance of the shift estimate does not depend on the time the echoes are sampled. Thus,

$$\mathrm{Var}[S(i,j)] = \mathrm{Var}[S(j-i)] = \mathrm{Var}[S(DEL)] \tag{50}$$

where DEL is the number of time periods, j-i, between echoes. With the above assumption, the optimum axial flow estimate is as follows:

$$\hat{V}_A = \frac{c}{2\ T} \sum_{DEL=1}^{DELMAX} W(DEL) \left[\frac{1}{N - DEL} \sum_{i=1}^{N-DEL} \frac{S(i,i+DEL)}{DEL} \right] \tag{51}$$

Because Var[S(DEL)] depends only on the time shift between echoes, the variance of the velocity estimate can be minimized by proper selection of the weighting coefficients (W(i,j)). The variance function can be determined _a priori_ for a particular transducer configuration. With this _a priori_ information and the S(i,j) values, equations (45) and (46) can be used to solve for the optimum set of W(DEL) values. The solution for independent Gaussian variables, given in [48], shows that the weighting coefficient is inversely proportional to the variance of the estimate. This can be expressed as

$$W(DEL) = \frac{K\ \ DEL^2}{\mathrm{Var}[S(DEL)]} \tag{52}$$

The value of the constant, K, can be determined by combining equation (37) and (41), giving

$$W(DEL) = \frac{DEL^2\ (\ \mathrm{Var}[S(DEL)]\ )^{-1}}{\displaystyle\sum_{k=1}^{DELMAX} k^2\ (\ \mathrm{Var}[S(k)]\ )^{-1}} \tag{53}$$

The denominator of equation (53) is simply the sum of the variances of the V_{AE} estimates and assures that the sum of the weighting function is unity.

For a large number of echoes (N > 30) a reasonable estimate of the Var[S(DEL)] can be obtained from the shift estimates by the discrete summation

$$\mathrm{Var}[S(DEL)] = \frac{1}{N-DEL}\sum_{i=1}^{N-DEL} S(i,i+DEL)^2 - \left[\frac{1}{N-DEL}\sum_{i=1}^{N-DEL} S(i,i+DEL)\right]^2 \quad (54)$$

where the second term is the average shift squared for each DEL value. The Var[S(DEL)] and the W(DEL) weighting function can be calculated for $1 \leq DEL \leq DELMAX$ where DELMAX is the maximum j-i value considered. W(1) and W(DELMAX) should both be small compared to the maximum weighting function for best performance. Thus, an optimum axial velocity of a scatterer at each range along the vessel can be obtained. The variance of the weighted velocity estimate is found by substituting (53) into (47). The result is

$$\mathrm{Var}[\hat{V}_A] = \frac{c^2}{4\,T^2 \displaystyle\sum_{DEL=1}^{DELMAX} \frac{DEL^2}{\mathrm{Var}[S(DEL)]}} \quad (55)$$

The $Var[\hat{V}_A]$ is always less than or equal to the smallest $Var[S(DEL)]/DEL^2$ term, as can be seen from equation (55). If the $Var[S(DEL)]/DEL^2$ terms were equal for all DEL, then by equation (55),

$$Var[\hat{V}_A] = c^2 \; Var[S(1)] \; / \; 4 \; T^2 \; DELMAX \tag{56}$$

Equation (56) represents a significant improvement in the variance compared to the variance associated with estimating the axial velocity from only one DEL value ($c^2 Var[S(1)]/4\;T^2$). Since all of the individual variances ($Var[S(DEL)]/DEL^2$) are not equal, the improvement in the variance of the optimum axial velocity estimate compared to the smallest variance of the individual variances at each DEL value is not as large as predicted by (56). The improvement in the variance of the optimum axial velocity estimate can be expressed as the ratio of the minimum variance of the individual estimates for all DEL values to the variance of the optimum estimate given by (55). This ratio is always greater than one and is expressed by

$$\frac{Min(Var[V_{AE}])}{Var[\hat{V}_A]} = Min(\frac{Var[S(DEL)]}{DEL^2}) \sum_{DEL=1}^{DELMAX} \frac{DEL^2}{Var[S(DEL)]} \tag{57}$$

Where the Min( ) operator indicates the minimum of all DEL values ($1 \leq DEL \leq DELMAX$).

5.2 DISCRETE MAXIMUM CORRELATION METHOD

The time shift between echoes is estimated by determining the time shift with the maximum correlation between two echoes, as indicated in Chapter 3. Unfortunately, the correlation function has many local maximum values (see Figure 6) due to the bandlimited nature of the echoes, and the correlation between echoes can only be estimated at discrete multiples of the sampling rate. This section provides the details of programs used to estimate the continuous time shift between echoes and the methods used to avoid the problems associated with the multiple peaks of the correlation function.

With a UDAS sampling rate of 50 MHz, the correlation function of each pair of echoes can be calculated at discrete shifts of 20 ns each. As shown in the theoretical precision versus time shift curves (Figure 8), the velocity estimate with the best precision is obtained with a 100-200 ns time shift. Thus, for best precision, the pulse repetition period should be set so that the shift with maximum correlation is between five and ten samples. Suppose that the correlation between echoes is determined at ten discrete values from zero to nine samples. The shift with the largest correlation is used as the shift estimate, $S(i,j)$, as in equation (43). The shift estimates are then averaged in an optimum fashion as described in the previous section. The variance due to the discrete nature of the shift estimate would significantly increase the variance of the flow estimate.

For illustration purposes, the error introduced by the discrete estimate of the time shift can be modeled as a zero mean uniformly distributed random variable from -0.5 to 0.5 samples as is often done in the analysis of quantization of analog signals [43]. The variance of this error is 0.084 (variance of the uniform error distribution). The precision of a flow estimate would be limited to 5.8% by this additional error if the continuous case had a zero variance.

For example, if the mean time shift to be estimated were five samples, then the precision of a continuous correlation estimate would be less than 5% for signal-to-noise ratios greater than 20 dB, a 45^o measurement angle, and an RMS bandwidth of 2.5 MHz (see Figure 8). The variance due to the discrete correlation and the variance of the continuous time correlation estimate can be added together by making the assumption that the two errors are independent. This is a reasonable assumption used in almost all quantization problems in digital signal processing. The sum of the variances of a continuous time correlation flow estimate with a 5% precision (0.061 variance) and the discrete error (0.084 variance) is 0.145. The precision of this discrete time flow estimate is, therefore, approximately 7.6%. This considerable increase in the standard deviation of the flow estimate indicates the importance of computational methods which estimate the shift with the maximum correlation more precisely by interpolation of the discrete correlation values.

Techniques which estimate the peak correlation of two signals by iterative methods are discussed in [49] and [50]. These techniques require a great deal of computation, since a large portion of the correlation function must be calculated. Frequency domain methods are also indicated in [50]. Since these methods require that a number of FFTs be computed, the computation time is again excessive on a general purpose computer. For these reasons, the peak of the correlation function was estimated by fitting a parabolic curve to the peak correlation point and the two nearest neighbors. This technique was used by Foster [12] and analysed extensively by Boucher and Hassab [51].

The variance and bias due to the parabolic fit of the correlation peak were determined theoretically for a bandpass signal. The results in [51] show that the variance of the time shift estimate from the parabolic-fit peak method was slightly larger than the variance from methods which calculate the peak by band-limited interpolation of the correlation function [49]. The bias of the parabolic-fit peak method was also derived in [51]. The time shift estimate was shown to be unbiased when the peak was at a discrete number of samples or half way between the two sample points. The bias of the shift estimate between these unbiased values changes with the signal-to-noise ratio and signal bandwidth. Independent of the noise level, the bias increases to a maximum value at one quarter and three quarters of the time between samples.

The example given in [51] was for a 0 dB signal-to-noise ratio and a bandwidth of 30% of the sampling rate. This worst case example showed an estimated shift of 0.22 when the actual shift was 0.25. If the shift to be estimated was 5.25 samples, then the discrete correlation method would give a 5.22 sample result. This represents a -0.6% error in the shift estimate. For larger shifts or greater sampling rates this inaccuracy becomes smaller.

Figure 17 shows a flow chart of the maximum correlation algorithm. The algorithm works properly when the pulse repetition rate is large enough so that the maximum correlation for two adjacent echoes (DEL=1) occurs at less than five samples. The first set of correlations is calculated at -2,-1,0,1,2,3,4, and 5 samples of shift between echoes. The algorithm first finds the local maximum of the discrete shifts. If the correlation between the echoes for a particular shift is negative, the next correlation at the next shift value is calculated. Once a positive correlation between the echoes is found, the correlations for the next two shifts are determined. If the second correlation (PREV1 in the flow chart) is not greater than both the first positive correlation (PREV2) and the third correlation (ACC, the most recent value) then additional correlations are performed until a local maximum is located. Once the maximum PREV1 value is located, no more correlations need be calculated to estimate the shift. The fractional portion of the shift is then calculated from the three correlation values by the parabolic-fit method (see equation shown in Figure 17).

If the shift of the echoes is at a point greater than five samples, the multiple peaks in the correlation function could cause an erroneous estimate of the maximum correlation shift. The pulse repetition period must be set so that the peak shift between consecutive echoes is between one and four samples. If the shift is less than one sample, the variance of the flow estimate for DEL=1 will be very large and will not significantly contribute to the improvement of the optimum velocity estimate indicated by equation (54). In other words, the variance of the DEL=1 term would be so large compared to the other variances that little can be gained by calculation of the shifts.

Then, every other echo (DEL=2) is used to estimate the shift by starting at two samples less than twice the shift estimate for adjacent echoes. Thus, the shift of the next DEL value is guessed from the shift of the previous DEL value. As shown in Figure 17, the starting point for the next shift estimate, GUESS, is

$$\mathrm{GUESS} = E[S(\mathrm{DEL})]\ (\mathrm{DEL} + 1)/\mathrm{DEL} \tag{58}$$

where E[S(DEL)] denotes the mean shift calculated for the previous DEL value. This technique is used to estimate the shift from DEL=1 to DEL=10. The optimum flow estimate is then made from these ten average shift estimates as discussed in section 5.1.

The calculation of all of the discrete correlations was done on the UDAS using the high speed correlator. The floating point calculations such as the variance of the flow estimate and the optimum flow rate estimate were done on the host computer, a VAX

11/730. About 90 seconds was required to perform the correlation calculations for 384 echoes at 25 range positions and to send the average shift data to the host computer using the UDAS.

5.3 PULSATILE FLOW MEASUREMENT METHOD

The measurement of pulsatile flow is considerably more difficult than the measurement of steady flow. Pulsatile flow is flow with a periodically varying flow rate [39]. Variation of the flow with time makes the flow estimates nonstationary, since the mean of the flow estimate is time dependent and since the variance of the shift estimates is not independent of the pair of echoes used to estimate the flow, as assumed in equation (39). However, by assumming that over a short time interval the flow does not change significantly, the flow estimates can be assumed to be stationary. Future research where pulsatile flow measurement is considered in more detail may address these assumptions and resulting problems in greater depth.

The shifts can be calculated at each DEL value from DEL=1 to DEL=10 by the algorithm illustrated in Figure 17. For pulse flow measurements, these values of shift are not averaged together but are simply sent to the host computer for further processing.

If the measurement angle and weighting function for a particular measurement are known, the optimum flow estimate can be determined. Since the flow estimates are not stationary, the estimate of the variance from the flow data as was done for steady flow is not possible. With the a priori knowledge of the weighting function determined for steady flow at the same measurement angle, the optimum flow estimate, $\hat{V}_A$, can be determined in exactly the same way as indicated by equation (42), except that the number of echoes used must be much smaller than the number used for steady flow measurements (384 using the UDAS).

If the pulse repetition rate is 5000 Hz, ten echoes represent 2 ms of time. For typical human blood flows, the pulse variation rate is never greater than 3 Hz (the human pulse rate rarely exceeds 180 beats/min). Assuming that the magnitude of the frequency components in the pulsatile flow waveform are zero above the tenth harmonic, the flow will change less than 1% during the 2 ms represented by ten echoes. Since the precision of a typical measurement is 5%, this additional 1% variation due to the time variation of the flow during the ten echoes is not significant.

The pulsatile flow measurement technique uses ten echoes for each optimum flow estimate (N=10 in equation (42)). Thus, a total of 55 shift estimates (N(N+1)/2) are used to estimate each optimum axial flow velocity by equation (42). The W(DEL) values are determined from measurements of the variance versus shift (Var[S(DEL)]) for steady flow at the same measurement angle and transducer. Further discussion of the validity of this method will be presented in Chapter 7.

CHAPTER 6

VOLUME FLOW MEASUREMENT METHOD

The measurement methods used to estimate volume flow from a collection of axial flow velocity measurements are considered in this chapter. In particular, the axial flow velocity estimates determined from consecutive echoes by time domain correlation will be used to calculate the steady flow in a round tube. The steady flow velocity of fully developed laminar flow is parallel to the vessel walls and is parabolic in shape with a peak flow velocity at the center of the vessel. For any viscous fluid, the flow at the walls must be zero [39]. Since steady, fully developed laminar flow is one of the simplest types of flow to measure and describe, it will be considered exclusively in the volume flow measurement method presented here.

A two dimensional set of constant axial velocity points is determined from a series of one dimensional axial flow velocity profiles as described in section 6.1. An elliptic fitting algorithm used to determine the position of constant axial flow velocity contours from the constant velocity points is described in section 6.2. Two different methods to estimate the volume flow from the constant velocity contours are presented in section 6.3.

The first method, called the INTEGRATED volume flow estimate, determines the size of the tube and the measurement angle from ten constant velocity ellipses. The size of the constant velocity ellipses is estimated from the velocity versus range data. The volume flow contributions from each elliptically shaped section are integrated to yield the INTEGRATED volume flow estimate.

The second volume flow estimate, called the TUBE SIZE volume flow estimate, determines the best fit ellipse of the zero velocity points. The size of this tube wall ellipse and the maximum axial velocity measurement (assumed to be at the center of the tube) are then used to form the volume flow estimate. This estimate assumes that the flow profile is parabolic and axially symmetric, that is, fully developed laminar flow.

In the remainder of this chapter, the effects of refraction on the accuracy of the volume flow estimates are described. A method to correct experimental axial flow velocity measurements for the effects of refraction is discussed in section 6.4. The results of volume flow measurement simulations used to establish the accuracy of the volume flow measurement methods are presented in section 6.5. The results of several simulations which quantify the effects of refraction on the volume flow estimates are presented in section 6.6.

6.1 TWO DIMENSIONAL CONSTANT VELOCITY POSITIONS

The method used to estimate the two dimensional axial flow velocity positions from the one dimensional axial flow velocity profiles is described in this section. The characteristics of a typical axial flow velocity profile for fully developed laminar flow in a unit radius tube is described in section 6.1.1. The results of three typical one dimensional axial flow velocity measurements are presented in section 6.1.2 in order to help illustrate the volume flow measurement method. The method used to determine a set of constant axial velocity points from the one dimensional axial flow velocity measurements is described in section 6.1.3.

6.1.1 Typical Fully Developed Laminar Flow

A perspective view of the two dimensional flow velocity field in a typical round tube with constant laminar flow is shown in Figure 18. The figure is the result of a simulation of a typical flow profile which will be measured using the time domain technique described in Chapter 5, and the flow regulation system described in Chapter 4. The flow velocity field for a unit radius tube is given by

$$V(r) = V_0(1 - r^2) \tag{59}$$

where r is the distance from the tube center and V_0 is the peak velocity at the center of a unit radius tube. Figure 18 is a two dimensional perspective representation of this flow velocity field. Along any line passing through the tube the flow velocity profile will have a parabolic shape [39] as illustrated by Figure 18. Thus, the one dimensional flow measurement method should provide flow profiles which are parabolic in shape as long as fully developed laminar flow exists.

The volume flow measurement problem is to estimate the velocity field as accurately as possible from the one dimensional flow profiles and then estimate the volume flow. Since the flow velocity is zero at the tube walls and in the region outside the tube, the two dimensional velocity field is spatially limited. If this velocity field is considered a two dimensional signal, then this continuous signal has an infinite bandwidth since it is spatially limited [45]. Because of the infinite spatial bandwidth, the spatial sampling rate used to represent this velocity field must be infinite in order to reconstruct the velocity profile exactly. Thus, any finite spatial sampling rate which can be used in practice will result in an inaccurate estimate of the flow velocity field. The accuracy of the volume flow estimate obtained from samples of the flow velocity field is one of the major objectives of the simulation results presented in section 6.5 and the experimental results to be considered in Chapter 7.

6.1.2 Typical One Dimensional Axial Flow Velocity Measurements

In order to estimate the volume flow in a round tube from one dimensional axial flow velocity measurements, it is important to examine the one dimensional axial velocity results and determine how well they fit the shape of the flow profile predicted by equation (59). Axial flow velocity measurements similar to those presented in this section can be found in [12] where buttermilk was used as a scattering fluid. More detailed discussion of the one dimensional axial flow velocity results can be found in Chapter 7, section 7.1.

Figure 19 shows three average axial flow velocity versus range measurements for a steady flow of porcine blood through a tube with a diameter of approximately 6.3 mm (21 wavelengths). Three different transducer scan angles (α) are shown, one with the beam axis through the tube center ($\alpha = 0.0^{\circ}$) and two equally spaced on each side at $\alpha = \pm 2.9^{\circ}$. In each case the measurement angle (θ) was 60°. These measurements were obtained using 384 echoes and the echo data were processed with the algorithm outlined in Figure 17. The transducer had a beamwidth of two wavelengths (0.8 mm in water) at the focus and the distance from the rotation axis to the center of the tube was 40 mm.

The two profiles at $\alpha = \pm 2.9^{\circ}$ (Figures 19a and 19c) show a decreased width and reduced flow compared to the $\alpha = 0.0^{\circ}$ profile (Figure 19b). This would be expected as the transducer is scanned away from the center of the tube. The shape of each of the three velocity profiles appears to be very close to the parabolic shape expected. In fact, second order least squares curve fitting of the data points reveals that the mean squared error between the best fit parabolic curve and the measured data is less than 2% of the average axial flow velocity in each case.

6.1.3 Constant Axial Velocity Positions

The axial flow velocity estimates versus range along the ultrasound beam are used to determine the range positions where the velocity is a given value. The ranges where the velocity is a given value are then used to generate a set of constant velocity points. As illustrated in Figure 19, the one dimensional flow measurements form parabolic velocity versus range graphs. A number of velocity values or levels are then used to develop a contour map of the flow velocity profile.

Each positive velocity level (less than the maximum) of each one dimensional measurement has two range positions where the axial velocity has the same value (see Figure 19). A spatial set of these constant velocity points is developed by converting the axial velocity versus range measurements (similar to Figure 19) to the ranges at which the axial velocity is equal to a series of velocity levels. The polar coordinates (range of a velocity level and scan angle) are then converted to rectangular coordinate values by using the known distance from the scan axis (defined in Chapter 4) to the transducer. When the positions of constant velocity values for all angular positions are plotted on a rectangular grid, a result similar to that shown with Xs in Figure 20 is obtained. Each of these Xs on the same ellipse represents the spatial position of the same velocity value.

The constant axial velocity points can now be obtained from a set of one dimensional axial flow velocity measurements. All of the constant velocity points lie in a plane defined as the measurement plane. The measurement plane is the plane which contains each of the scan lines as the ultrasonic beam moves across the vessel and is the plane shown in Figure 20. The measurement angle (θ_M) is the angle between the measurement plane and the flow velocity vector. The measurement plane is perpendicular to a plane which passes through the scan axis and the center of the vessel. The measurement plane is, therefore, perpendicular to the plane shown in the cross sectional view of the scan axis and vessel shown in Figure 11. The velocity versus range data are collected at a number of different scan angles. The velocity versus range data are then converted to range versus velocity by first finding the velocity points closest to the velocity level. Since 25 velocity versus range values are measured every 0.6 mm, four of the range values are close to a particular velocity level. Linear interpolation is then used to estimate the range location of the velocity level. The X axis in the measurement plane is defined as the beam path when the scan angle is zero. The angle, PHI, is defined as the angle in the measurement plane between the ultrasonic beam and the X axis. The angle in the measurement plane, PHI, is related to the scan angle, α, by the sine of the track setting or $(R_0 + F)/(R_Z + F)$. Figure 11 shows these three distances for the circular track. Note that R_0 is negative because the scan axis is in front of the transducer. Given the polar coordinate values (R,α) for a particular velocity level, the Cartesian coordinate values (X,Y) in the measurement plane are determined as follows:

$$PHI = \frac{R_0 + F}{R_Z + F} \alpha$$

$$X = (R + R_Z) \ Sin(PHI)$$

$$Y = (R + R_Z) \ Cos(PHI) \qquad (60)$$

where, as shown in Figure 11,

R_0 = distance from scan axis to front face of transducer at $\theta = 90^\circ$,
R_Z = distance from scan axis to front face of transducer along a path colinear with the axis of the beam, and
F = distance from front face of transducer to center of rotation of the circular track.

The value of R_Z changes depending on the position of the transducer on the circular track. The constant R_0 is determined by the machining of the circular track and the mounting of the transducer. Grooves to indicate the track setting, θ, were etched accurately on the circular track at 90°, 75°, 60°, and 45°. The accuracy of these grooves was verified by arc length and diameter measurements of the track using calipers with an accuracy of ± 0.1 mm. The track setting grooves were found to be accurate to within $\pm 1^\circ$. For the circular track used in this study, caliper measurements revealed that $F = 49.4$ mm and $R_0 = -9.5$ mm and both remained constant throughout the experiments. Measurements of the circular track with an accuracy of ± 0.1 mm have revealed the values for R_Z versus track setting shown in Table 5.

Table 5 - R_Z Measured Values Versus Track Setting.

Track Setting (Θ)	R_Z (mm)
90°	-9.5
75°	-8.1
60°	-3.3
45°	7.0

Figure 20 is an illustration of the constant velocity ellipses of steady laminar flow which exist in a round tube for a measurement angle of 45°. Seventeen different scan angles are shown with five different constant flow contours. The outer most curve indicates where the tube wall is and each concentric ellipse towards the center indicates a greater velocity. For this example, starting with the outer most ellipse and moving inward, the velocity levels represented by each ellipse are 0, 0.1 V_0, 0.3 V_0, 0.5 V_0, and 0.7 V_0. The area inside the center ellipse represents where the velocity is greater than 70% of the maximum value.

The simulated constant velocity ellipses shown in Figure 20 are what would be expected from an ideal round tube scanned by an ideal ultrasonic measurement system at a 45° measurement angle. In an actual experiment, data similar to the data presented in Figure 19 were used to determine the volume flow. The volume flow estimate must be determined completely from the constant velocity points obtained from the ultrasonic measurements. The main assumption made in the development of the volume flow estimates used in this research is that the vessel has a circular cross section. Since the vessel is assumed to be circular and the axial velocity measurements are made at an oblique angle, the constant velocity contours form a set of constant velocity ellipses as shown in Figure 20. Thus, in order to estimate the volume flow, the vessel size, measurement angle, and the axial flow velocity field must all be estimated from the ultrasonic measurements. The elliptic fitting algorithm used to estimate the size and orientation of the constant velocity ellipses from the constant velocity points is described in the next section. The methods used to determine the volume flow from the size of the constant velocity ellipses are considered in section 6.3.

6.2 ELLIPTIC FITTING ALGORITHM

This section contains the details of the algorithm used to obtain the parameters of the constant velocity ellipses (size, position, and orientation) from the ultrasonic axial velocity flow measurements. For a tube with a perfectly circular cross section and constant laminar flow, the constant velocity curves form a set of concentric ellipses when the measurement plane is at an oblique angle. The data points measured by ultrasound represent only a portion of each ellipse. Within the section of the ellipses near the tube wall which are nearly parallel to the beam, no ultrasonic measurement of the velocity can be made because most of the ultrasonic energy is reflected away from the vessel by the tube wall.

The minor axis of each constant velocity ellipse represents the diameter of the region in the tube where the flow velocity is greater than the particular velocity level. The minor axis of the ellipse at a zero velocity level is the diameter of the tube. Since the minor axes of all of the constant velocity ellipses are nearly perpendicular to the ultrasonic beam (see Figure 20), it is not possible to directly determine the dimensions of the tube or the constant velocity ellipses. Other scanning geometries, such as a transducer which moves around the center of the tube or a transducer which moves along the circular track, could be used to directly measure the tube dimensions. Since these scanning methods are much more complicated and require additional motion of the transducer, such scanning methods are not practical for blood flow measurement in the human body and will not be considered here. It is therfore important to estimate the dimensions of the constant velocity ellipses from a limited number of scan angles in the geometry illustrated in Figure 20.

One way to estimate the dimensions of the constant velocity ellipses is to fit an elliptical curve to the data points. Although this is somewhat difficult to accomplish for the general case of arbitrarily distributed data points, many simulations have shown that a typical ellipse can be fitted by least squares curve fitting.

Figure 21 shows a flow chart of the elliptic fitting procedure. The equation of an ellipse which is rotated by ANG with a center at (X_o,Y_o) and axis lengths 2a and 2b is as follows:

$$A(X - X_o)^2 + 2\,B\,(X - X_o)(Y - Y_o) + C(Y - Y_o)^2 = 1 \qquad (61)$$

where

$$A = \frac{\cos^2(\mathrm{ANG})}{a^2} + \frac{\sin^2(\mathrm{ANG})}{b^2}$$

$$B = \sin(\mathrm{ANG})\,\cos(\mathrm{ANG})\,(\,b^{-2} - a^{-2})$$

$$C = \frac{\cos^2(\mathrm{ANG})}{b^2} + \frac{\sin^2(\mathrm{ANG})}{a^2}$$

A typical example of an ellipse described by the above equation is shown in Figure 22 in which the five parameters (a, b, X_o, Y_o, and ANG) are graphically defined.

The elliptic fitting problem is to estimate A, B, C, X_o and Y_o from the experimental (x_n, y_n) data. The rotation angle, ANG, is the most difficult parameter to estimate, since for a nonzero rotation angle (ANG $\neq$ 0), the cross product term B is nonzero. Thus, a simple way to estimate the rotation angle is to rotate the data by -ANG and determine how well the data fit an unrotated ellipse (B=0). By trying a series of ANG values, the rotation angle can be estimated. The procedure illustrated in Figure 21 evaluates 21, one degree increments from -10^o to $+10^o$. A measure of the difference between the N data points $(x_n, y_n;\ 0 \leq n \leq N-1)$ and the best fit unrotated ellipse is the mean square error (MSE) defined as follows:

$$\mathrm{MSE} = \frac{1}{N} \sum_{n=o}^{N-1} (y_n - Y_o \pm b \quad 1 - a^{-2}(x_n - X_o)^2\ )^2 \qquad (62)$$

where the sign in equation (62) is determined from (1) the geometry and (2) the sign of $(x_n - X_o)$. The value of ANG which has the lowest MSE is used as the final estimate of the rotation angle.

The other four parameters (X_o, Y_o, a, b) are estimated by the iterative technique illustrated in Figure 21. The first center estimate is determined from the mean of the x_n and y_n data points,

$$(X_o,\ Y_o) = \left(\frac{1}{N} \sum_{n=0}^{N-1} x_n\ ,\ \frac{1}{N} \sum_{n=0}^{N-1} y_n \right) \tag{63}$$

This initial center estimate requires that the data points are reasonably evenly distributed on both sides of the ellipse. If only one side of the ellipse were represented by the data, then a large error in this initial guess of the center would result. Since the center estimate is subtracted from the data before least squares curve fitting, the iterative technique may not converge to the proper values if the initial center estimate is not close to the actual center. Extensive simulation of the elliptic fitting procedure has revealed that as long as some of the data points represent both sides of the ellipse and at least five data points are used, the procedure converges to the correct center solution (within 1% of the actual value). If fewer than five data points are used, the parameters determined by the procedure are not unique (five parameters are being determined) and the values obtained from the algorithm are then unpredictable. A simulation of the overall accuracy of the volume flow method including the elliptic fitting procedure will be discussed in section 6.5.

The next step in the procedure is to assume that one of the center coordinates is zero and fit the square of the data points versus the other coordinate by second order least squares. For example, if $X_o=0$, the data (x_n^2, y_n) are a parabolic curve. Figure 23 illustrates this case. The unrotated ellipse shown in Figure 23 has $(a, b, X_o, Y_o) = (1.5, 2.0, 0.0, 0.1)$. The curve (x^2, y) is a parabola and (y^2, x) is composed of two parabolic curves which are superimposed. The fit of (x^2, y) yields estimates of A0, A1, and A2 of $x^2 = A0 + A1\ y + A2\ y^2$. The A0, A1, A2 values can be used to determine Y_o, a, and b as shown in the flow chart. This Y_o value is subtracted from the data and a fit of (y^2, x) is then used to estimate X_o, a and b. The X_o value is then subtracted from the x_n data points. The least squares fit and center subtraction are repeated ten times for each angle. This number of iterations was found to be sufficient for convergence of the a, b, X_o, and Y_o values to within 1% of the correct values in all of the simulations. As shown in Figure 21, after each least squares estimate of a and b, the MSE is again estimated according to equation (62). If the current MSE is lower than all previous MSE values (MSEMIN), the current values of a, b, X_o, Y_o, and ANG replace the final values passed to the calling program. Since 420 (21 different ANG values and 20 curve fits for each angle) least squares second order curve fits must be performed for each elliptic fit, the time to determine the parameters of one 30 point ellipse was 7 seconds on the host computer (VAX 11/730). The five parameters passed to the calling program are the estimate of (a, b, X_o, Y_o, ANG) for ANG= -10^o to 10^o with the smallest mean squared error.

6.3 VOLUME FLOW ESTIMATES

The constant velocity ellipses obtained with the elliptic fitting algorithm described in the last section can now be used to estimate the volume flow. The set of parameters obtained from each constant velocity ellipse provides a great deal of information about the two dimensional flow velocity field. The estimation of volume flow from the parameters obtained from elliptical curve fitting is described in this section. Estimates of the measurement angle, tube size, and constant velocity ellipse parameters can be used to determine two volume flow estimates, namely the INTEGRATED and TUBE SIZE estimates.

The center, angle of rotation, and major and minor axes of each elliptical estimate of constant velocity contour are determined by the elliptic fitting algorithm. The measurement angle was constant for all of the constant velocity levels so that the ratio of the axes of the ellipses (or the aspect ratio) should be approximately the same. However, because of the variation in the experimental axial velocity measurements, each resulting constant velocity ellipse will not have the same aspect ratio. An average of the measurement angle estimates obtained from each ellipse may provide a good measurement angle estimate. The average measurement angle estimate is given by

$$\theta_M = \frac{1}{M} \sum_{n=0}^{M-1} \mathrm{Sin}^{-1}\left[\frac{a_n}{b_n}\right] \tag{64}$$

where a_n is half the minor axis length (see a and b in Figure 22) and b_n is half the major axis length of the n^{th} constant velocity ellipse. A total of M ellipses are determined with the first and largest ellipse, representing the wall, where the flow velocity is estimated to be zero, having n=0. The volume flow can be estimated by numeric integration as follows:

$$Q = \frac{\pi}{3} \sum_{n=1}^{M-1} \frac{(V_n - V_{n-1})\ (a_{n-1}{}^3 - a_n{}^3)}{(a_{n-1} - a_n)\ \cos(\theta_M)} + \frac{\pi a_{M-1}{}^2 (V_{max} - V_{M-1})}{2\ \cos(\theta_M)} \quad (65)$$

where

Q = total volume flow (m^3/sec),
a_n = half of the minor axis of ellipse n,
b_n = half of the major axis of ellipse n,
V_n = axial velocity level of ellipse n (m/s),
V_{max} = maximum axial velocity value of all one dimensional measurements (m/s), and
M = number of constant velocity ellipses.

Equation (65) approximates the volume of each layer as the bottom circular section parallel to the base of a right circular cone as illustrated in Figure 24. Each of the M-1 layers is added in the first term of equation (65). The thickness of the layer is determined by the difference in the velocity levels (V_n-V_{n-1}) and the minor axes of the ellipses determine the size of the top and bottom surfaces of the circular conic section. The approximation assumes that the flow between constant velocity ellipses increases in a linear fashion. Equation (65) assumes that the velocity values of the ellipses are ordered from the smallest (V_o) to the largest (V_{M-1}) and that the size of each ellipse is smaller than the previous ellipse.

A simulation of the errors associated with equation (65) (to be disscused in section 6.5) has shown that M=10 provides an accurate estimate of the flow to within ± 2%. Given that M=10, the first term of equation (65) is the flow due to all of the nine conic slices from the wall to 90% of the peak flow. The flow levels were chosen at multiples of 10% of the peak axial flow velocity (V_{max}), or $V_n = 0.1\ V_{max}$. The peak flow (V_{max}) is the maximum axial flow velocity of all of the one dimensional measurements. The second term is the additional flow due to the difference between the maximum flow (V_{max}) and the highest constant velocity ellipse value (V_{M-1}). The shape of this top section, as illustrated in Figure 24, is assumed to be parabolic and axially symmetric. Since the V_{M-1} ellipse is the smallest ellipse, it represents the smallest contribution of the total flow, Q. The largest contribution is from the first and largest section. Thus, from many one dimensional flow measurements, the total flow may be estimated without prior knowledge of the vessel size, or transducer orientation. When equation (65) is used to estimate the volume flow and M=10, the result will be called the INTEGRATED volume flow estimate.

The time required to determine the parameters of the ten ellipses and the total volume by equation (65) is rather long (78 seconds on the host computer). Since computationally simpler volume flow estimates than that obtained using ten ellipses (M=10) require less time, it is intriguing to determine the accuracy of other simpler volume flow estimates. Another estimate of the volume flow can be obtained by using only the last term in equation (65) and $V_{M-1}=0$. Thus, the entire flow profile is assumed to be parabolic and axially symmetric. This simpler estimate is obtained by setting M=1 in equations (64) and (65) and will be called the TUBE SIZE volume flow estimate. The measurement angle must still be determined by equation (64) and the tube radius (a_{M-1} or a_0) must be determined by elliptic fitting the tube wall data points. The accuracy of this TUBE SIZE flow estimate and the INTEGRATED flow estimate determined from a ten layer integration (M=10 in equation (65)) will be compared in the next chapter.

6.4 ERRORS DUE TO REFRACTION

When the speed of sound in the flowing fluid is different than the speed of sound in the surrounding medium, the ultrasonic beam bends due to refraction. Although this effect should not be significant for Sephadex^R flow experiments (because the speeds are nearly the same, see section 4.6.2), the speed of sound in porcine blood (1.55 mm/μs) was different from the speed of sound in the surrounding medium (normal saline was used in blood flow experiments with a speed of sound of 1.51 mm/μs). The methods used to address the problems caused by the refraction of the ultrasonic beam are described in this section. A simulation will be used to show the change in the beam direction due to refraction in section 6.4.1. Also, a method which can correct the experimentally measured data for the effects of refraction will be considered in section 6.4.2.

6.4.1 Refraction Simulation

Figure 25 shows a schematic representation of an ultrasound beam (in terms of ray theory) incident at an oblique angle, θ_I, on the round tube. If the beam size is small compared to the size of the tube, Snell's law can be used to predict the path of the refracted beam. Since Cartesian coordinates are used throughout this discussion, the formulation of the direction of the beam is easier to express in terms of the slopes (dY/dX) of the beam and tube wall instead of angles between them. The angle between the incident beam (slope M1) and the tube wall (slope M2) is θ_I. The angle between the tube wall (slope M2) and the refracted ray (slope M3) is θ_M. By using the dot product of the vectors, the following relations between the angles and the slopes can be derived:

$$\cos(\theta_I) = \frac{1 + M1\ M2}{\sqrt{(1 + M1^2)(1 + M2^2)}} \tag{66}$$

$$\cos(\theta_M) = \frac{1 + M3\ M2}{\sqrt{(1 + M3^2)(1 + M2^2)}} \tag{67}$$

By Snell's law,

$$\frac{\cos(\theta_M)}{\cos(\theta_I)} = \frac{c_1}{c_0} \tag{68}$$

where c_1 is the speed of sound in the medium inside the tube and c_0 is the speed of sound in the surrounding medium. By using equations (66), (67) and (68), a relationship can be derived between M3 and M1 in terms of M2. The result is,

$$M3 = \frac{-M2 \pm \sqrt{C\ (M2^2 - C + 1)}}{M2^2 - C} \tag{69}$$

where

$$C = \frac{c_1^2\ (1 + M1\ M2)^2}{c_0^2\ (1 + M1^2)} .$$

The sign in equation (69) must be determined from the geometry of the system. For the case illustrated in Figure 25, the positive sign is correct.

Figure 26 shows simulation results for cases with the transducer perpendicular to the flow direction for c_1/c_0 equal to 0.90 and 1.10. For an index of refraction greater than one, the rays bend away from the tube (Figure 26a). An index of refraction less than one causes the rays to bend inward toward the tube center (Figure 26b). In both cases, a total of 17 scan angles were simulated and the transducer was at (-12, 0) or 12 units away from the center of the unit radius tube. This relative transducer location is typical for the experimental measurement to be considered in the next chapter. The dashed lines beyond the back wall of the tube indicate the path of the ultrasound beam in the tube. Since the path of the ultrasound beam beyond the back wall does not produce a backscattered signal, the refraction at the back wall was not simulated. Figure 26 illustrates the rather large change in the direction of the ultrasonic beam when only a 10% change in the speed of sound occurs.

6.4.2 Refraction Correction

Axial flow velocity measurements of fluids with a different speed of sound than the surrounding fluid have the same parabolic flow profile as measurements of fluids with no refraction effects. The path of the refracted ultrasonic beam inside the tube is straight but in a different direction than the incident beam. Thus, the width of the flow profile and the magnitude of the velocities are different than what would be expected if the bending of the ultrasonic beam were not included in the analysis of the experimental data. In order to obtain accurate flow estimates for experiments where refraction effects are important, some method to correct the experimental data for the refraction effects is required.

Since the incident angle (Θ_I) between the ultrasonic beam and the tube wall is unknown for a particular scan angle, it must be determined from the ultrasonic data. By determining the front wall locations from the experimental data, an initial estimate of the incident angle in the measurement plane can be obtained. An iterative method can then be used to estimate the incident angle for each scan angle. Then, by using the measured values of the speed of sound in the materials used in a particular experiment, the ultrasound beam direction inside the vessel can be determined. The following steps were used to correct the experimental axial flow velocity measurements for the effects of refraction:

1. Locate the front wall from one dimensional velocity estimates assuming constant speed of sound (c_0) for entire range. The wall location is extrapolated from a second order least squares fit of the one dimensional velocity values, as was described in section 6.1. The location of the front wall should not be affected by a different speed of sound inside the tube.

2. Correct the one dimensional estimate by using c_1 for the speed of sound for range cell locations after the front wall position determined above.

3. Determine the intial elliptic fit of front and back wall data using the corrected one dimensional results. This wall estimate is used as an initial guess of the front wall where the refraction of the beam occurs.

4. Using the slope of the front wall of the wall ellipse, correct the path of the ultrasonic beam using equation (69) and determine the location of the refraction corrected back wall.

5. Using the new back wall estimates, determine the best fit ellipse for the tube wall. These tube wall values replace the old wall ellipse values.

6. Repeat steps 4 and 5 until the size of the wall ellipse does not change significantly (less than 1% change in the a_0 value). For refraction indices as large as 1.15, eight iterations of steps 4 and 5 were sufficient. Additional

iterations did not change the a_0 value or the wall ellipse estimate. For small refraction indices (1.05 or less), only three iterations were required because the slope of the refracted ray was very close to the slope of the incident ray.

7. Using the final wall ellipse estimate, correct the path of scan lines according to Snell's law (equation (69)) and the slope of the final wall ellipse at the front wall.

8. Elliptic fit all constant velocity data points using the corrected ultrasound beam path. Calculate the volume flow estimate using equation (65).

6.5 VOLUME FLOW MEASUREMENT SIMULATION

In order to determine the validity of the assumptions made in this chapter, simulated data at different measurement angles were generated and used to verify the operation of the program which implements the volume flow estimate from experimental data. Figure 20 is a result of one such simulation. Parabolic, axial symmetric flow velocities according to equation (59) were simulated.

The simulation program generated data in exactly the same format as the data generated by an experiment. For each measurement angle, 13 scan angles evenly distributed across the vessel were simulated. After the measurement angle was entered by the user, the simulation program generated all of the 25 velocity versus range values for all 13 scan angles and wrote there data to a data file. This data file was then read by the same analysis program as is used to read the experimental data files. In the simulation, the value of R_0 was set to -9.5 mm in order to be consistent with the experimental value. The value of R_Z was calculated by the simulation program for the particular measurement angle (see section 6.1 for definitions of R_0 and R_Z). The R_Z value must be entered into the analysis program by the user after the simulation program has generated the data to be analyzed.

Four different measurement angles were simulated. The maximum axial flow velocity in each case was fixed at 0.1 m/s for $\theta = 30^o, 45^o, 60^o$, and 75^o. The tube diameter was 7.5 mm and the tube axis was 50 mm away from the scan axis along the ultrasound beam. The results of these simulations showed that ten velocity levels (M=10) are sufficient to provide a volume flow measurement accuracy of within 2% for all three measurement angles. The simulated volume flow values were different for each measurement angle ($Q = \pi r^2/20 \cos(\theta)$ m^3/s, where r is the tube radius, 3.75 mm). The simulated volume flow, the estimated value of the measurement angle, TUBE SIZE flow estimate, and INTEGRATED flow estimate (by equation (65) with M=10) and the errors associated with the flow estimates are shown in Table 6.

Table 6 - Volume Flow Measurement Simulation Results.

	Simulated	Angle	TUBE SIZE		INTEGRATED	
θ	Flow	Estimate	Flow	Error	Flow	Error
30	153.0	30.1	152.9	-0.1	153.1	0.0
45	187.4	44.9	188.4	0.5	185.9	-0.8
60	265.1	59.7	270.0	1.9	260.3	-1.8
75	512.1	75.0	525.4	2.6	510.3	-0.4

As shown in the table, the measurement angle estimates are within ± 0.3^{o} of the correct simulated value, and the INTEGRATED flow estimates were within ± 2% of the correct simulated value. The TUBE SIZE flow estimates (M=1) were within ± 3% of the correct simulated value. Also, the flow estimates for larger measurement angles (60 and 75^{o}) were less accurate than for 30 and 45^{o}. This effect is due to the fact that fewer nonzero data points were present in the simulations of 30 and 45^{o} measurement angles. Also, the error in the measurement angle at 60^{o} caused a significant portion of the error in the flow estimates. The more data points used to estimate the volume flow estimate, the more accurate the estimate became. This effect is representative of what would be expected from the experimental results as well.

6.6 REFRACTION SENSITIVITY OF VOLUME FLOW MEASUREMENTS

The bending of the ultrasonic beam caused by refraction (as illustrated in Figure 26) at the interface of the scattering media with the surrounding media results in the ultrasonic beam sampling different axial flow velocities than would otherwise be sampled if the beam path were straight. This section describes a computer simulation intended to quantify the effects of refraction on the INTEGRATED volume flow estimate at several measurement angles.

One way to quantify the refraction effect is to determine the sensitivity of a simulated flow measurement to small changes in the speed of sound. The sensitivity, S, of the volume flow estimate to changes in the speed of sound of the flowing fluid is defined as follows:

$$S = \frac{\Delta Q/Q}{\Delta c_1/c_1} \tag{70}$$

where the Δ symbol indicates the change in the quantity, Q is the volume flow, and c_1 is the speed of sound in the flowing fluid. The sensitivity, S, indicates the percent change in the volume flow estimate due to a one percent difference in the speed of sound in the flowing fluid. Since both the numerator and denominator of equation (70) are relative changes in each quantity; the sensitivity, as defined here, is a unitless ratio.

By using the simulated volume flow measurement data (which were used in the simulation described in section 6.5) and the refraction correction program, the sensitivity can be estimated for different measurement angles. For this simulation the value of c_0 (speed of sound in the surrounding medium) was set to 1.5 mm/us. The simulated volume flow data were generated as described in section 6.3. For each measurement angle, 13 scan lines of experimental data were simulated. The speed of sound in the flowing fluid (c_1) was then changed a small amount (± 1%) and the sensitivity of the INTEGRATED volume flow estimated was determined. Measurement angles of 30, 45, 60, and 75° were simulated. The refraction program was then used to determine the volume flow estimate at three different values of c_1 for each of the four simulated measurement angles. Table 7 shows the INTEGRATED volume flow estimate results for these four cases for c_1= 1.485, 1.500, and 1.515 mm/µs (12 total cases). The calculated sensitivities for this ± 1% variation about the value of 1.5 mm/µs are shown in the last column.

Table 7 - Sensitivity of Flow Measurement to Variations in c_1.

Measurement Angle	INTEGRATED Volume Flow c_1=1.50	c_1=1.485	c_1=1.515	Sensitivity
30	153.3	136.8	169.4	10.6
45	186.4	174.4	198.7	6.6
60	263.7	250.2	277.9	5.2
75	514.2	484.2	547.4	6.1

The simulation results shown in Table 7 indicate that the sensitivity of the volume flow estimate changes with measurement angle. A larger sensitivity value indicates a greater effect on the volume flow estimate due to changes in c_1. The simulation indicates that at a 30^o measurement angle the sensitivity is worse than the sensitivity at 45^o, 60^o, or at 75^o. This is because the change in the beam direction due to refraction is much more significant when the measurement angle is small. When the measurement angle becomes as large as 75^o the sensitivity again increases because the change in the relative dimensions of the constant velocity ellipses begins to dominate the changes in the volume flow estimate. This is because the measurement angle is estimated from the ratio of the axes of the ellipses by equation (64).

The scan geometry used in the experiments and the simulation tends to make the major axis larger with little change in the minor axis. At 75° the major axis of each ellipse is only 3.5% larger than the minor axis of each ellipse. This causes the estimated measurement angle for the 75° case to change by 0.8° for a 2% variation in the speed of sound of the flowing fluid. This small change in the estimate of the measurement angle causes a large change in the flow estimate (5.3%). The precision of the axial velocity measurements also decreases greatly as the measurement angle approaches 90° and the measured axial velocity approaches zero. It is, therefore, unlikely that reasonable volume flow estimates could be obtained when refraction is important and the measurement angle is close to 90°.

Thus, refraction causes two major effects on the volume flow estimate. First, the change in the speed of sound in the flowing fluid changes the estimate of the dimensions of the constant velocity ellipses. This effect is most important at large measurement angles (75°) because the volume flow estimate changes greatly for small changes in the ratio of the axes of the ellipses. Second, the bending of the ultrasonic beam changes the axial flow velocities which are sampled by the one dimensional axial velocity measurements. This effect is most important at small measurement angles (30°) where the change in the beam direction is more severe than at large measurement angles (75°).

CHAPTER 7

RESULTS AND DISCUSSION

The experimental results obtained with the measurement system and the time domain correlation flow measurement method are presented in this chapter. Axial flow velocity results for steady flow will be described in section 7.1. Volume flow measurement results for steady flow will be discussed in section 7.2 and axial flow velocity measurement results for pulsatile flow will be presented in section 7.3.

7.1 AXIAL FLOW VELOCITY RESULTS

The axial flow velocity results calculated by the UDAS and sent to the host computer for further analysis and graphical display are presented in this section. All measurements in this section were obtained using an aqueous suspension of Sephadex^R as a blood mimicking substance. The axial velocity versus range measurements are presented and discussed in section 7.1.1. Results concerning the precision of the time domain correlation technique are presented in sections 7.1.2 and 7.1.3. The precision of the time domain technique is compared with the precision of Doppler flow measurement methods in section 7.1.4.

7.1.1 Typical One Dimensional Flow Measurement Data

Detailed results for a typical one dimensional axial flow velocity versus range measurement are presented in this section. A series of these one dimensional axial flow velocity measurements are combined together in order to estimate the total volume flow as indicated in Chapter 6. It is, therefore, important to discuss and examine the axial flow velocity measurements before considering volume flow measurement results.

Figure 27 shows a typical set of one dimensional average time shift measurements of an aqueous suspension of Sephadex^R flowing at a hydrodynamically determined flow rate of 153 ml/min. Flow conditions were such that fully developed laminar flow existed for this ultrasound axial flow velocity measurement. The measurement angle was 45^o and the ultrasonic beam intersected the vessel close to the center of the tube where the flow velocity was greatest. Figure 27b shows the average time shift between consecutive echoes versus 25 range positions for all ten DEL values ($1 \leq DEL \leq 10$). As defined in Chapter 5, DEL is the number of pulse repetition periods (T) between the pair of echoes correlated with each other. At each range, the average time shift value (in samples) for each DEL value was determined from 384 consecutive echoes ($N = 384$) and then each average value was divided by DEL for ease of comparison of the averages. As can be seen in Figure 27b, all ten average time shift curves for each DEL value lie nearly on top of each other (within ± 0.1 samples).

The upper plot, Figure 27a, shows the precision versus range of all ten time shift estimates. Each of these curves is determined from the variance of the shift estimates and the average shift at each range. The sum of the squares of the shift estimates and the sum of the shift estimates were calculated for all 25 ranges by the UDAS average shift program (see Figure 17) and then sent to the host computer. The host computer calculated the standard deviation, average shift and the resulting precision value (standard deviation divided by average shift) for each range. The precision curves indicate that at the peak of the axial flow velocity profile, the precision of each of the average time shift estimates was approximately the same. The largest standard deviation occurred for the estimate with DEL=1 which is the smallest time shift between echoes. Close to the walls, the precision value generally exceeded 50% (values above 50% are clipped to and plotted as 50%). This is primarily because a range of axial flow velocities was present in each 0.6 mm wide range cell (40 samples). Thus, as the velocity gradient increases near the tube wall, the variance of the flow estimate increases.

Although it is difficult to theoretically determine the quantitative effects of velocity gradients on the variance of the ultrasonic axial flow velocity measurement, the trends illustrated in Figure 27a can be explained. As the ultrasonic wave travels through the scattering liquid, the backscattered signal is determined by the size and relative location of the individual scatterers. Scatterers within a range cell which happen to produce a larger backscattered signal in a particular pair of echoes will tend to make the axial velocity estimate biased toward the axial velocity of these large signal scatterers. As new scatterers move into the range cell, the axial velocity estimated by the time domain correlation method will vary in a random fashion due to the distribution of velocities in the range cell. The distribution of velocities in a range cell changes greatly depending on the position of the range cell within the tube. At the center of the tube the variation of the velocities within a range cell is small because the flow is nearly constant at the peak of the parabolic profile. Near the tube walls, the variation of the flow velocities is greatest since the slope of the flow profile has the largest magnitude. Future research should investigate the quantitative effects of flow velocity gradients on the precision of the axial velocity estimates.

The experimental data presented in Figure 27 can be used to obtain the optimum axial flow velocity estimate by the procedure described in section 5.1. Also, the variance of the flow estimates can be used to determine the weighting functions used to estimate the optimum axial flow velocity at all 25 ranges. For each one dimensional axial velocity measurement, a pair of plots similar to Figure 27 and a set of plots similar to Figure 28 were generated. Figure 28 shows a set of plots obtained from the same 384 echoes as were used to generate Figure 27. Figure 28 displays the experimental data in a way which can be used by the investigator to determine the overall results of one axial velocity versus range measurement. The bottom plot shown in Figure 28d is the optimal axial flow velocity estimate determined by weighting the ten average shift estimates (the procedure is described in section 5.1). A least squares second order fit of these optimal velocity values versus range was used to determine both the position of the front and back walls and the velocity points nearest to the walls. Two velocity points, one at range greater than the front wall and one at a range less than the back wall, were determined by second order least squares extrapolation. The positions of the front and back walls were used to estimate the tube size, which was required later to estimate the total volume flow. Since the flow velocity outside the tube was zero for the experimental arrangement, and the flow velocity profile should be parabolic in shape (because fully developed laminar flow should be present), a second order least squares extrapolation of the velocity measurements near the walls provided more realistic flow velocities. Without extrapolation, the flow velocity tended to increase beyond the range of the back wall due to multiple reflections of the ultrasonic beam within the vessel. This is indicated in Figure 28 for ranges greater than the back wall position (about 50.3 mm for data shown in Figure 28).

Also, at ranges less than the front wall position (about 40.2 mm in Figure 28), the optimal axial velocity was nonzero because the width of the ultrasonic beam causes an averaging of the flow velocities in the 0.6 mm range cell. In this region near the front wall, the ultrasonic beam intersects a region of the vessel with a nonzero average flow velocity; thus, the measured values were nonzero as is observed in the shape of the flow velocity measurements at ranges near 40 mm in Figure 28. This effect was also noted and described in some detail by Foster [12]. Also, the backscattered signal near the front wall was approximately equal to the noise level resulting in very large precision values as indicated by the precision curves in Figure 27a.

Figure 28c shows the precision of the optimum velocity estimate and the precision of the average time shift estimate with the lowest precision value. The BEST DEL velocity estimate precision (also shown in Figure 28c) is the lowest precision value of the ten time shift estimates at each range. It is the lowest precision value shown in Figure 27a for each range. The precision of the optimal velocity estimate at the peak axial velocity was approximately 3%, indicating some improvement in the precision of the optimal estimate when compared to the precision of the BEST DEL velocity estimate (about 5%).

Figure 28b shows the DEL value with the lowest precision value versus range. The BEST DEL value is an integer from one to ten and indicates the change in the time shift which has the lowest precision value. The BEST DEL curve can be used to help the experimenter set the pulse repetition period to a value which provides the most precise optimal axial velocity estimate. If the BEST DEL value is large (8-10) for all ranges, then the pulse repetition period is too large and should be reduced in order to obtain more precise axial flow velocity results. On the other hand, if the BEST DEL value is low (1-5 for all ranges), then the pulse repetition period should be made larger for best performance. As shown in Figure 28b (a proper pulse repetition period), the BEST DEL value should be small (1-3) for the higher axial flow velocities near the center of the tube where the average time shift between echoes is greater, and large (7-10) for the smaller axial flow velocities near the walls.

The upper most plot (Figure 28a) shows the received power (expressed in dBm, reference 1 mW into a 50 ohm impedance) of the echoes versus range. The received echo power at the A/D converter can be determined by calibrating the full scale A/D level (127) to represent a 0.5 V level and then calculating the sum of the squares of the echo samples. All of the echoes are 40 samples long and are stored in the UDAS memory in two's-complement form. The received input power level in dBm can then be expressed as,

$$\text{POWER} = 10 \, \text{Log}_{10}\left[\frac{1}{127^2 \; 8 \; N} \sum_{j=1}^{N} \sum_{i=1}^{40} E(i,j)^2\right] + A - G \quad (71)$$

where $E(i,j)$ is the i^{th} sample of the j^{th} echo sampled by the A/D converter $(-128 \leq E(i,j) \leq 127)$, N is the number of echoes (384 for the example shown in Figure 29), A is the attenuation added by the programable attenuator (0-63 dB) and G is the gain of the wideband amplifier (50 dB for these experiments). This discrete estimate of the power or variance of the echoes assumes that the A/D converter offset is adjusted so that the mean of the samples is zero. Thus, the POWER values plotted in Figure 29 indicate the average echo power present at the output of the receiver at each of the 25 range positions.

The signal-to-noise ratio for a particular experiment is estimated from the difference between the power from echoes within the vessel and the noise power outside the vessel where the signal is zero. The signal-to-noise ratio indicated in Figure 29 is approximately 15 dB. Other experiments with Sephadex^R have indicated that signal-to-noise ratios of as high as 22 dB can be obtained. Variations in the size of the Sephadex^R particles and the particle concentration for each experiment may be responsible for the variation of the received signal level. The noise level of the measurement system was about -70 dBm and caused by noise sources within the pulser-receiver (the noise level of the wideband amplifier alone was -95 dBm). Thus, the signal-to-noise ratio could be improved by improving the pulser-receiver design so that less noise was generated or a larger pulse was transmitted. Perhaps an order of magnitude reduction in the precision value of the axial flow velocity measurements could be obtained by noise reduction alone. Future research may require the pulser-receiver to be improved so that a better signal-to-noise ratio and therefore more precise measurements can be obtained.

7.1.2 Measurement Precision And Optimum Weighting Function

The experimental results of several midstream flow measurements which were intended to establish the precision of the time domain correlation method under different experimental conditions are presented in this section. The optimum weighting functions (see section 5.1) which were calculated from the precision values are also reported for the transducers used in this study. Figures 29, 30 and 31 show the precision and resulting weighting functions obtained from midstream constant flow measurements using the three transducers (see Table 3) at several different measurement angles.

Figure 29b shows the precision versus shift for measurement angles of 45, 60, and 75°. The large size of transducer one (27 mm outside diameter) and the mounting structure prevented measurement angles less than 45°. At a 45° measurement angle the minimum precision (5%) occurred at approximately 140 ns of time shift. Larger measurement angles had a larger minimum precision value. The minimum precision also occurred at a smaller shift as the measurement angle increased. The experimental results shown in Figure 29b can be compared to the theoretical precision relationships which were developed in section 3.2 and represented in Figure 8. The bandwidth (2.5 MHz), signal-to-noise ratio (20 dB), and beamwidth (0.6 mm) for these experimental results are similar to those used to generate Figure 8. Figure 29b indicates a slightly larger minimum precision value (5%) than Figure 8 (4%) possibly due to velocity gradients. The time shift of the minimum precision is at a larger value in Figure 8, presumably because of the simple linear approximations used in developing the theory. However, the overall shape of the theoretical precision relationships and the experimentally measured precision curve are similar.

The theoretical precision curve (Figure 8) indicates a minimum precision of 4% for $\Theta = 45^o$, 7% for $\Theta = 60^o$ and 15% for $\Theta = 75^o$. The experimental precision results (shown in Figure 29b) indicate a minimum precision of 5% for $\Theta = 45^o$, 8% for $\Theta = 60^o$ and 17% for $\Theta = 75^o$. Thus, in all three cases, the experimental minimum precision value was greater than the theoretical precision value. Since considerable approximations were made in developing the theory (such as ignoring the second order noise terms) it is remarkable that the minimum precision values are within 2% of each other. The precision value versus time shift indicated by the experimental result appears to increase more gradually with time shift indicating that the linear decorrelation of the echoes assumed in the theory may be an oversimplification.

Figure 30b shows a precision of a midstream flow measurement versus shift curve for transducer two (12.7 mm aperture and a 5 MHz center frequency). Since the aperture diameter of transducer two is half that of transducer one, the beamwidth at the focus is twice as great. The wider beamwidth caused the minimum precision to be lower (3% versus 5%) than the minimum precision shown in Figure 29b for a 45^o measurement angle. The time shift where the minimum time shift occurred was nearly twice as great as that for transducer one (140 ns for transducer one versus 250 ns for transducer two both at 45^o). Because the scatterers stay in the beam for a longer period of time, a more precise estimate of the flow velocity was obtained. The smaller size of transducer two also allowed flow measurements at 35^o

giving a minimum precision of about 2.5% at a 250 ns time shift.

Figure 31b illustrates the effect of increasing the bandwidth of the ultrasonic pulse by using transducer three. Transducer three has the same aperture diameter and almost the same quality factor (see Table 3) as transducer one. Since the center frequency of transducer three is 10 MHz, its bandwidth is about twice the bandwidth of transducer one. The minimum of the precision curve (Figure 31b) at a 45° measurement angle is again lower (3% at 130 ns) than the minimum precision obtained using transducer one (5% at 140 ns). The experimental precision versus time shift relationship for this case is again similar to that predicted by theory.

Thus, the experimentally determined precision curves seem to agree with the theoretical precision relationship derived in Chapter 3. The precision results obtained for the three different transducers demonstrate two effects on the precision of the time domain correlation method. First, increasing the bandwidth of the received echoes improves the precision of the axial flow velocity estimate at all measurement angles. Second, increasing the width of the ultrasonic beam by changing the aperature size of the transducer also improves the precision of the axial flow velocity estimate.

The weighting functions, shown in Figures 29a, 30a, and 31a for each transducer was calculated from the variance of the flow estimate at each shift as discussed in section 5.1. Each variance estimate was determined from 6144 echoes (64 bytes each) in order to obtain a good estimate of the standard deviation and the precision. In all of the results for the three transducers, the weighting function was small for small time shifts (20-50 ns) and reached a maximum at a time shift which was dependent on the measurement angle and the beam width. The time shift where the weighting function was maximum indicates the time shift where the most precise measurment can be made and the location of the minimum of the precision curve. At time shifts greater than the maximum of the weighting function, the weighting function again decreases as the correlation between echoes decreased. The weighting functions (part (a) of Figures 29, 30, and 31) were obtained from the same variance and average time shift values used to obtain the precision curves (part (b) of Figures 29, 30, and 31). Thus, the weighting functions are simply another way to show the change in the precision of the time domain correlation method versus the average time shift. Since the experimentally determined precision curves seem to agree with the precision relationships predicted by theory, the experimentally determined weighting functions should also agree with the weighting functions calculated from the theoretical precision relationships derived in section 3.2.

In summary, the experimental precision results presented in this section indicate that the precision of the time domain correlation method depends on the measurement angle, the transducer bandwidth and the transducer beamwidth. The precision relationships demonstrated by the experimental data indicate that the theoretical derivation of the precision of the time domain correlation method predicts the statistical properties of the time shift estimates remarkably well.

7.1.3 Quantization Performance

Since considerable hardware simplification and reduced cost can result by using fewer number of bits per sample, it is important to determine the effect of reducing the number of quantization levels. The original Sephadex^R data were sampled with eight bits of precision as were all of the echoes sampled by the UDAS. The experimental results which demonstrate the effect of sampling the received echo signals with less than eight bits of quantization are presented in this section.

Figure 32 shows the precision of one midstream axial flow measurement versus time shift and the number of bits used to represent the echo samples. All of the precision curves shown were obtained from one midstream axial flow velocity measurement at a measurement angle of 45^o. All 384 Kbytes of echo samples (6144 echoes, each 64 bytes) were then rounded to the nearest value which can be represented with a number of bits, B, less than eight. Since the numbers from the A/D converter are two's-complement numbers, the rounding process was not simply truncation. Truncation will result in a negative bias in the digital representation of the signal. If the number was positive, the lower (8-B) bits were set to one. If the number was negative, the lower (8-B) bits were set to zero. This rounding process results in a zero mean representation of the original signal for all values of B. The approximate signal-to-noise ratio of a signal represented by B bits is (6B + 4.8) dB if the analog signal was sampled within two standard deviations of the mean [43]. The electrical noise level in the original signal was approximately 20 dB below the signal level. Thus, the precision of the 6, 7, and 8 bit curves were all approximately equal (5-7%) and followed the same trend as the eight bit data. When the noise added due to quantization becomes significant (at about three bits of quantization), the precision jumps to 10-15% and is relatively constant for each time shift.

The effective signal-to-noise ratio was changed by the degree of received signal quantization. With eight bits of quantization the signal-to-noise ratio was approximately 20 dB. When the number of bits per sample was reduced to one (where only the sign of the signal was retained) the signal-to-noise ratio was approximately 10 dB. Thus the signal-to-noise ratio was reduced by 10 dB (or a factor of 3.16) which caused the precision value to increase to approximately 15% for one bit from 5% for eight bits. Thus, the precision value appears to be inversely related to the signal-to-noise ratio as predicted by equation (26) in section 3.2.

The precision value for 1-3 bits of quantization did not change very much with time shift because the quantization noise dominated the random variations of the time shift between echoes. Similar experiments under the same conditions, as the experiment which generated Figure 32, indicated that the precision curves for 1-3 bits of quantization did not have the same trends as shown in Figure 32 but have a similar magnitude (10-15%). This suggests that when random quantization noise dominates the received echoes, the precision of the time domain method is relatively constant for different time shifts. The precision relationship predicted by the theory presented in section 3.2 (equation (26)) is for a large signal-to-noise ratio and may not apply to the results shown in Figure 32. Future research should investigate the performance of the time domain correlation flow measurement method when low signal-to-noise ratios are present.

7.1.4 Precision Comparison With Doppler Flow Measurement

The precision results which were presented in section 7.1.2 for the time domain correlation method are compared with the precision of Doppler flow measurement methods in this section. The precision curves shown in Figures 29-31 indicate the precision of the time domain technique for different transducers and a signal-to-noise ratio of approximately 20 dB. The Doppler precision estimates obtained from literature values are listed in Table 1 and discussed in section 2.2. The signal-to-noise ratio for the best theoretical Doppler precision estimate (85%) was stated to be 10 dB [34] at a reported measurement angle of 45^o.

For comparison with the Doppler precision data, the time domain method data shown in Figure 30 must be corrected so that it represents a signal-to-noise ratio of 10 dB. According to the theoretical precision relationship of equation (24), the precision of the time domain correlation method is inversely proportional to the signal-to-noise ratio. The values shown in Figure 30 should all be multiplied by 3.16 (10 dB) since the time domain method measurements had a 20 dB signal-to-noise ratio. The values obtained can then be compared with the precision of Doppler flow measurement methods. The precision of the time domain technique, with transducer one at 45^o when the time shift between echoes was near 150 ns, was 5%. This precision was obtained by selecting a pulse repetition frequency (PRF) so that the flow rate caused a time shift between echoes of about 150 ns. At a 10 dB signal-to-noise ratio the precision of the time domain technique for this case would be 15.8%. Thus, for this example the precision of the time domain correlation experimental results (15.8%) was 5.4 times better than the precision of a comparable theoretical Doppler flow velocity measurement (85%).

A comparable experimental result listed in Table 1 for Doppler flow measurement indicates a precision of 124%. Thus, if Doppler experimental results are compared with time domain correlation experimental results, the precision of the time domain methods is 7.8 times better for a measurement angle of 45^o and a 5 MHz transducer.

7.2 VOLUME FLOW RESULTS

Detailed results and discussion of the volume flow measurement experiments are included in this section. The results of 31 volume flow measurement experiments are presented. Experiments were performed with three different scattering media: Sephadex^R and water; porcine blood; and glycerin. For convenience, these flow experiments will be referred to as Sephadex^R experiments, blood experiments, and glycerin experiments based on the type of scattering media used. The Sephadex^R experiments (discussed in sections 7.2.1, 7.2.2, and 7.2.3) demonstrated the accuracy of the volume flow measurement method for three different measurement angles. The blood experiments (discussed in section 7.2.4) verified that the time domain correlation flow measurement method worked with blood as a scattering media. The glycerin experiments (discussed in section 7.2.5), as well as the blood experiments, demonstrated the effects of refraction on the volume flow measurements since the speed of sound of these two scattering media are significantly different from the speed of sound in the surrounding media. Section 7.2.6 discusses the results of a method to quantify the effects of refraction on volume flow measurements by determining the sensitivity of simulated volume flow measurements.

7.2.1 Typical Volume Flow Measurement

The graphical and numerical results of three typical volume flow measurement experiments which were intended to demonstrate the volume flow measurement method are presented in this section. These three results demonstrate the feasibility of the volume flow measurement method at measurement angles of 45, 60, and 75^o. The numerical results of 26 Sephadex^R flow experiments are presented in the next two sections (sections 7.2.2 and 7.2.3) in order to demonstrate the accuracy of the volume flow measurement method under different experimental conditions.

Figure 33 shows a typical result of 11 one dimensional axial flow velocity versus range measurements combined to form constant velocity ellipses as detailed in section 6.2. Dialysis tubing with a diameter of approximately 6.4 mm and a track setting (Θ) of 45° was used for this Sephadex^R experiment. These data were obtained from the fifth experiment on September 9, 1985. The data set filename used to reference all experimental data sets is formed from the date of the experiment and the experiment number, SEP095 in this case.

As indicated in section 6.2, the volume flow was estimated by two different methods. These methods are termed the TUBE SIZE and INTEGRATED flow estimates. Figure 33 indicates that the tube wall ellipse (the outer ellipse) has a minor axis length of approximately 6.4 mm and a major axis length of approximately 9.1 mm. The tube radius is therefore approximately 3.2 mm and the ratio of the minor axis to the major axis is 0.704. The measurement angle estimate from the tube wall ellipse alone is $\sin^{-1}(0.704)$ or 44.6°. The average measurement angle obtained from all of the ellipse values was 45.9° as shown in Figure 33 (see section 6.2 for definition of the average measurement angle). The TUBE SIZE flow estimate obtained from the tube radius, the maximum axial velocity, and the measurement angle was 157.1 mm/min for this data set. Since the hydrodynamic flow measurement was 152.9 ml/min, the error in this volume flow estimate was + 2.8%. This experiment indicated that the INTEGRATED volume flow, obtained by adding the flow contribution of each constant velocity ellipse, was 146.6 ml/min. The experimental error or accuracy, determined by comparison with the hydrodynamic flow rate, was -4.2%. Further discussion concerning the volume flow measurement accuracy can be found in the next section where many different flow measurement experiments are considered.

Figures 34 and 35 show the constant velocity ellipses for approximately the same hydrodynamic flow rate (149.7 ml/min and 146.9 ml/min, respectively) as was measured for Figure 33 (152.9 ml/min). The experimental data sets SEP102 (Figure 34) and SEP101 (Figure 35) were measured with a track setting (Θ) of 60 and 75°, respectively. The constant velocity ellipses for both data sets appear very similar in size because the axes of each plot were scaled independently. In both cases, the minor axis of the tube wall ellipse (the outer ellipse of each figure) is approximately 6.5 mm. This indicated that according to both measurements, the tube radius was approximately 3.25 mm. The length of the major axes of the two wall ellipses are considerably different. At 60° the tube wall major axis was estimated to be approximately 6.7 mm and at 75° approximately 6.6 mm. As indicated in section 6.2, the ratio of the minor axis to the major axis of all of the constant velocity ellipses was used to estimate the average measurement angle. For data set SEP102 the average measurement angle was 60.9° and for SEP101 it was 71.6°. As shown in Figures 34 and 35, the ultrasonic determined INTEGRATED volume flow estimates were 142.6 ml/min for SEP102 (-4.8% error) and 115.4 ml/min for SEP101 (-21.5% error). These values agree reasonably well with the hydrodynamic flow rate measurement (-21.5% error for SEP101 is due to the low measurement angle estimate). Complete numerical experimental results are presented in the next section.

7.2.2 Numerical Volume Flow Results

The numerical results from a series of volume flow experiments intended to demonstrate the accuracy of the volume flow measurement method are presented in this section. The ultrasonic data were analyzed in two separate ways to yield the TUBE SIZE and INTEGRATED volume flow estimates. These results were then compared to the hydrodynamically determined volume flow rate to assess their accuracy.

Table 8 is a summary of 26 Sephadex^R volume flow measurement experiments. The left six columns of Table 8 show the data set name, the track setting (Θ), the speed of sound of the surrounding medium (c_0), the speed of sound of the flowing fluid (c_1), the hydrodynamically determined volume flow rate, and the number of scan angles (number of one dimensional axial velocity profiles). The next three columns show ultrasonically obtained results from the constant velocity ellipses, that is, the measurement angle estimate (Θ_M), the tube cross sectional area estimate and the maximum axial flow velocity estimate (V_{max}). The last four columns show the volume flow estimates for the two analysis procedures and their percent errors relative to the hydrodynamic flow rate. The TUBE SIZE volume flow rate (fourth column from the right) was estimated from the ultrasonically determined values of the tube area, the measurement angle and the

Table 8 - Ultrasonic Volume Flow Measurement Results for Sephadex^R.

Data Set Name	Track Setting (θ)	c_0 (mm/μs)	c_1 (mm/μs)	Hydro Flow Rate (ml/min)	Number of Angles	Angle Estimate (θ_M)	Tube Area (mm^2)	Max Axial Velocity (m/s)	TUBE SIZE Flow (ml/min)	TUBE SIZE Error (%)	INTEGRATED Flow (ml/min)	INTEGRATED Error (%)
JUL061	45	1.50	1.50	58.6	12	45.2	33.4	0.0395	56.2	-4.1	54.2	-7.6
SEP253	45	1.50	1.50	79.5	11	45.3	31.5	0.0559	75.0	-5.6	77.1	-2.9
JUL062	45	1.50	1.50	129.1	12	44.3	39.9	0.0874	146.1	13.2	127.3	-1.4
SEP095	45	1.50	1.50	152.9	11	45.2	37.3	0.0978	157.1	2.8	144.8	-5.3
SEP094	45	1.50	1.50	153.7	11	45.0	34.8	0.0983	145.4	-5.4	139.1	-9.5
JAN114	45	1.50	1.50	163.4	11	45.1	30.7	0.1014	149.5	-8.5	145.6	-10.9
JUN212	45	1.50	1.50	175.1	12	46.8	39.8	0.1092	190.6	8.9	175.5	0.2
JUL063	45	1.50	1.50	200.5	13	43.7	37.8	0.1250	196.0	-2.3	192.1	-4.2
JAN292	45	1.50	1.50	267.1	13	45.0	35.6	0.1647	248.4	-7.0	240.9	-9.8
JAN115	45	1.50	1.50	279.1	11	47.3	38.1	0.1670	281.6	0.9	276.1	-1.1
JAN116	45	1.50	1.50	401.0	12	45.2	31.8	0.2314	303.0	-24.4	349.6	-12.8
JAN117	45	1.50	1.50	550.7	13	45.9	32.2	0.2979	413.3	-24.9	520.6	-5.5
FEB052	60	1.50	1.50	97.0	11	62.2	38.8	0.0539	134.5	38.7	115.5	19.1
FEB061	60	1.50	1.50	120.0	11	59.2	37.0	0.0608	131.6	9.7	116.5	-2.9
SEP102	60	1.50	1.50	149.7	12	60.9	37.9	0.0661	164.1	9.6	142.6	-4.8
SEP096	60	1.50	1.50	150.7	11	58.7	36.8	0.0692	147.0	-2.5	131.4	-12.8
SEP097	60	1.50	1.50	150.9	11	59.5	33.2	0.0689	135.3	-10.4	134.8	-10.7
FEB051	60	1.50	1.50	167.7	13	63.0	39.3	0.0751	194.8	16.1	173.2	3.3
FEB111	60	1.50	1.50	214.3	13	62.5	35.7	0.0913	211.6	-1.3	195.3	-8.9
FEB053	60	1.50	1.50	331.0	13	59.7	35.4	0.1528	322.1	-2.7	340.9	3.0
FEB123	75	1.50	1.50	106.4	12	78.2	32.5	0.0261	124.3	16.9	122.1	14.8
SEP101	75	1.50	1.50	146.9	11	71.6	34.5	0.0379	124.2	-15.5	115.4	-21.5
JAN112	75	1.50	1.50	166.8	12	75.6	38.7	0.0379	176.3	5.7	158.8	-4.8
JAN113	75	1.50	1.50	168.8	12	73.6	33.1	0.0381	134.4	-20.4	154.1	-8.7
FEB121	75	1.50	1.50	220.5	12	77.3	34.3	0.0527	246.6	11.8	236.2	7.1
FEB122	75	1.50	1.50	334.6	11	73.8	34.7	0.0820	306.0	-8.5	295.2	-11.8

peak axial flow velocity. In this estimate the flow is assumed to be parabolic and axially symmetric. The INTEGRATED volume flow rate estimate (second column from right) is determined by integrating the constant velocity ellipses as described in section 6.2. The table also shows the experimental errors for both volume flow rate estimates when compared to the hydrodynamic flow rate.

Table 8 shows the results of Sephadex^R experiments which did not require refraction correction since the speed of sound of the Sephadex^R and distilled water mixture and distilled water alone were found to be nearly the same (see section 4.6.2). Each experiment at different flow rates and measurement angles was intended to illustrate a particular capability or limitation of the volume flow measurement method.

The first 12 entries in Table 8 all had a track setting of 45°. These data sets are ordered from the lowest hydrodynamically measured flow rate (58.6 ml/min for JUL061) to the highest flow rate (550.7 ml/min for JAN117). The number of scan angles for the 45° track setting experiments is 11, 12, or 13. Thirteen scan angles were used for three of the 12 experiments. In many of the experiments, it was difficult to center the dialysis tube such that all 13 scan angles resulted in reasonable (precision values less than 20%) axial flow velocity profiles. When the ultrasonic beam was close to tube wall most of the ultrasonic energy was reflected away and did not pass through the tube, resulting in very small signal-to-noise ratios and very large precision values. Thus, four of the experiments resulted in 12 scan angles with suitable data and five experiments resulted in 11 scan angles. Based on the accuracy of the volume flow estimates (to be considered in more detail in section 7.2.3), 11 scan angles appear to provide good definition of the two dimensional flow velocity profile. The measurement angle estimate (Θ_M) is accurate to within $\pm 2.5^{o}$ for all 12 experiments, if the measurement angle is equal to the track setting of 45^{o}. The tube area estimates obtained from the minor axis of the wall ellipse varied from 30.7 mm^2 to 39.9 mm^2. This relatively large variation was caused by the errors in the extrapolation of the axial velocity profiles used to locate the front and back walls. The maximum axial velocity (V_{max}) appears to be proportional to the volume flow rate and ranges from 0.0395 m/s for JUL061 to 0.2979 m/s for JAN117.

Except for data set JUL062, both volume flow estimates were within ± 10% of the hydrodynamic flow rate as long as the flow rate was less than approximately 300 ml/min. Above 300 ml/min (for data sets JAN116 and JAN117) the TUBE SIZE flow estimate gives a lower value than the INTEGRATED flow estimate. These experimental results demonstrate the effects of the change in the shape of the flow profile as the flow rate becomes larger. Above approximately 300 ml/min, the entrance length (see section 4.1.2) of the flow measurement system was insufficient for fully developed laminar flow. At these large flow rates, the flow profile became more constant near the center of the vessel as plug flow (constant across the vessel) was approached. This effect is illustrated in Figure 36 where the flow profile estimate for three different volume flow measurements (JAN114, JAN116, and JAN117) are superimposed. For these three measurements, the minor axis size of each of the ten constant velocity ellipses is plotted versus the normalized flow rate (normalized to a maximum flow velocity of one unit at the peak of each profile). The flow profiles shown in Figure 36 are assumed to be axially symmetric and the result of laminar flow. Measurements at higher flow rates (above 550 ml/min) have been attempted but have resulted in random variations in the axial velocity measurements presumably because of the presence of turbulent flow.

Since the relative axial flow velocity of the two higher flow rates (401 ml/min and 550 ml/min) shown in Figure 36 is greater than the assumed parabolic flow profile (shown in Figure 36 for JAN114), the TUBE SIZE volume flow estimate is considerably lower (24.9% lower for JAN117) than the hydrodynamically measured flow rate. The INTEGRATED flow estimate does not assume a parabolic flow profile and therefore gives a much better estimate (-5.5% error for JAN117) of the flow rate (see Table 8). Thus, if the flow is fully developed laminar flow, TUBE SIZE flow estimates may be sufficiently accurate to determine the volume flow; otherwise the INTEGRATED volume flow estimate should be used.

A track setting of 60^o was used for the next eight data sets listed in Table 8 with flow rates from 97.0 ml/min to 331.0 ml/min. A similar number of scan angles (11-13) were used for the eight 60^o track setting experiments as were used for the

45^{o} track setting experiments. The measurement angle estimates are within ± 3^{o} of the 60^{o} track setting and the tube area estimates (33.2-39.3 mm^{2}) agree with the values obtained at a 45^{o} measurement angle. For similar volume flow rates, the maximum axial velocity estimates are smaller for the 60^{o} experiments than for the 45^{o} track setting experiments as would be expected since the axial velocity decreases with increasing measurement angle. The TUBE SIZE volume flow estimates at 60^{o} have larger experimental errors than similar measurements at 45^{o} (38.7% error for FEB052). In all eight cases the INTEGRATED flow estimates are accurate to within 20% of the reference or hydrodynamic values.

The largest track setting used in the flow measurement experiments was 75^{o} for the last six data sets listed in Table 8. The hydrodynamic flow rate ranged from 106.4 ml/min for FEB123 to 334.6 ml/min for FEB122. Eleven or 12 scan angles were used for the six 75^{o} track setting experiments. The measurement angle estimates varied from 71.6^{o} to 78.2^{o} indicating substantially larger errors in the measurement angle at this track setting. The maximum axial velocity estimates for 75^{o} are less than half of the maximum axial velocity results at 45^{o} for similar hydrodynamic volume flow rates. This is consistent with the expected reduction in the axial velocity with measurement angle ($\cos(75^{o})/\cos(45^{o})=0.37$).

The larger volume flow measurement errors indicated for some of the 75° track setting experiments were partially caused by errors in the measurement angle estimates (Θ_M). A one degree error in a measurement angle estimate near 75° will cause a 6.5% error in the volume flow estimates. This can be compared with a 1.6% error in the flow estimates for a one degree error in a measurement angle of 45°. Furthermore, the precision of the axial velocity estimates at 75° is approximately three times greater than the precision of the axial velocity estimates at 45° which could result in less accurate volume flow estimates. Thus, more accurate volume flow measurements were obtained when the measurement angle was 45° or 60° than when it was 75°. This is shown in the next section where statistical analysis of the experimental data is considered. Other significant experimental errors (such as alignment problems with the circular track or problems with the elliptic fitting procedure) may also have contributed to the larger errors in the volume flow estimates at a 75° measurement angle.

7.2.3 Statistical Analysis Of Experimental Data

The experimental volume flow measurements and associated experimental errors described in the last section indicate that the volume flow measurement method provides remarkably accurate volume flow estimates under a wide range of experimental conditions. The purpose of the statistical analysis presented in this section is to determine the quantitative performance of each volume flow estimate from the experimental results. The volume flow estimates are assumed to be random samples of a measurement process which is linearly dependent on the actual volume flow rate. Also, the hydrodynamic measurement of the volume flow rate is assumed to have negligible error compared to the actual volume flow rate.

The relationship between the ultrasonic volume flow estimates and the hydrodynamic volume flow measurements were determined by simple linear regression. The linear prediction equation as well as the statistical variation for both volume flow estimates at the three measurement angles were determined from the experimental data.

In order to illustrate the accuracy of the flow estimates at a 45^{o} track setting, Figure 37 shows a plot of the ultrasonically determined flow estimates versus the hydrodynamically determined flow rate. The two flow estimates (TUBE SIZE and INTEGRATED) are plotted together for ease of comparison. The INTEGRATED and TUBE SIZE estimates are considerably different for the two experiments with the highest flow rates (JAN116 and JAN117). The other ten results indicate that the INTEGRATED and TUBE SIZE estimates were approximately the same (within 10% of each other in all cases). Thus, Figure 37 also shows the result of a least squares linear regression for the 22 flow estimates (12 INTEGRATED and 10 TUBE SIZE). The highest two TUBE SIZE estimates are not included in the regression because these two points are the result of a nonparabolic flow profile as indicated in Figure 36.

The linear regression line shown in Figure 37 indicates that the data follow a linear relationship rather well (correlation coefficient, r=0.994). The regression line can be described by the linear prediction equation, $y = y_o + m\ x$, where y is the ultrasonically determined volume flow rate (TUBE SIZE or INTEGRATED) and x is the hydrodynamic volume flow measurement for each experiment. The slope of the regression line, m, and the y intercept of the regression line, y_o, were both determined by simple linear regression [45] from the experimental data. The linear regression indicated that the intercept value (y_o) was 7 ± 11 ml/min and the slope (m) was 0.92 ± 0.05 where the intervals are 95% confidence intervals for the 22 data points [45]. Independent statistical analyses of the experimental data for the two ultrasonic flow estimates at all three track settings are considered in this section.

A linear regression similar to the one illustrated in Figure 37 for the 45^o flow experiments was used to estimate the bias, accuracy, and variance of the flow estimates [45] at different measurement angles. Since the TUBE SIZE flow estimate may have a different bias than the INTEGRATED flow estimate, the two flow estimates were analysed separately. A single regression line for both estimates is shown in Figure 37 for illustration purposes and because it was found that both estimates had nearly the same slope and intercept. The bias of the flow estimate is indicated by the intercept estimate (y_o). If the intercept estimate confidence limit contains zero, then the experimental evidence suggests that the accuracy of the flow estimate does not depend on the magnitude of the flow being measured (a zero flow rate would produce a flow estimate within the intercept confidence limit 95% of the time). If, in addition, the slope estimate (m) confidence limit includes unity, the experimental evidence suggests that the volume flow estimate is as accurate as the hydrodynamically determined flow rate. If the slope confidence limit does not include unity, then the flow estimate is very likely (95% of the time) to be biased.

Thus, a statistical method identical to the method used to analyse the mill base experimental data in section 4.6.1 was used to determine the accuracy of the volume flow experimental data for each measurement angle. Table 9 shows the results of six linear regressions from the Sephadex^R experimental data shown in Table 8. The results shown are for both flow estimates (TUBE SIZE and INTEGRATED) at the three different track settings.

Table 9 - Statistical Analysis Data From Sephadex^R Flow Experiments at Three Different Track Settings.

Track Setting (Θ)	Number of Trials	Mean Squared Error (s)	Correlation Coefficient (r)	Intercept Estimate (y_o)	Slope Estimate (m)
INTEGRATED flow estimates:					
45	10	8.2	0.993	-0.2 ± 16	0.95 ± 0.09
60	8	15.3	0.982	4 ± 14	1.01 ± 0.20
75	6	18.5	0.970	23 ± 59	0.83 ± 0.29
TUBE SIZE flow estimates:					
45	10	11.9	0.987	4 ± 23	0.97 ± 0.13
60	8	16.8	0.970	31 ± 40	0.86 ± 0.22
75	6	24.8	0.951	27 ± 79	0.86 ± 0.39

The statistical data shown in Table 9 summarize the experimental data shown in Table 8. The correlation coefficient values are all very close to unity (lowest 0.951) indicating that a very linear relationship exists between the ultrasonic flow estimates and the hydrodynamic flow measurement. The slope estimates (m) seem to indicate that both ultrasonic flow estimates may be somewhat lower than the hydrodynamic flow rate. For example, at $\theta = 45^\circ$, $m = 0.95 \pm 0.09$ indicates that a small systematic error in the volume flow estimate may exist (although the confidence limit includes unity). This negative bias is also suggested by the large number of negative experimental errors in Table 8 and may be caused by a small index of refraction present in the aqueous suspension of Sephadex^R. Measurements of the speed of sound in the Sephadex^R and water mixture indicated that the refractive index was between 0.99 and 1.01 (with 95% confidence since each measurement was accurate to within ± 0.5%). The refraction simulation results presented in section 6.6 suggest that a 1% change in the speed of sound in the flowing fluid could cause approximately a 6% change in the volume flow estimate at 45°. This could easily explain the slight negative bias indicated by the slope estimates at 45° since the speed of sound in the aqueous suspension of Sephadex^R is likely to be higher than the speed of sound of water alone because the addition of a solid to water almost always results in a higher speed of sound [44]. Experimental refraction results are considered in detail in sections 7.2.5 and 7.2.6.

The mean squared error (s) obtained from the linear regression indicates the standard deviation of the experimental data about the regression line [45] and can be used to show the relative repeatability of the experiments. Also, both confidence limits are proportional to the mean squared error and therefore indicate the repeatability or precision of the experimental data. The mean squared error values shown in Table 9 indicate that for all three measurement angles, the TUBE SIZE flow estimates are less repeatable than the INTEGRATED flow estimates. This suggests that the TUBE SIZE estimate may be less precise than the INTEGRATED flow estimate.

The mean squared error values also indicate that for both flow estimates, experiments with higher measurement angles are less repeatable. This causes the confidence limits to be much larger for the larger measurement angles than at 45°. Many more experiments would be required in order to determine the slope and intercept values more accurately. The present experimental system requires manual adjustment of the scan angle which results in tedious and time consuming experiments. Data could be collected automatically with the addition of a computer controlled scan angle positioning system. Future research may benefit from such a positioning system.

The correlation coefficient (r) indicates how well the experimental data fit a straight line. The correlation coefficient is also a measure of the repeatability or precision of a volume flow estimate. The closer the correlation coefficient is to unity, the more precise the volume flow estimate and the closer the regression line is to the volume flow estimates. The correlation coefficients shown in Table 9 indicate that both volume flow estimates follow a very linear relationship (the lowest r value is 0.951) and that the INTEGRATED estimates are somewhat better than the TUBE SIZE estimates for all track settings. The correlation coefficients for both estimates decrease with increasing measurement angle indicating that less precise volume flow estimates are possible at higher measurement angles.

Thus, the statistical analysis of the 24 volume flow experiments at three different track settings shows that the precision of both volume flow estimates gets worse with increasing measurement angle. The precision of the axial flow velocity estimates gets worse with increasing measurement angle (as shown experimentally in section 7.1.2 and theoretically in section 3.2) and causes the volume flow estimates to become less precise.

7.2.4 Volume Flow Results With Fewer Scan Angles

All of the preceding volume flow measurement results had 11, 12, or 13 scan angles. This number of scan angles produced rather accurate INTEGRATED as well as TUBE SIZE volume flow estimates. Fewer scan angles would result in a shorter time to complete each experiment (each scan angle took 90 seconds) and a shorter analysis time since less data are manipulated. It is, therefore, important to determine the effect of the number of scan angles on the accuracy of the volume flow estimate.

In order to simplify the analysis, the previous volume flow estimates (shown in Table 8) are compared to estimates obtained with half the number of scan angles. For each of the 26 Sephadex^{R} volume flow experiments listed in Table 8, half of the scan angles were removed from the data set and the same analysis program was used to determine both volume flow estimates (INTEGRATED and TUBE SIZE). In each data set, the odd numbered scan angles (first, third, fifth and so on) were kept and the even numbered scan angles were deleted. Thus, 11 or 12 scan angle data sets are reduced to six scan angle data sets and 13 scan angle data sets are reduced to seven scan angle data sets. Table 10 shows the volume flow estimates for the same experimental data sets as shown in Table 8 but with the even scan angles removed. All of the ultrasonically determined quantities were recalculated from the reduced data set. The data set name (with an 'H' appended to each), track setting, number of scan angles remaining, and the measured data for each data set are shown in Table 10 in an identical format as was used in Table 8.

Comparison of the results shown in Table 10 to those shown in Table 8 indicates that using half of the scan angles changes the flow estimate significantly when compared with the volume flow estimates with 11 or greater scan angles. The magnitude of the errors also seems to increase with increasing measurement angle (as large as a -37% error for 75^{o}). Thus, the greater precision values at higher measurement angles leads to greater variation of the volume flow estimates when fewer scan angles are used. The same statistical analysis done in the last section for

Table 10 - Ultrasonic Volume Flow Measurement Results for Sephadex^R With Half of the Scan Angles Removed From the Original Data Set.

Data Set Name	Track Setting (Θ)	c_0 (mm/μs)	c_1 (mm/μs)	Hydro Flow Rate (ml/min)	Number of Angles	Angle Estimate (Θ_M)	Tube Area (mm^2)	Max Axial Velocity (m/s)	TUBE SIZE		INTEGRATED	
									Flow (ml/min)	Error (%)	Flow (ml/min)	Error (%)
JUL061H	45	1.50	1.50	58.6	6	44.9	32.8	0.0395	55.0	-6.2	53.9	-8.1
SEP253H	45	1.50	1.50	79.5	6	45.1	30.7	0.0553	72.1	-9.2	76.7	-3.5
JUL062H	45	1.50	1.50	129.1	6	45.6	41.3	0.0874	154.8	19.9	136.1	5.5
SEP095H	45	1.50	1.50	152.9	6	45.4	36.9	0.0976	154.0	0.7	142.3	-6.9
SEP094H	45	1.50	1.50	153.7	6	45.0	34.5	0.0977	143.0	-7.0	136.0	-11.5
JAN114H	45	1.50	1.50	163.4	6	46.0	37.7	0.1014	165.0	1.0	152.5	-6.7
JUN212H	45	1.50	1.50	175.1	6	47.1	38.2	0.1065	179.3	2.4	174.3	-0.5
JUL063H	45	1.50	1.50	200.5	7	44.0	39.2	0.1248	203.9	1.7	204.3	1.9
JAN292H	45	1.50	1.50	267.1	7	44.2	35.5	0.1618	240.2	-10.1	219.2	-17.9
JAN115H	45	1.50	1.50	279.1	6	45.3	39.9	0.1670	284.4	1.9	245.3	-12.1
JAN116H	45	1.50	1.50	401.0	6	41.3	30.5	0.2314	281.6	-29.8	392.0	-2.3
JAN117H	45	1.50	1.50	550.7	7	45.0	31.2	0.2979	393.6	-28.5	456.0	-17.2
FEB052H	60	1.50	1.50	97.0	6	61.8	36.3	0.0539	124.5	28.3	110.9	14.4
FEB061H	60	1.50	1.50	120.0	6	58.1	35.7	0.0602	122.4	2.0	112.4	-6.3
SEP102H	60	1.50	1.50	149.7	6	60.0	35.1	0.0661	139.4	-6.9	135.5	-9.5
SEP096H	60	1.50	1.50	150.7	6	59.6	38.2	0.0691	156.6	3.9	157.8	4.7
SEP097H	60	1.50	1.50	150.9	6	58.7	33.6	0.0685	133.2	-11.7	126.3	-16.3
FEB051H	60	1.50	1.50	167.7	7	59.5	37.3	0.0751	165.6	-1.3	149.5	-10.8
FEB111H	60	1.50	1.50	214.3	7	59.7	34.5	0.0897	184.2	-14.0	169.6	-20.8
FEB053H	60	1.50	1.50	331.0	7	62.3	36.1	0.1528	355.7	7.5	373.2	12.7
FEB123H	75	1.50	1.50	106.4	6	68.6	32.6	0.0261	70.0	-34.2	67.1	-36.9
SEP101H	75	1.50	1.50	146.9	6	73.6	38.8	0.0374	154.1	4.9	135.3	-7.9
JAN112H	75	1.50	1.50	166.8	6	69.9	41.5	0.0376	136.3	-18.3	115.7	-30.6
JAN113H	75	1.50	1.50	168.8	6	72.0	33.3	0.0375	121.5	-28.0	121.3	-28.2
FEB121H	75	1.50	1.50	220.5	6	73.4	34.1	0.0520	186.1	-15.6	180.9	-18.0
FEB122H	75	1.50	1.50	334.6	6	69.1	34.8	0.0820	239.1	-28.5	211.6	-36.8

the data shown in Table 8 was also done using the data shown in Table 10 when half of the scan angles are removed. The resulting statistical values are shown in Table 11 in the same format as was used in Table 9.

Table 11 - Statistical Analysis Data From Sephadex^R Flow Experiments at Three Different Track Settings With Half of the Scan Angles Removed.

Track Setting (θ)	Number of Trials	Mean Squared Error (s)	Correlation Coefficient (r)	Intercept Estimate (y_o)	Slope Estimate (m)
INTEGRATED flow estimates:					
45	10	13.1	0.979	17 ± 25	0.83 ± 0.14
60	8	26.7	0.958	-29 ± 63	1.13 ± 0.34
75	6	21.4	0.927	25 ± 68	0.60 ± 0.34
TUBE SIZE flow estimates:					
45	10	13.9	0.982	6 ± 27	0.96 ± 0.15
60	8	21.3	0.967	-4 ± 50	1.04 ± 0.28
75	6	23.3	0.933	22 ± 74	0.68 ± 0.37

Comparing Table 11 to Table 9 reveals that the mean squared error values are larger in five of the six cases resulting in larger confidence intervals for the slope and intercept estimates. The correlation coefficients are lower in all cases but still indicate a very linear relationship between the ultrasonic flow estimates and the hydrodynamic values. Also, in Table 11 all three correlation coefficients for the INTEGRATED volume flow estimate are almost identical (within 0.009) to the correlation coefficients for the TUBE SIZE volume flow estimates suggesting that the two volume flow estimates give about the same results when only six or seven scan angles are used. The slope values are lower in four of the six cases indicating a negative bias, especially at higher measurement angles (m = 0.60 ± 0.34

for the INTEGRATED estimate at 75°). This negative bias may be caused by the fact that less data are used in the elliptic fitting procedure resulting in inaccurate estimates of the dimensions of the ellipses.

Much of the problem with less than 11 scan angles can be traced to problems with the elliptic fitting procedure. For example, the smaller constant velocity ellipses near the center of the vessel have less than five constant velocity points resulting in a nonunique and possibly incorrect elliptic fit. When less than five constant velocity points are present in a particular velocity level, the parameters determined by the elliptic fitting procedure are not used in the volume flow or measurement angle estimates. This potentially makes the volume flow estimate more subject to error, since fewer velocity levels are used to obtain the volume flow result. More sophisticated algorithms to estimate the volume flow from less than seven scan angles are required. Future research could be directed in this area.

In summary, reducing the number of scan angles by half such that six or seven scan angles remain causes the precision and accuracy of the volume flow estimates to be reduced. However, the precision and accuracy of the volume flow estimates obtained with only six scan angles suggests that six scan angles may be sufficient in many applications.

7.2.5 Volume Flow Measurement Of Blood

In order to verify that the time domain correlation volume flow measurement method works with blood as a scattering fluid, the flow of fresh citrated porcine blood was measured. The method used to collect the porcine blood is described in section 4.6.2. Figure 38 shows the constant velocity ellipses and a volume flow estimate of the flow of porcine blood at a measurement angle of 60^o without refraction correction. The data shown graphically in Figure 38 are listed in Table 12 as data set JUL167. The data sets shown in Table 12 are from porcine blood flow experiments (JUL163 and JUL167) and glycerin experiments (JUL035, OCT021, and OCT041), both with and without refraction correction. Glycerin experiments will be considered separately in section 7.2.6. Since blood and glycerin have significantly different speed of sound values than the surrounding medium, refraction causes a large change in the volume flow estimates. In order to illustrate this effect experimentally, results with and without refraction correction have been presented in Table 12. The refraction correction procedure is outlined in section 6.4.2.

The speed of sound of the porcine blood was measured to be 1.55 mm/μs at 25^oC (see section 4.6.2). The surrounding medium was normal saline since dialysis tubing is a semi-permeable membrane and could cause the small ions in the blood to diffuse across the membrane. Since normal saline has the same osmolarity

Table 12 - Ultrasonic Volume Flow Measurement Results for Blood and Glycerin.

									TUBE SIZE		INTEGRATED	
Data Set Name	Track Setting (θ)	c_0 (mm/μs)	c_1 (mm/μs)	Hydro Flow Rate (ml/min)	Number of Angles	Angle Estimate (θ_M)	Tube Area (mm^2)	Max Axial Velocity (m/s)	Flow (ml/min)	Error (%)	Flow (ml/min)	Error (%)
Blood experiments without refraction correction:												
JUL167	60	1.51	1.51	109.5	14	60.6	30.6	0.0454	85.9	-21.5	88.8	-18.9
JUL163	60	1.51	1.51	157.6	13	64.2	29.6	0.0659	134.5	-14.7	136.7	-13.3
Blood experiments with refraction correction:												
JUL167	60	1.51	1.55	109.5	14	62.3	33.4	0.0466	100.2	-8.5	103.6	-5.4
JUL163	60	1.51	1.55	157.6	13	65.8	32.3	0.0677	159.5	1.2	160.7	2.0
Glycerin experiments without refraction correction:												
JUL035	45	1.50	1.50	87.3	9	28.9	24.8	0.0526	44.7	-48.8	36.3	-58.4
OCT021	45	1.50	1.50	88.0	8	31.4	19.9	0.0557	38.9	-55.8	38.8	-56.0
OCT041	60	1.50	1.50	209.2	10	50.9	34.8	0.1036	171.5	-18.1	136.2	-34.9
Glycerin experiments with refraction correction:												
JUL035	45	1.50	1.70	87.3	9	35.8	44.9	0.0596	98.8	13.2	82.5	-5.5
OCT021	45	1.50	1.70	88.0	8	38.2	38.3	0.0631	92.2	4.8	88.1	0.1
OCT041	60	1.50	1.70	209.2	10	54.0	47.9	0.1174	287.1	37.2	228.8	9.3

as blood, no net diffusion of the ions will take place. Unlike Sephadex^R flow measurements, the blood flow measurements are affected by refraction. Since the speed of sound in saline is 1.51 mm/μs and the speed of sound in porcine blood is 1.55 mm/μs, a 1.0265 refractive index is present. This small refractive index is responsible for the large negative experimental error in the blood flow measurements (-18.9% for JUL167). Not only does the higher speed of sound in the medium make the velocity estimates lower, but the tube size and measurement angle are also reduced. Thus, a one percent change in the speed of sound of the flowing fluid is likely to make a greater than one percent change in the volume flow estimate. This effect has been demonstrated by simulation as described in section 7.2.7. As shown in Table 12, refraction corrected results for the two blood flow data sets have much lower experimental errors (less than 6%).

7.2.6 Volume Flow Measurement Of Glycerin

A mixture of glycerin, distilled water, and Sephadex^R was used to demonstrate a more severe volume flow estimate error due to refraction. Also, the refraction correction method described in section 6.4.2 will be tested for this larger index of refraction. As indicated in section 4.6.2, the 50% glycerin-water mixture had a measured speed of sound of 1.70 mm/μs at 25°C. The surrounding medium was distilled water with a speed of sound of 1.50 mm/μs. The refractive index in this case was 1.133. This large index of refraction caused a large negative bias when a constant 1.5 mm/μs speed of sound was assumed (-56.0% for data set OCT021 shown in Table 11). Figure 39 shows the constant velocity ellipses and volume flow results for the OCT021 data set after refraction correction. The additional solid lines represent the path of the beam if no refraction effects were present. Table 11 also shows a summary of the refraction corrected 50% glycerin-water mixture results. Considerable improvement in the error of the volume flow estimates is indicated. Data set OCT041 was a glycerin flow experiment with a track setting of 60°. The volume flow estimate error (-34.9%) was less than the error for the two 45° cases (about -56% for JUL035 and OCT021). In all three cases the refraction corrected INTEGRATED volume flow results indicate a volume flow accuracy of better than 10%.

7.3 AXIAL FLOW VELOCITY RESULTS FOR PULSATILE FLOW

Since the flow of blood is pulsatile, it is important to determine if the time domain correlation technique can be used to measure flow variation with time. Since the UDAS is not capable of storing more than a few milliseconds of 1024 point echoes, one dimensional flow profiles with time can not be measured. Therefore, the pulsatile flow measurements presented in this section are restricted to flow versus time at a single point within the vessel.

Figure 40 shows the results of optimally weighting ten different pairs of echoes to obtain a velocity estimate for all 6143 echo pairs (each echo is 64 bytes) which can be stored in the UDAS. The flow in this case was steady (no time variation) laminar flow near the center of the tube where velocity gradients are small. All of the variation shown is small and is representative of the precision of the time domain correlation method. The optimum axial velocity estimate was determined as described in section 5.3. The optimum estimate of the speed of the scatterers at the center of the tube was determined by using the weighting funtion for the 5 MHz transducer at a measurement angle of 45° (shown in Figure 29).

A Masterflex peristaltic pump was used as a source of simple pulsatile flow. Measurements with an electromagnetic flow meter (Carolina Medical model 500) have shown that the Masterflex pump output is close to sinusoidal in shape with a positive average level. The average flow rate and pump pulse rate both vary with the pump speed. Figure 41 shows the optimum velocity estimate at the center of the dialysis tube with pulsatile laminar flow. The result is similar to what is observed at the output of the electromagnetic flow meter. The poor precision (> 10% for steady flow) of the electromagnetic flow meter prevented meaningful quantitative comparisons with the ultrasonic axial flow velocity measurements. Also, since it is difficult to position the single range cell at the center of the tube where the flow is maximum, no accurate volume flow estimates can be obtained.

7.3.1 Low Pass Filtered Pulse Flow Data

Since the axial flow velocity of pulsatile flow changes relatively slowly, the precision of pulsatile flow measurement can be improved by low pass filtering the optimum velocity estimate. A low pass digital filter was designed in order to eliminate some of the high frequency noise present in the pulse flow data shown in Figure 41. The resulting low pass filtered pulse flow data is a more precise representation of the pulsatile flow variation measured by the time domain correlation method. The filter was designed to pass the first ten harmonics (up to about 40 Hz) of the pulsatile flow variation without significant attenuation. Figure 42 shows the frequency response of a digital filter designed for this purpose using the McClellan-Parks algorithm [52]. Figure 43 shows the low pass filtered version of the same data presented in Figure 41. Since the pulse repetition rate was 6250 Hz, the -3 dB cutoff frequency of the filter was 47 Hz. Significantly less random variations in the filtered data are illustrated without reduction in the amplitude of the axial flow velocity variations (approximate mean pulse rate 4 Hz). Because the random variations of the axial flow velocity estimates have a wide bandwidth as illustrated by the rapid random variations of the pulsatile measurement of constant flow (see Figure 40), appropriate low pass filtering improves the precision of the flow versus time estimate. Future research should establish the accuracy of pulsatile flow measurements by using an accurate pulsatile flow generator or accurate pulsatile flow meters.

CHAPTER 8

CONCLUSIONS

A summary of the major accomplishments and results of this research is included in this chapter. Both simulation and experimental methods have been used to demonstrate some of the capabilities and limitations of a new time domain correlation method used to measure the volume flow of blood. Previously, pulsed Doppler flow measurement methods have been used for qualitative blood flow measurement. The quantitative limitations (namely accuracy and precision) of pulsed Doppler flow measurement were considered in Chapter 2 and are summarized in section 8.1.

A relatively new flow velocity measurement method, namely the time domain correlation method [12], was refined and developed in order to measure accurately the axial flow velocity profile in a round tube. A summary of the results of the axial flow velocity measurements is presented in section 8.2.

The new volume flow measurement method, developed as a result of this research, can be used to estimate the volume flow in a round tube without prior knowledge of the tube size, measurement angle, or flow velocity profile. The volume flow measurement method appears to be novel simply because the volume flow is determined exclusively from a collection of ultrasonic measurements. The major results of the volume flow measurement experiments are summarized in section 8.3.

The measurement of pulsatile flow by the time domain correlation method has not been tried previously. The results indicate that precise measurements of the pulsatile flow of human blood by the time domain correlation method may be possible. The results of measurements of the axial flow velocity of pulsatile flow are summarized in section 8.4.

In order to complete the experimental volume flow measurements, an extensive apparatus was designed and constructed. A flow regulation system provided constant laminar flow which could by measured ultrasonically. A transducer positioning system provided the capability to scan across a blood vessel phantom. An ultrasound data acquisition system (UDAS) was designed and constructed in order to easily sample and analyse the ultrasonic echoes. Improvements in the experimental aparatus, as discussed in section 8.6, may allow more accurate estimates of many ultrasonically determined parameters. Some of the basic practical limitations of the time domain correlation method (which can not be improved by equipment improvements) are summarized in section 8.5.

8.1 DOPPLER FLOW MEASUREMENT

The accuracy and precision of Doppler methods were examined by simulation and literature review and then compared to that of the time domain correlation method. The accuracy and precision of the time domain correlation method were found to be far superior.

The measurement of the axial flow velocity by pulsed Doppler methods is biased in an unpredictable way by the intervening tissue because the received mean frequency is changed by the frequency dependent attenuation of the tissue. This tissue bias is reduced as the bandwidth of the transmitted excitation is decreased. If narrow band, long excitations are transmitted, the range resolution is greatly reduced, making quantitative flow measurement difficult even with large vessels.

The standard deviation of Doppler flow measurements is extremely large and is proportional to the transmitted bandwidth. Thus, a long pulse must be transmitted in order to make the standard deviation of the velocity estimate reasonable. The raw Doppler flow estimate which is estimated for every echo has a standard deviation which often exceeds the mean, thus making the precision value greater than 100%. The poor precision of Doppler flow measurement makes quantitative measurements of blood flow extremely difficult.

8.2 ONE DIMENSIONAL TIME DOMAIN VELOCITY MEASUREMENT

The precision of the optimum time domain correlation method is 3-20% depending on the transducer used, the measurement angle, and the signal-to-noise ratio. The measurement precision of the flow estimate in one dimension along the beam axis has been improved such that the variance of the measurement is minimized for each range position. The precision of the flow estimate has been experimentally determined for different transducer apertures and different ultrasonic frequencies. The theoretical model of the precision of the time domain correlation technique appears to fit the experimentally determined precision curve adequately.

8.3 VOLUME FLOW MEASUREMENT

A series of one dimensional axial flow velocity estimates were used to determine the volume flow through a round vessel by using the volume flow measurement method developed as a result of this research. The experimental error of the volume flow estimate increased with increasing measurement angle, but experimental errors less than 15% were obtained consistently at measurement angles of 45^o and 60^o.

The volume flow of blood in a round tube was measured by scanning the vessel and fitting an ellipse to the constant velocity points. A large number of scan angles provided the best estimate of the volume flow (especially at large measurement angles). Fewer than seven scan angles resulted in larger experimental errors.

The effect of refraction on the ultrasonic beam can cause large errors in the volume flow estimate. The small refractive index from normal saline to porcine blood (1.0265) resulted in greater than 15% error in the volume flow estimate. The effects of refraction can be corrected by knowing the speed of sound in the surrounding medium and the speed of sound in the flowing fluid. Refraction correction by the iterative procedure suggested in this work provided accurate volume flow estimates (within 10%) for experimental measurements of blood flow and the flow of a glycerin-water mixture.

8.4 PULSATILE FLOW MEASUREMENT

The feasibility of the measurement of pulsatile flow by time domain correlation has been demonstrated by measuring the midstream velocity of the output of a peristolic pump. The precision of this estimate can be improved by lowpass filtering the flow versus time estimates.

8.5 PRACTICAL LIMITATIONS

Much of the ultrasound energy hitting the tube wall is reflected away from the transducer. When the measurement angle is small or when the beam hits the tube far from the tube center, considerably less signal is received. This causes the precision of the flow measurement to decrease due to a reduced signal-to-noise ratio. Velocity gradients within the ultrasonic beam cause large increases in the standard deviation of the flow velocity estimate resulting in imprecise flow measurements near the vessel walls. Also, the beam is refracted when it passes into the tube if the flowing liquid has a different speed of sound than the surrounding medium. The refraction of the ultrasonic beam causes the tube size and the measurement angle to be incorrectly estimated and therefore causes large experimental errors in the volume flow measurement. The refraction effects can be corrected if the speed of sound of the flowing fluid is known, and the front wall positions can be accurately determined from the flow measurements.

8.6 FUTURE WORK

During this research, several areas of potential future research were identified. Some of the more important areas to be investigated are as follows:

(1) A theoretical analysis of the quantitative effects of flow velocity gradients on the axial flow velocity estimates may show important limitations on the accuracy and precision of the time domain correlation method.

(2) Measurements of the flow velocity profile in a tube which has a sharp bend, an irregular shape, or a bifurcation (two branches) may demonstrate the versatility of the volume flow measurement method.

(3) Real time flow measurement hardware using the time domain correlation method would allow a tremendous number of fundamental flow measurement experiments to be performed.

(4) A volume flow measurement method which can accurately estimate the measurement angle and tube size from less than six scan angles may be useful in some clinical applications.

(5) The addition of an accurate computer controlled scan angle positioning system could improve the experimental volume flow measurement system so that flow measurement experiments could be performed rapidly without operator intervention.

(6) The measurement of pulsatile flow by the time domain correlation method may demonstrate that the measurement of human blood flow in a quantitative way is possible. Experiments should be designed which establish the accuracy and precision of the measurement of pulsatile flow by time domain correlation.

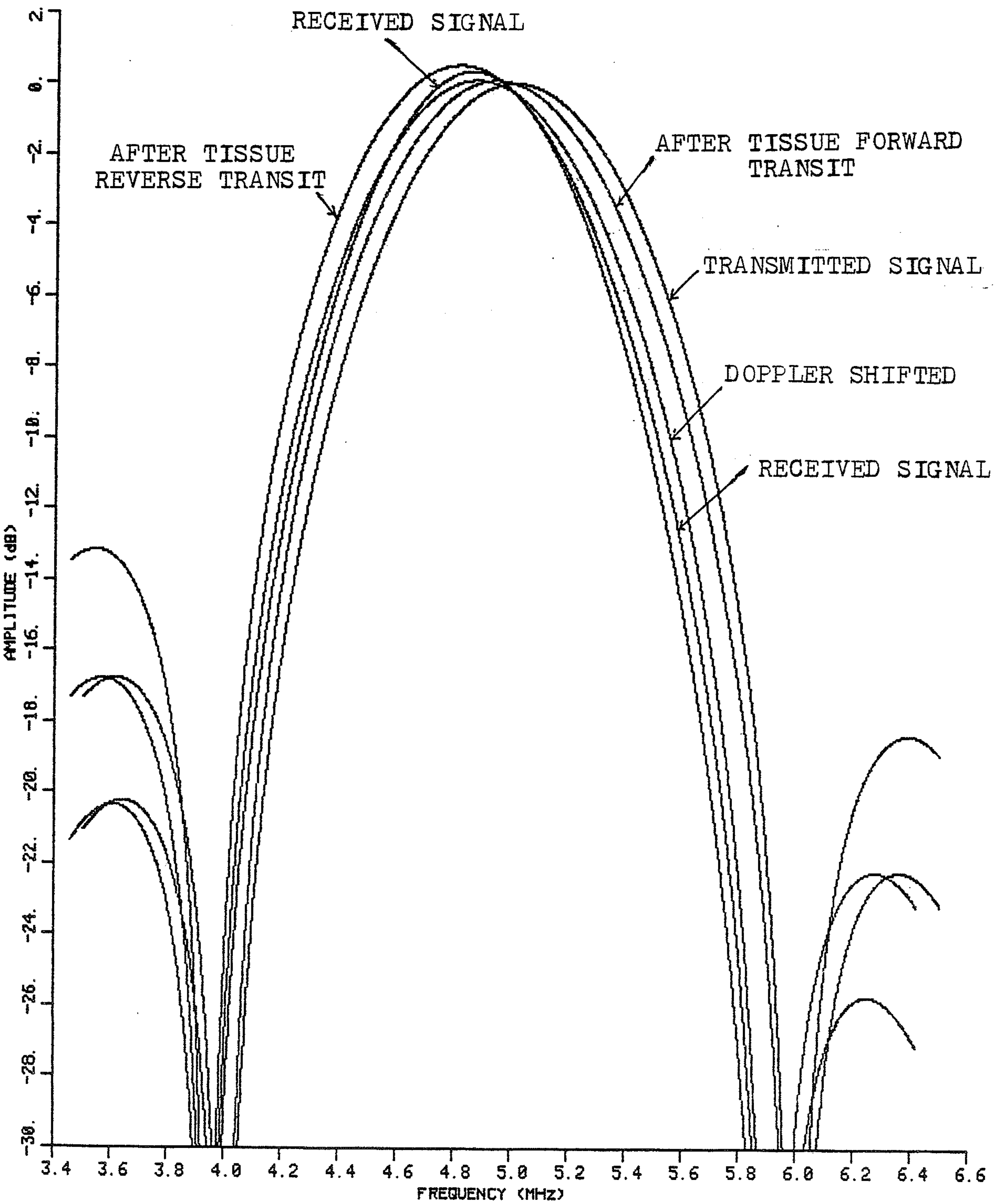

Figure 1 - Simulation results of typical signal spectra at various positions in the evolution of the acoustic signal. The center frequency of the transmitted signal and transducer is 5 MHz. The transducer Q is 3 and the target is moving at a constant 10 m/s toward the transducer. For this example, the values used in equation (3) are $A_o = 1.0$ and $b = 1.4$.

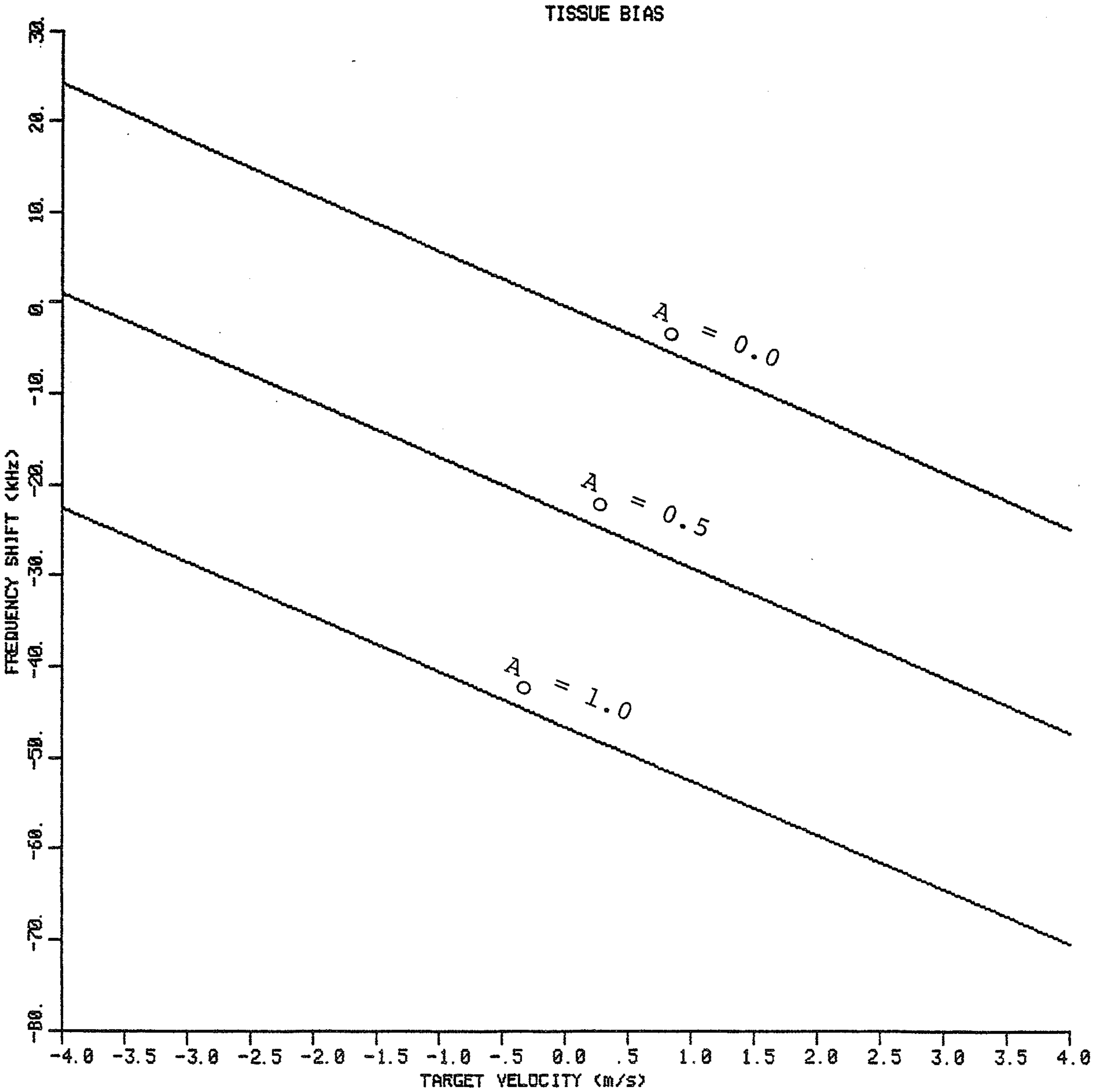

Figure 2 - Simulation results of the mean frequency shift of the received echo signal versus target velocity for different A_o values with b = 1.4. A ten cycle excitation is simulated. A linear relationship between the mean frequency shift and the target velocity is indicated. The negative bias changes with A_o and b (see equation (3) for definition of A_o and b).

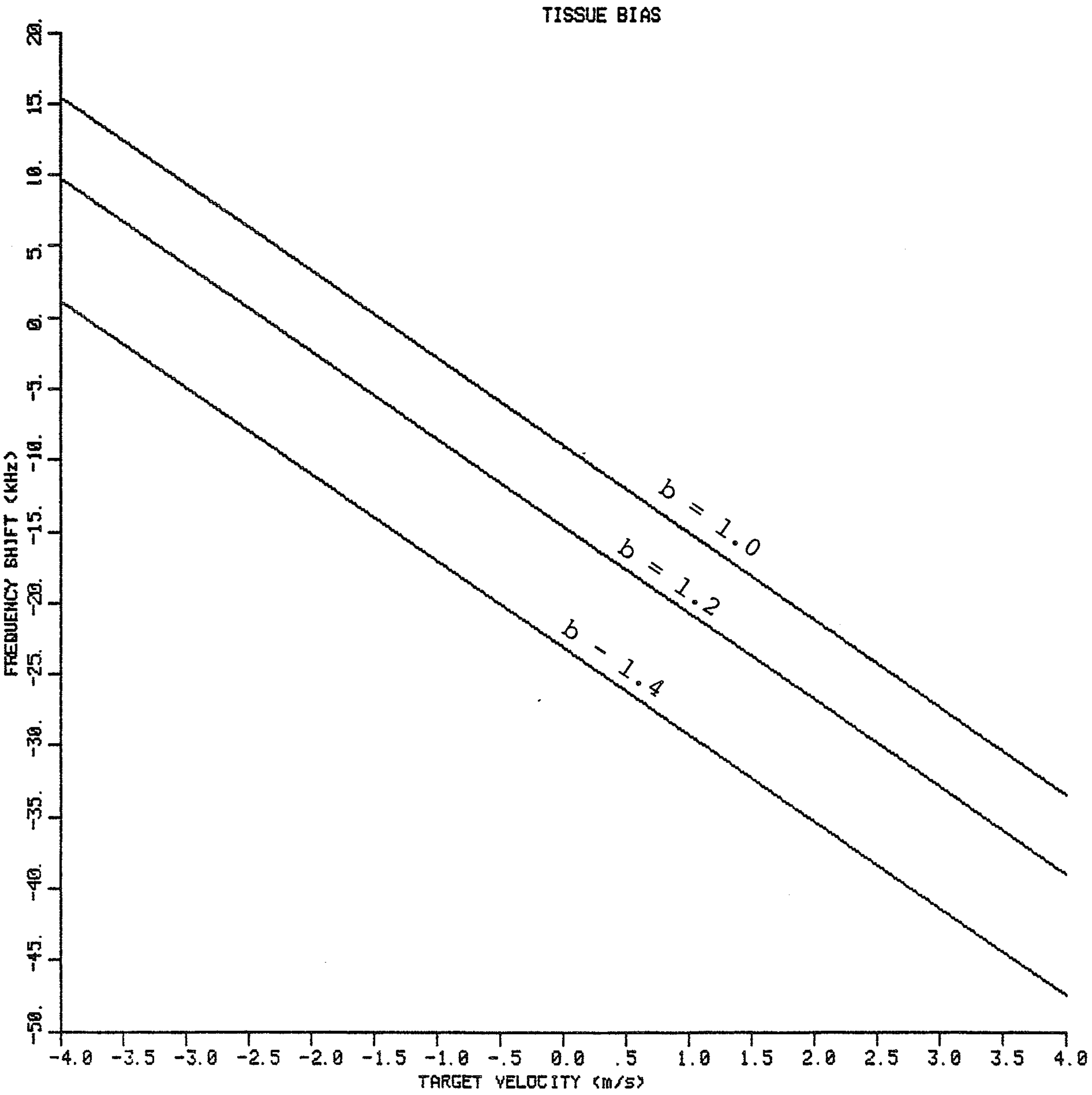

Figure 3 - Simulation results of the mean frequency shift of the received echo signal for different b values (A_o = 0.5, 10 cycles transmitted). The negative bias gets worse with increasing b (see equation (3) for definition of A_o and b).

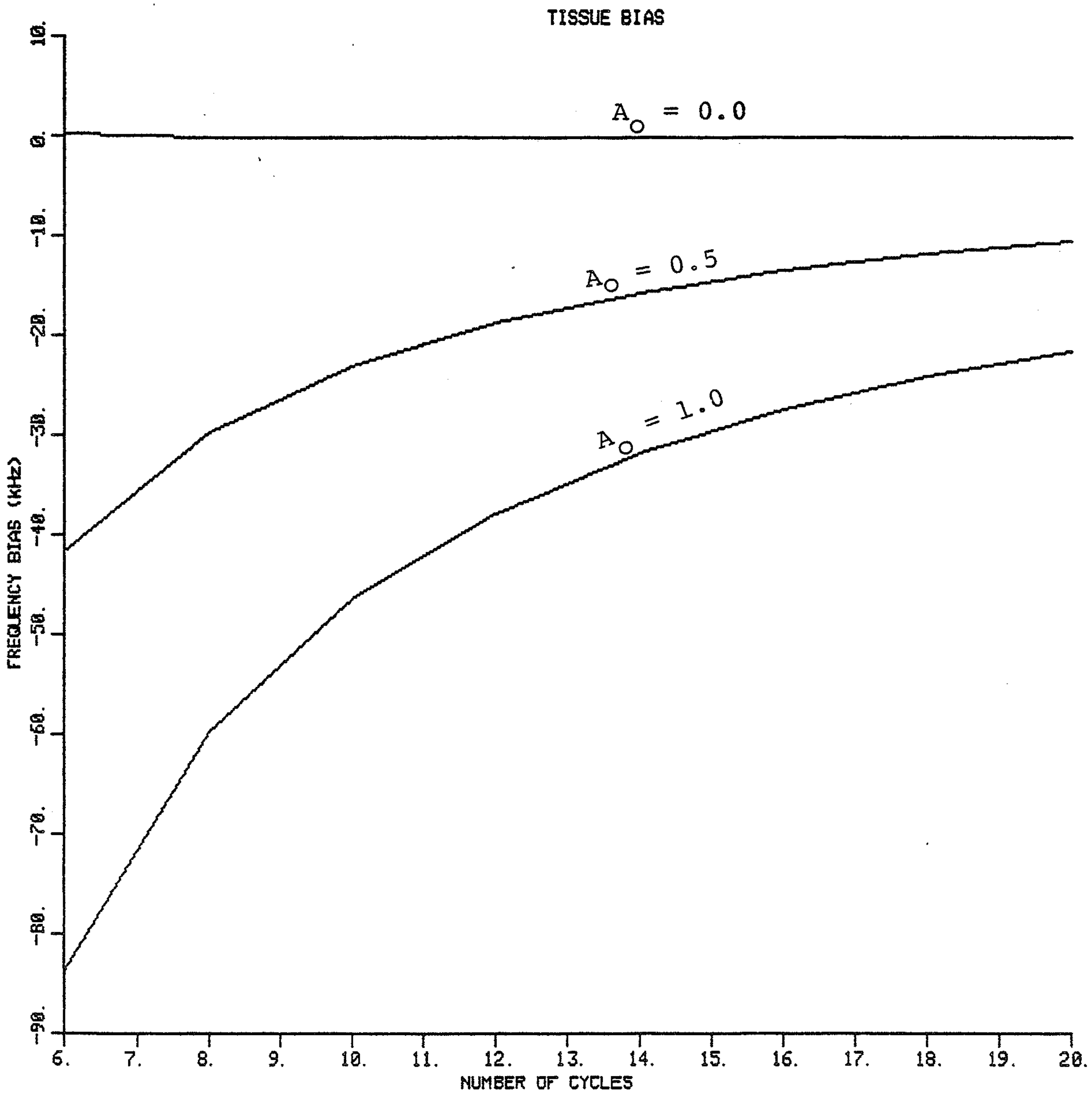

Figure 4 - Simulation results of the mean Doppler frequency bias of the received echo signal versus number of cycles transmitted for b = 1.4 and A_o = 0.0, 0.5, 1.0 (see equation (3) for definition of A_o and b).

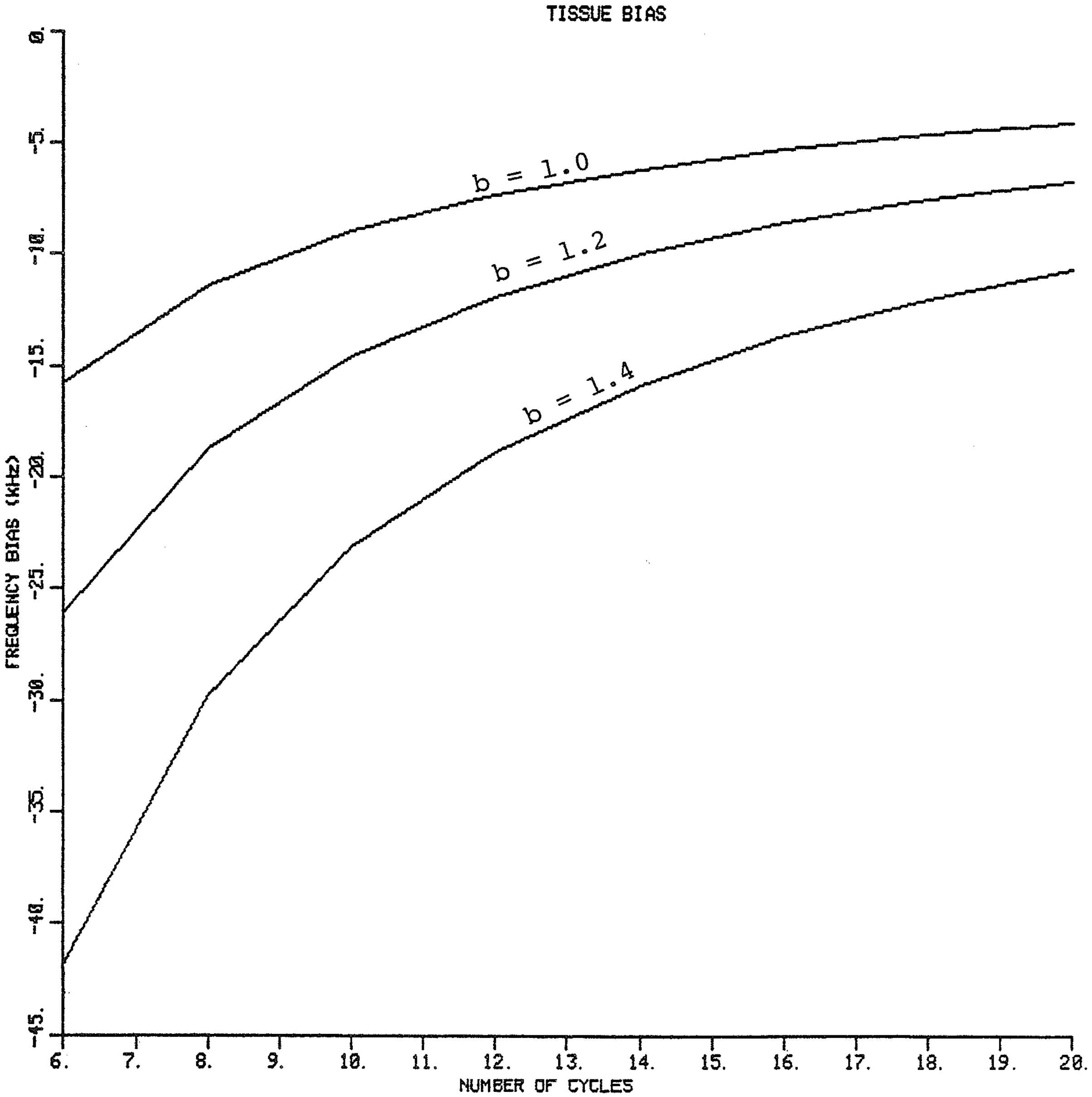

Figure 5 - Simulation results of the mean Doppler frequency bias of the received echo signal versus number of cycles transmitted for A_o = 0.5 and b = 1.0, 1.2, 1.4 (see equation (3) for definition of A_o and b).

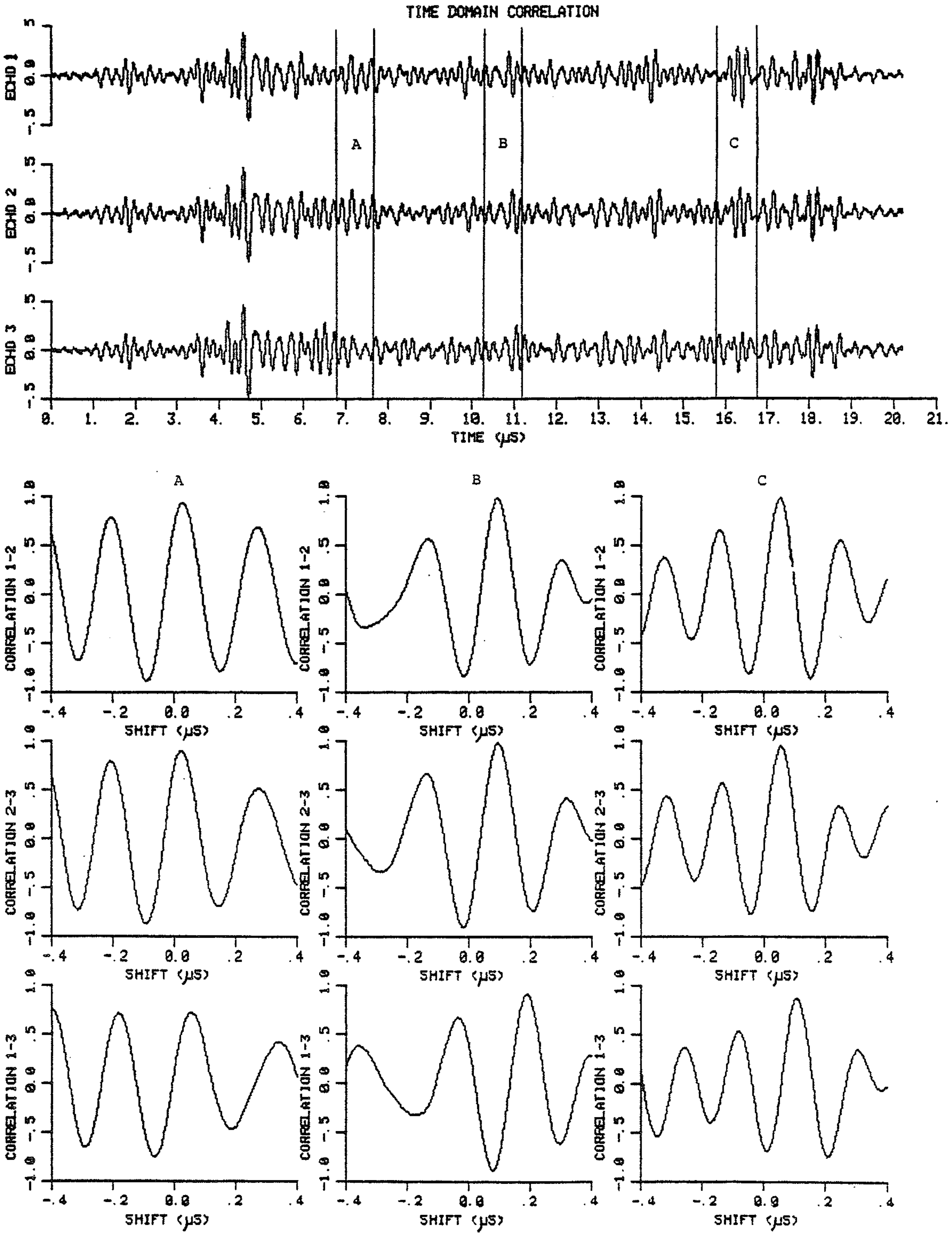

Figure 6 - Time domain correlation method example for typical experimental data for $\Theta = 45^{\circ}$. The upper three plots show three consecutive echoes sampled by the UDAS at a 50 MHz sampling rate with T = 384 µs. The lower nine plots show the correlation coefficients versus shift for the three 0.8 µs range gates (A, B, and C).

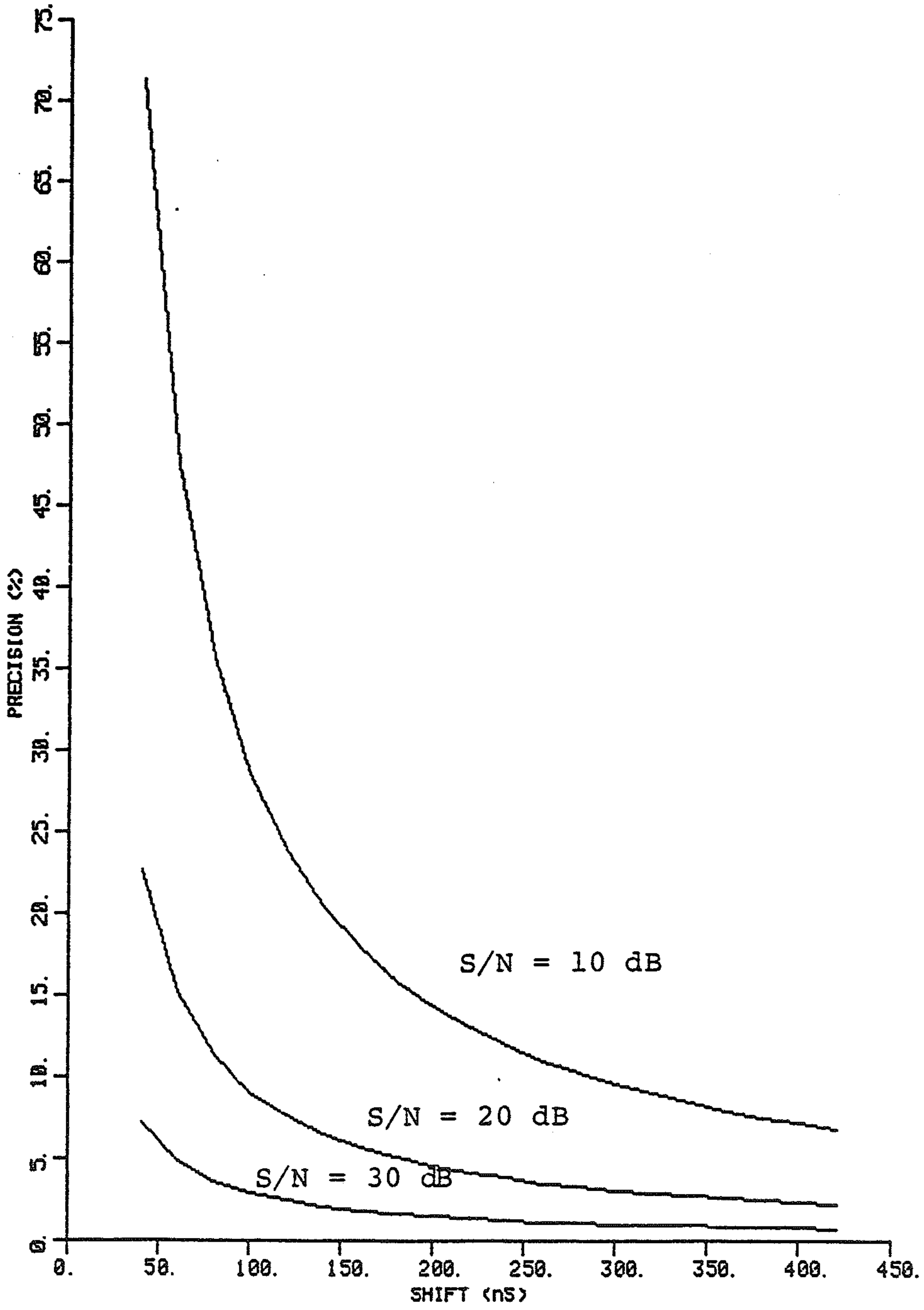

Figure 7 - Theoretical precision of time of arrival estimate versus mean time shift and signal-to-noise ratio. The RMS bandwidth is 2.5 MHz and the echoes are assumed to be perfectly correlated ($\rho = 1$).

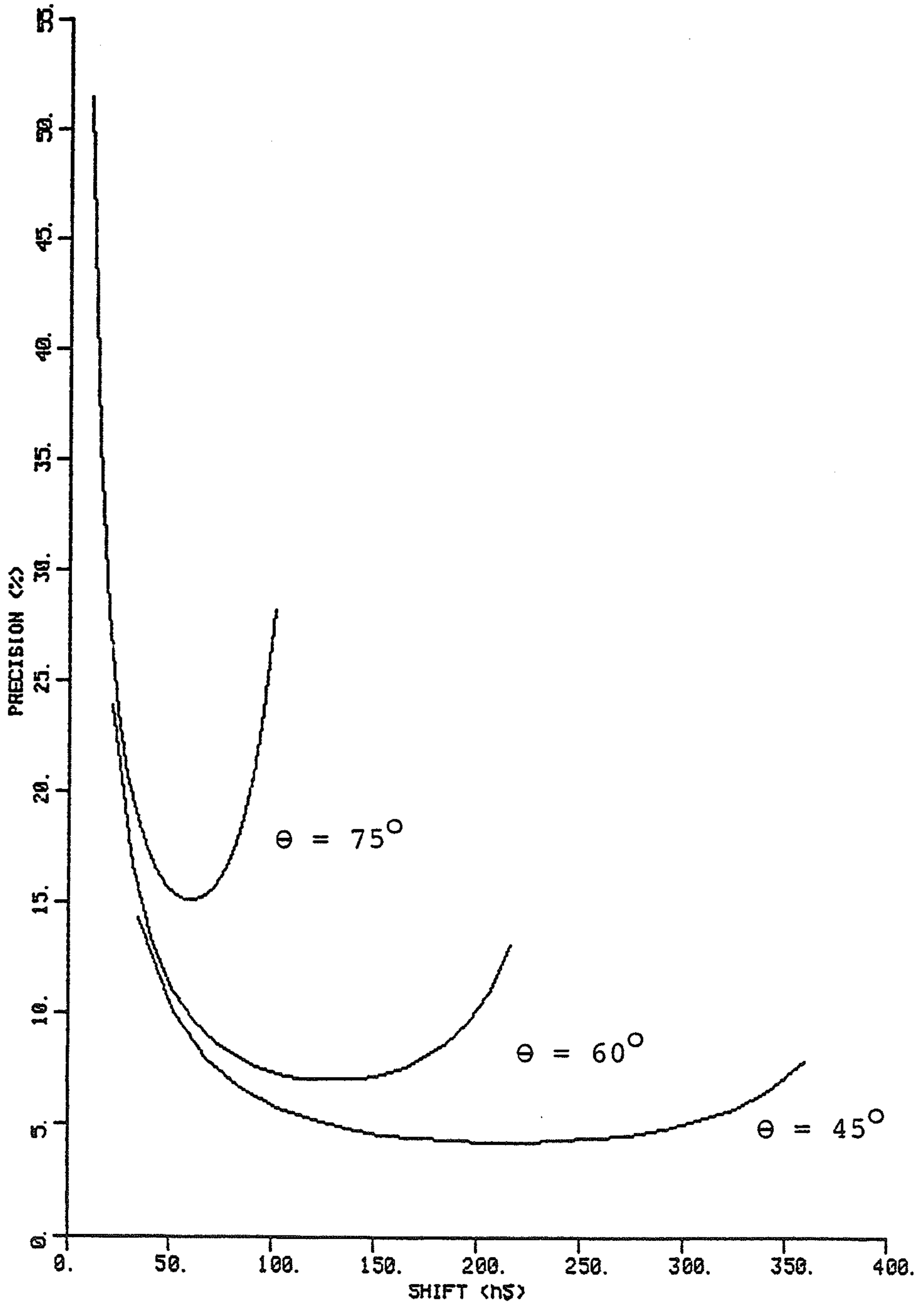

Figure 8 - Theoretical precision of time domain correlation versus time shift between echoes and measurement angle (Θ). The beam decorrelation is assumed to be linear. The signal-to-noise ratio is 20 dB and the RMS bandwidth is 2.5 MHz.

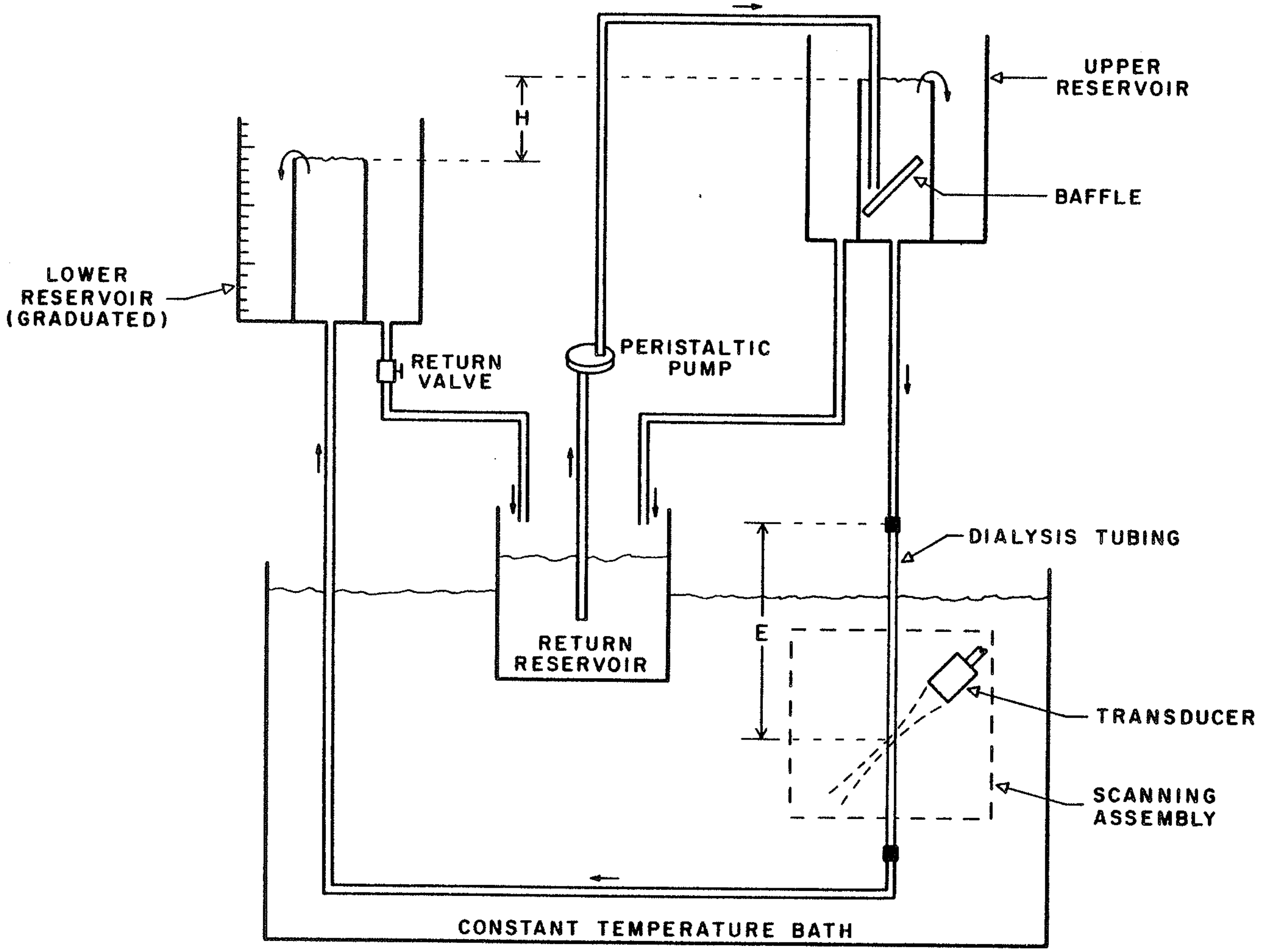

Figure 9 - Experimental blood flow regulation system and blood vessel phantom scanning system.

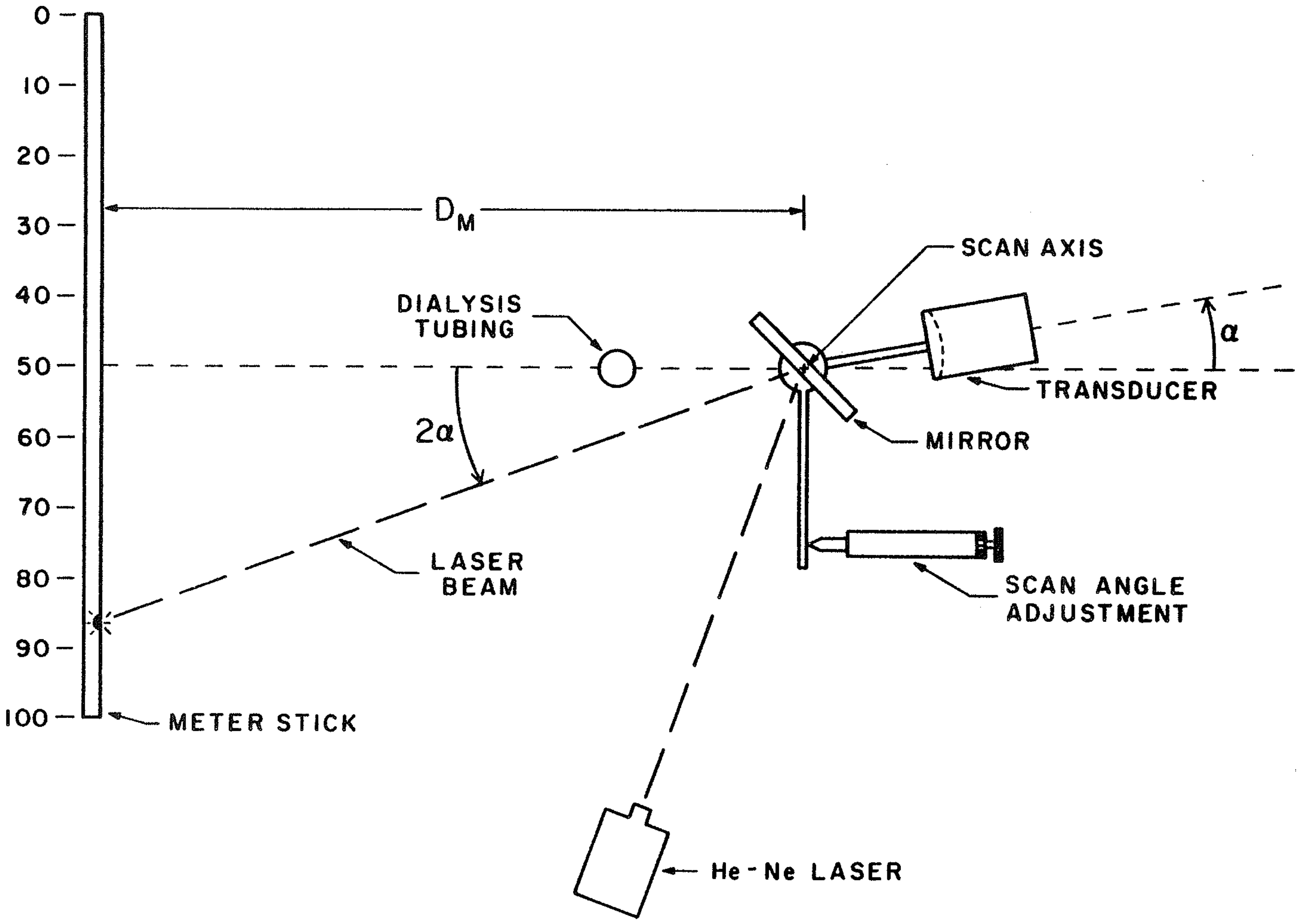

Figure 10 - Laser scan angle measurement system. The distance, D_M, is approximately 2.5 meters and the scan angle (α) is less than 10°.

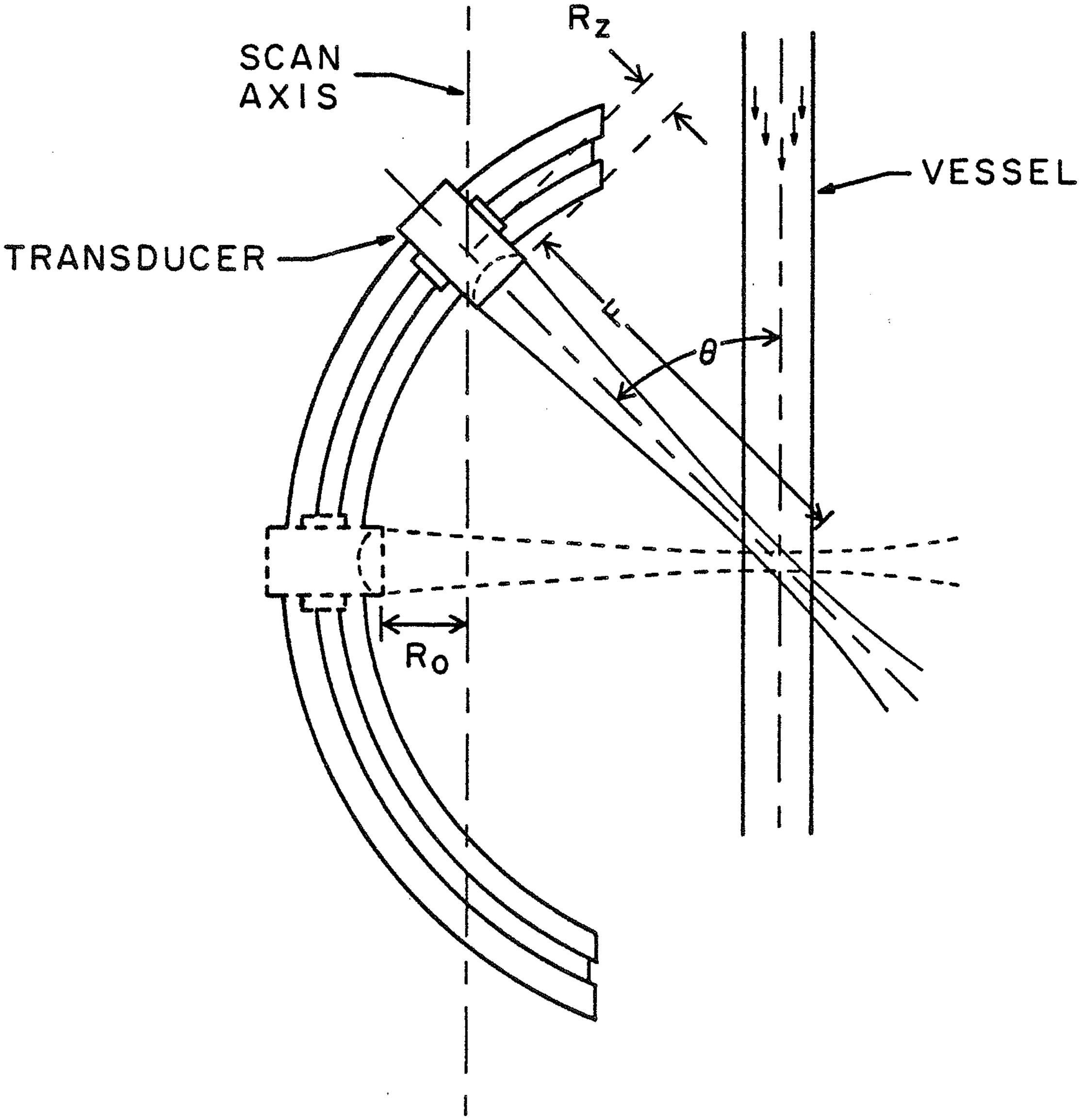

Figure 11 - Transducer scanning assembly and blood vessel phantom. The measurement angle, Θ, can be changed by sliding the transducer along the circular track.

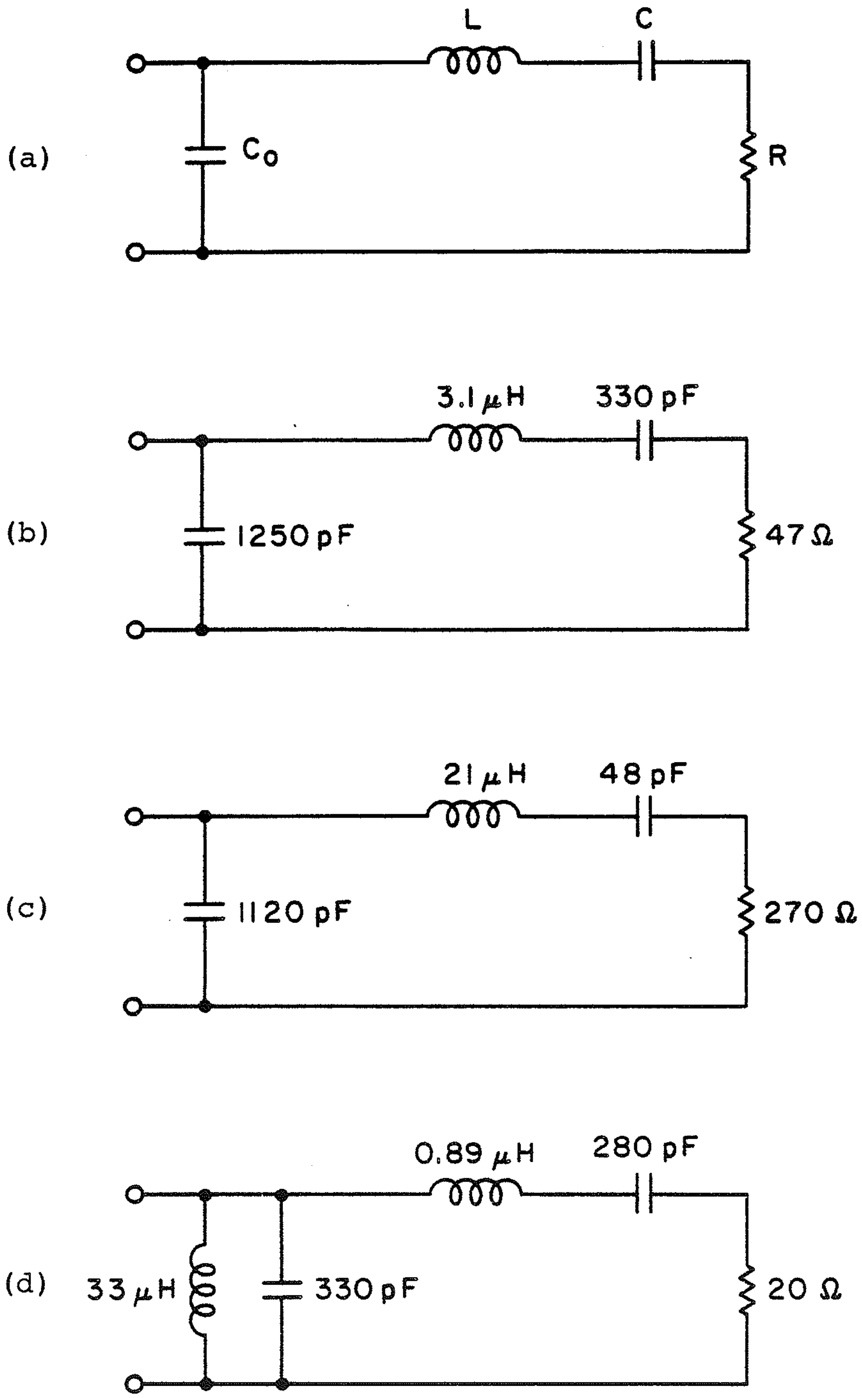

Figure 12 - Measured equivalent electrical circuits of Panametrics transducers.
(a) general model used for transducers.
(b) Transducer 1, V307, 5 MHz, 25.4 mm aperture.
(c) Transducer 2, V309, 5 MHz, 12.7 mm aperture.
(d) Transducer 3, V3323, 10 MHz, 25.4 mm aperture.

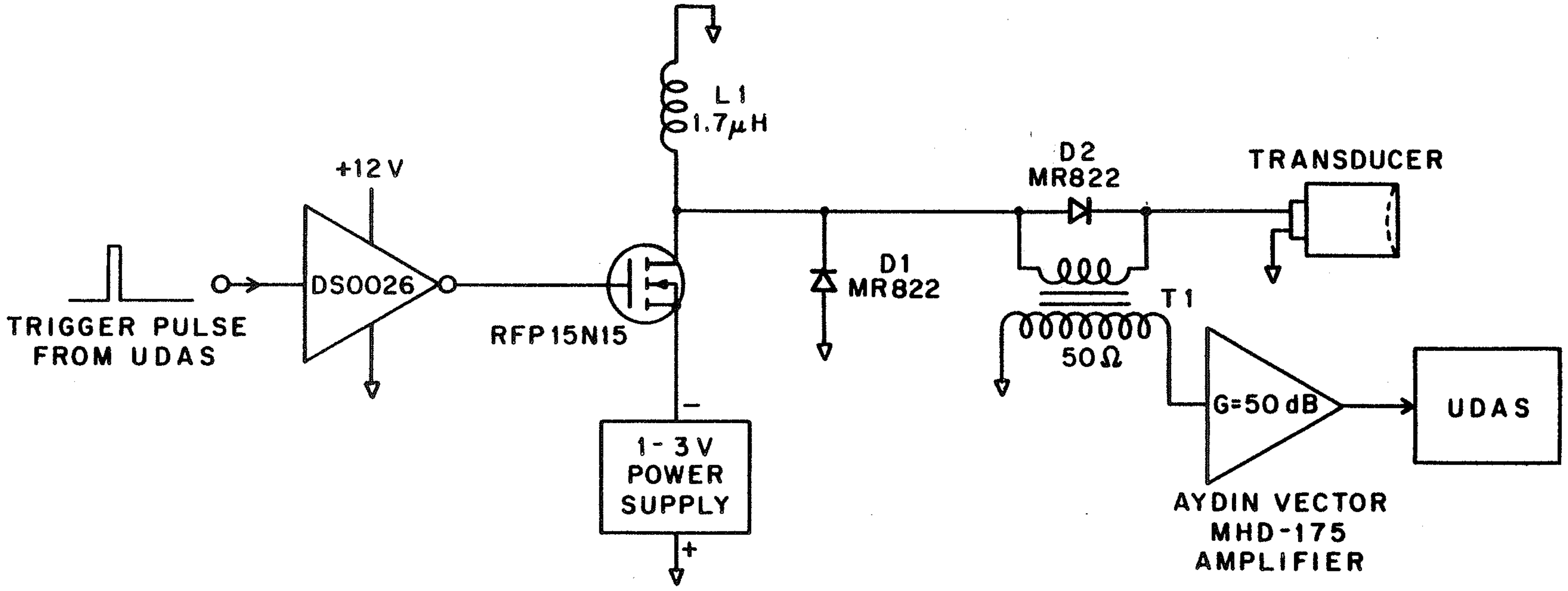

Figure 13 - Pulser-receiver schematic diagram.

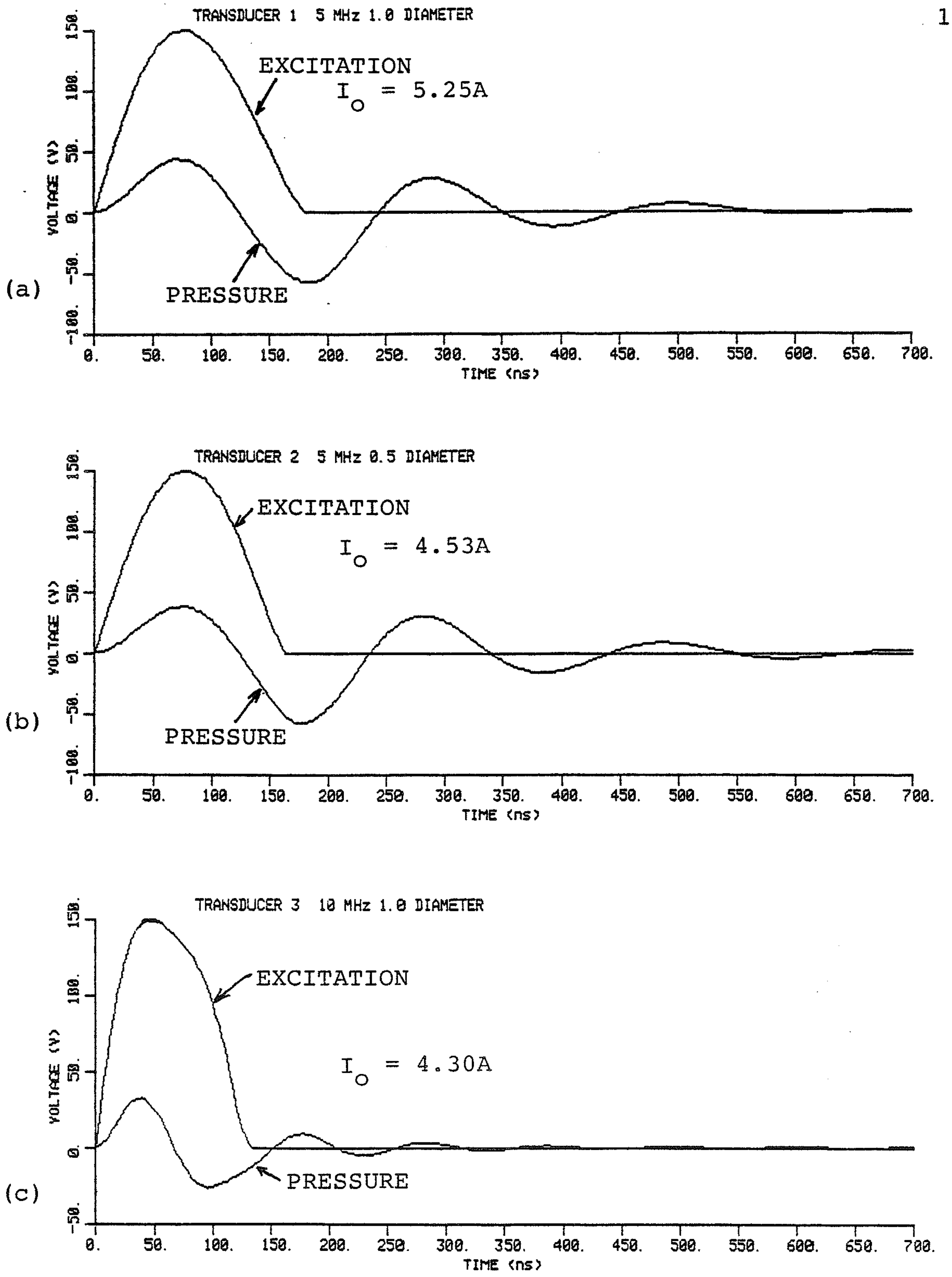

Figure 14 - Transducer SPICE simulation for the three transducers used in this study. For each transducer, the simulated excitation pulse and the accoustic pressure waveforms are shown.
(a) Transducer 1, V307, 5 MHz, 25.4 mm aperture.
(b) Transducer 2, V309, 5 MHz, 12.7 mm aperture.
(c) Transducer 3, V3323, 10 MHz, 25.4 mm aperture.

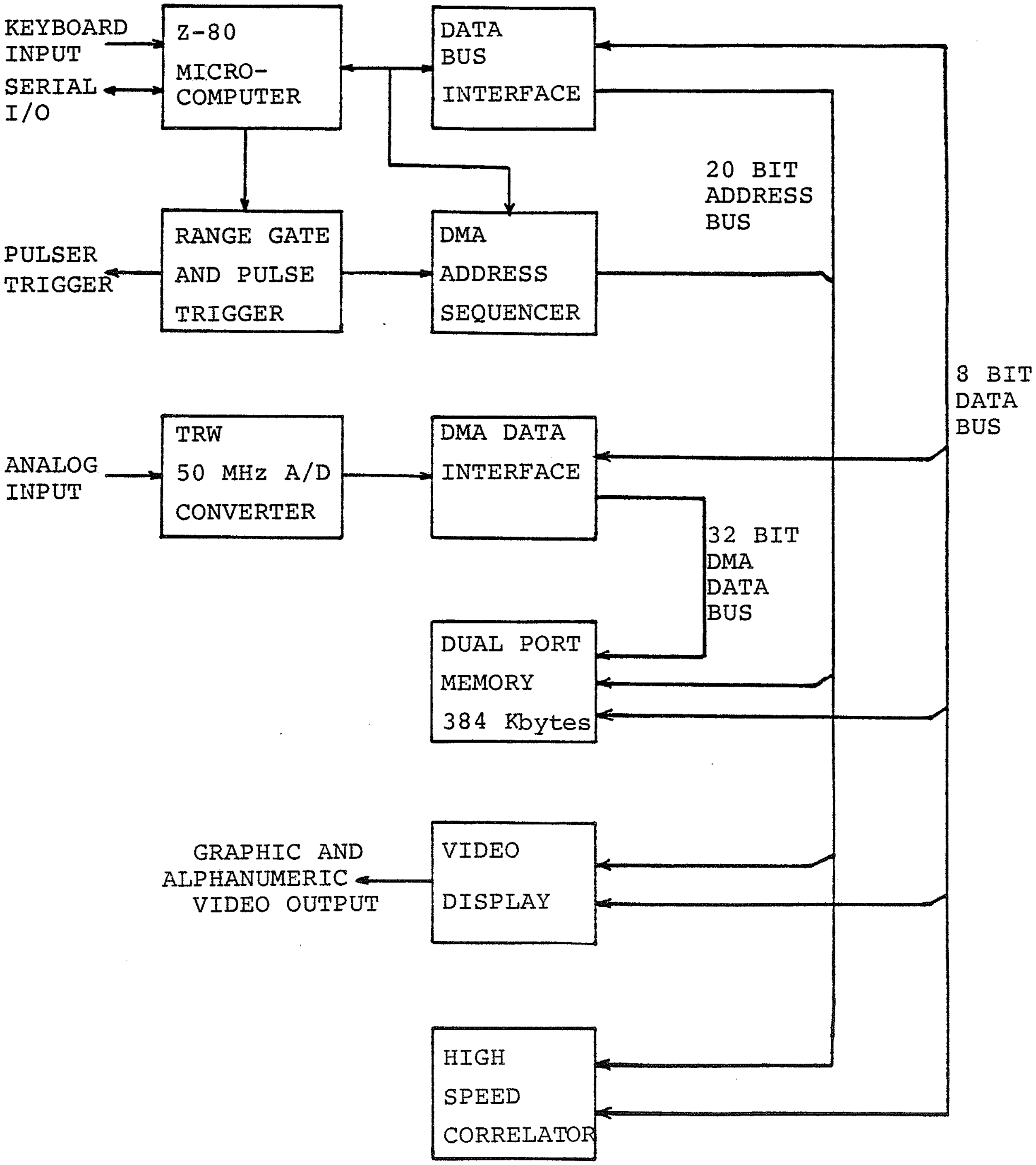

Figure 15 - Block diagram of ultrasound data acquisition system (UDAS).

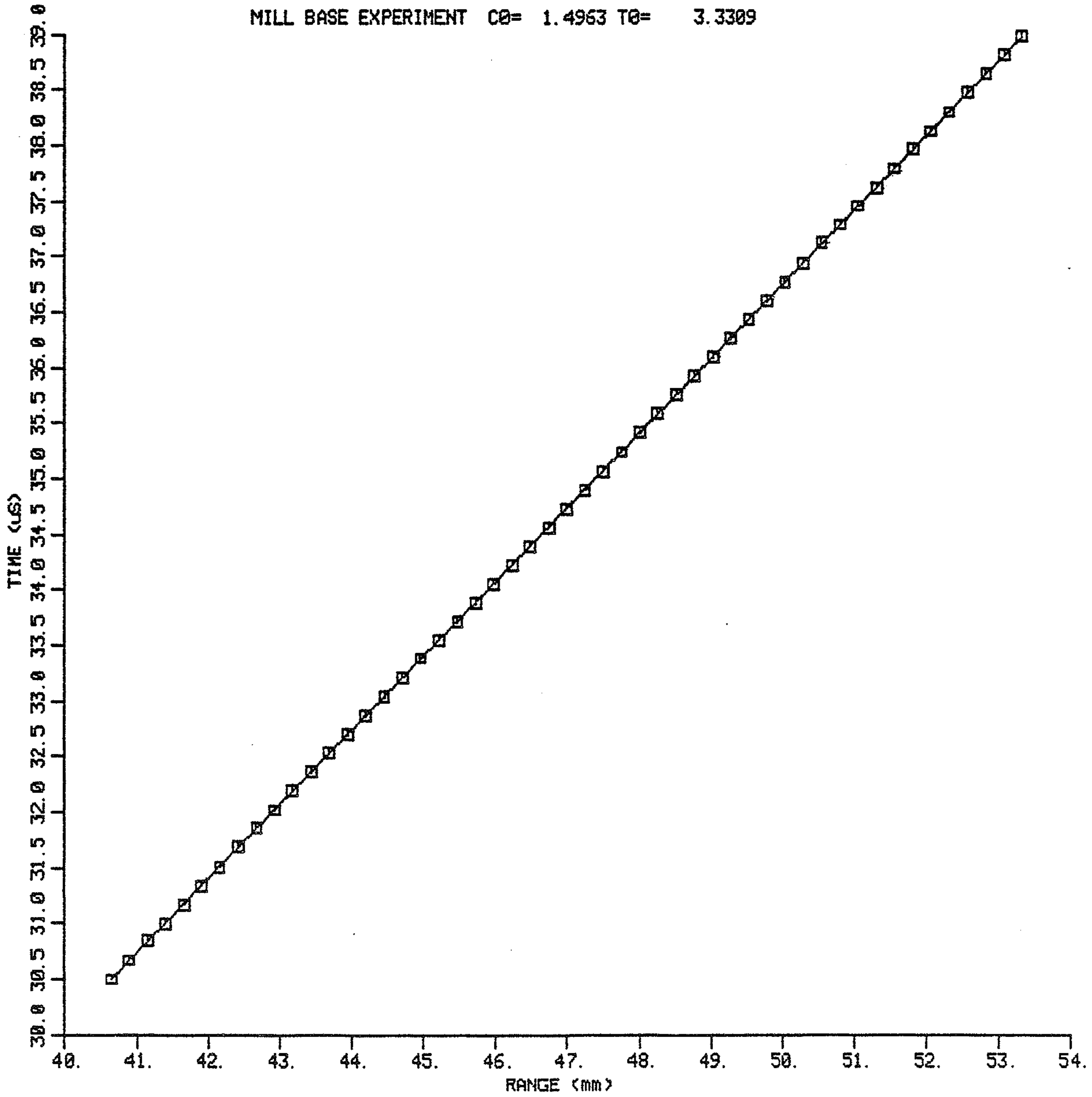

Figure 16 - Plot of one way time of arrival versus range distance measured with the mill base positioning system. A total of 51 time measurements are shown. The least squares linear regression line is used to determine the parameters t_o (time for zero range) and c_o (speed of sound estimated from inverse of the slope of the regression line).

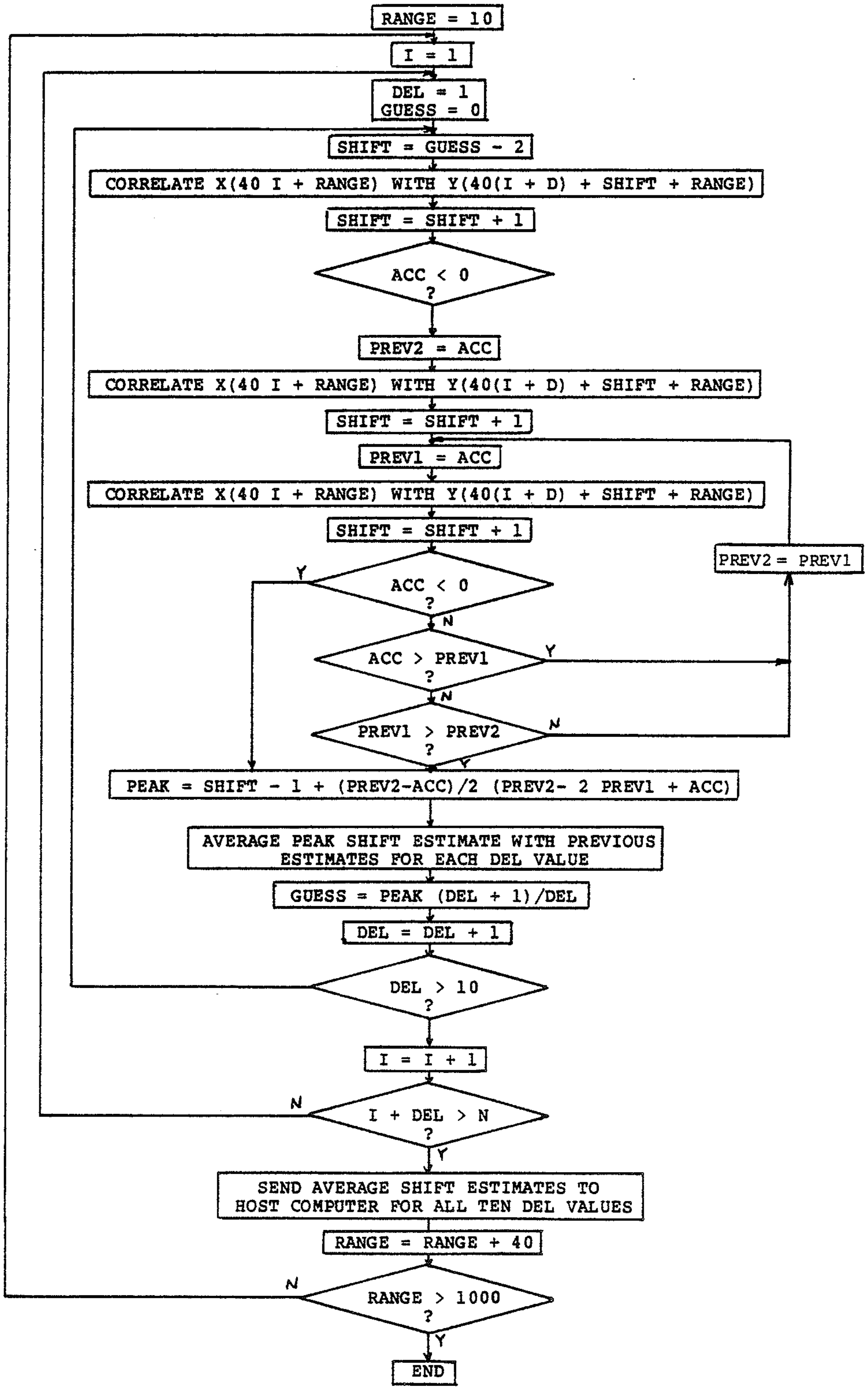

Figure 17 - Flow chart of program to determine the average time shift between 1024 point echoes at 25 range positions.

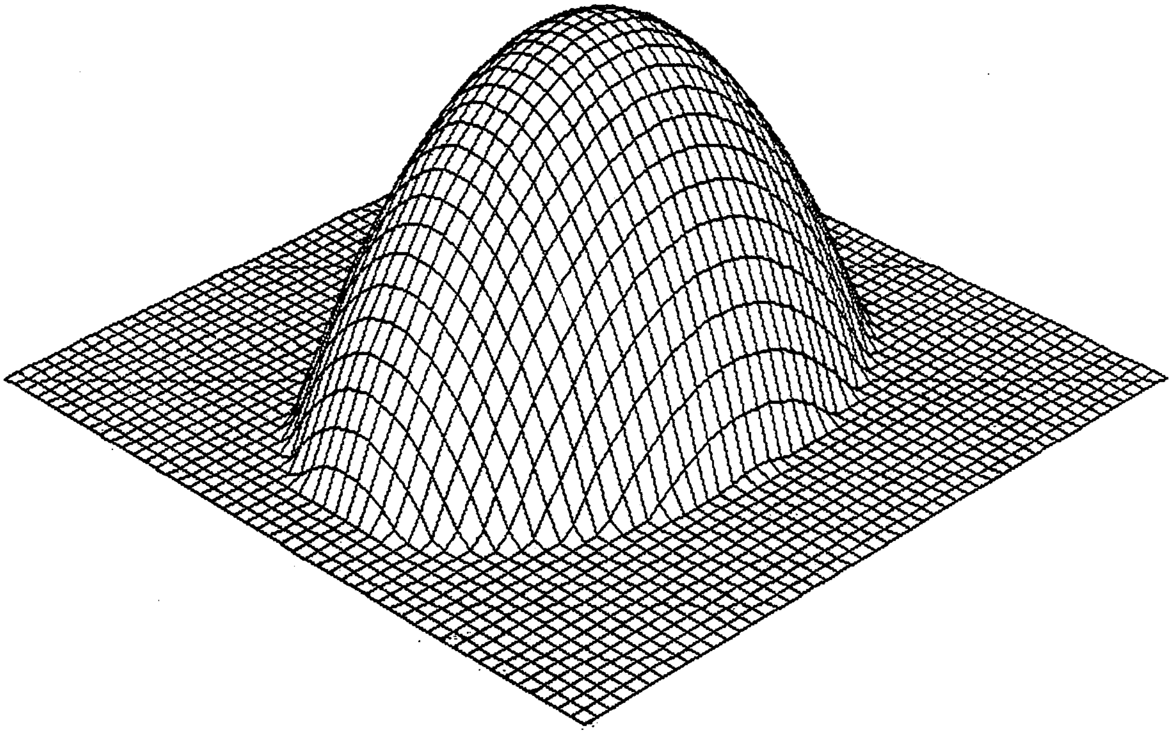

Figure 18 - Simulated 3-D perspective view of an ideal 2-D flow velocity field in a round tube with steady, fully developed, laminar flow.

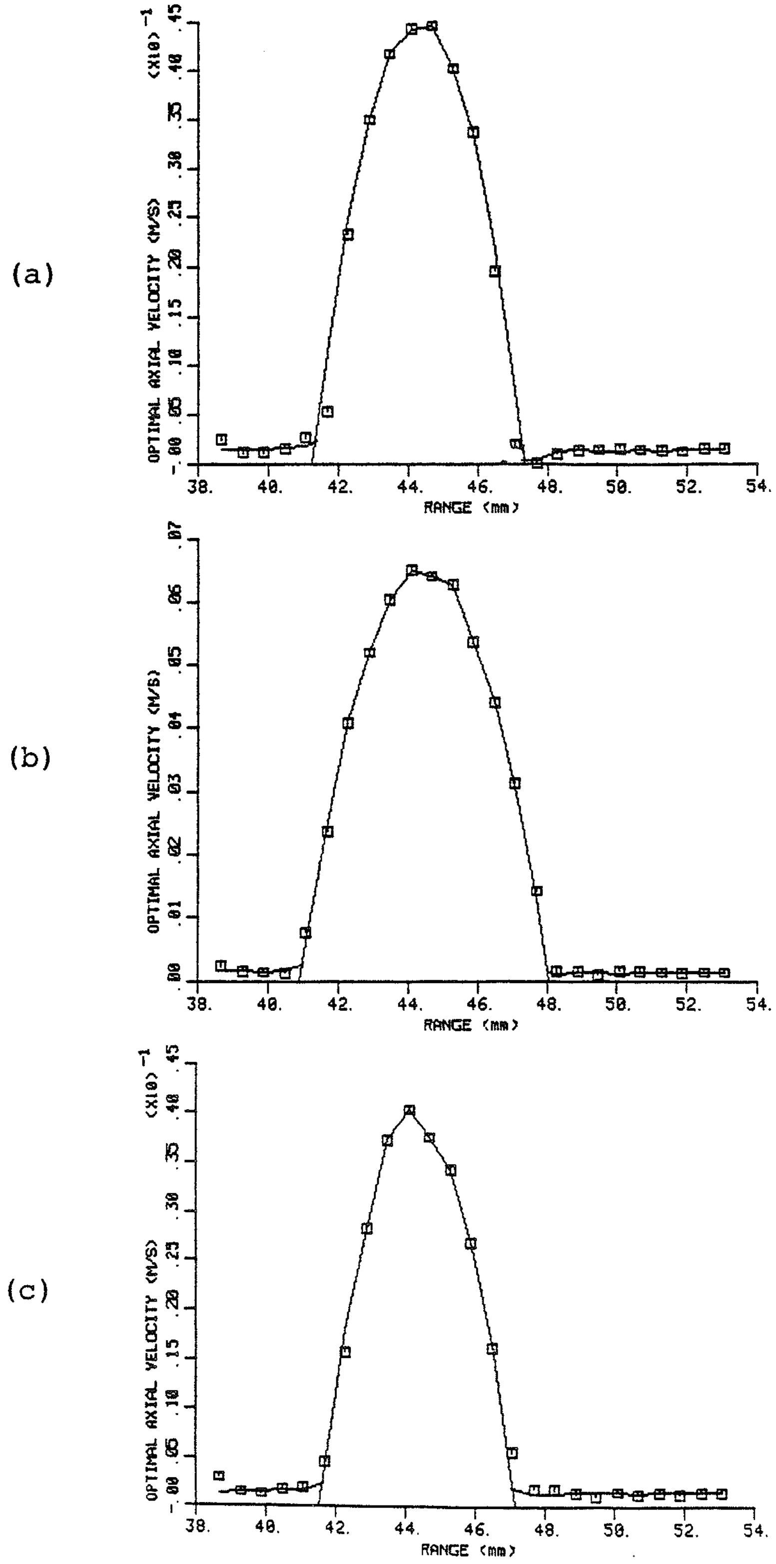

Figure 19 - Three 1-D axial blood flow velocity measurements at three different scan angles (α). Range is the distance from the transducer to the center of each range cell. The distance from the scan axis to the tube center is 40 mm and the measurement angle is 60°. (a) $\alpha = -2.9^{\circ}$, (b) $\alpha = 0.0^{\circ}$, (c) $\alpha = 2.9^{\circ}$.

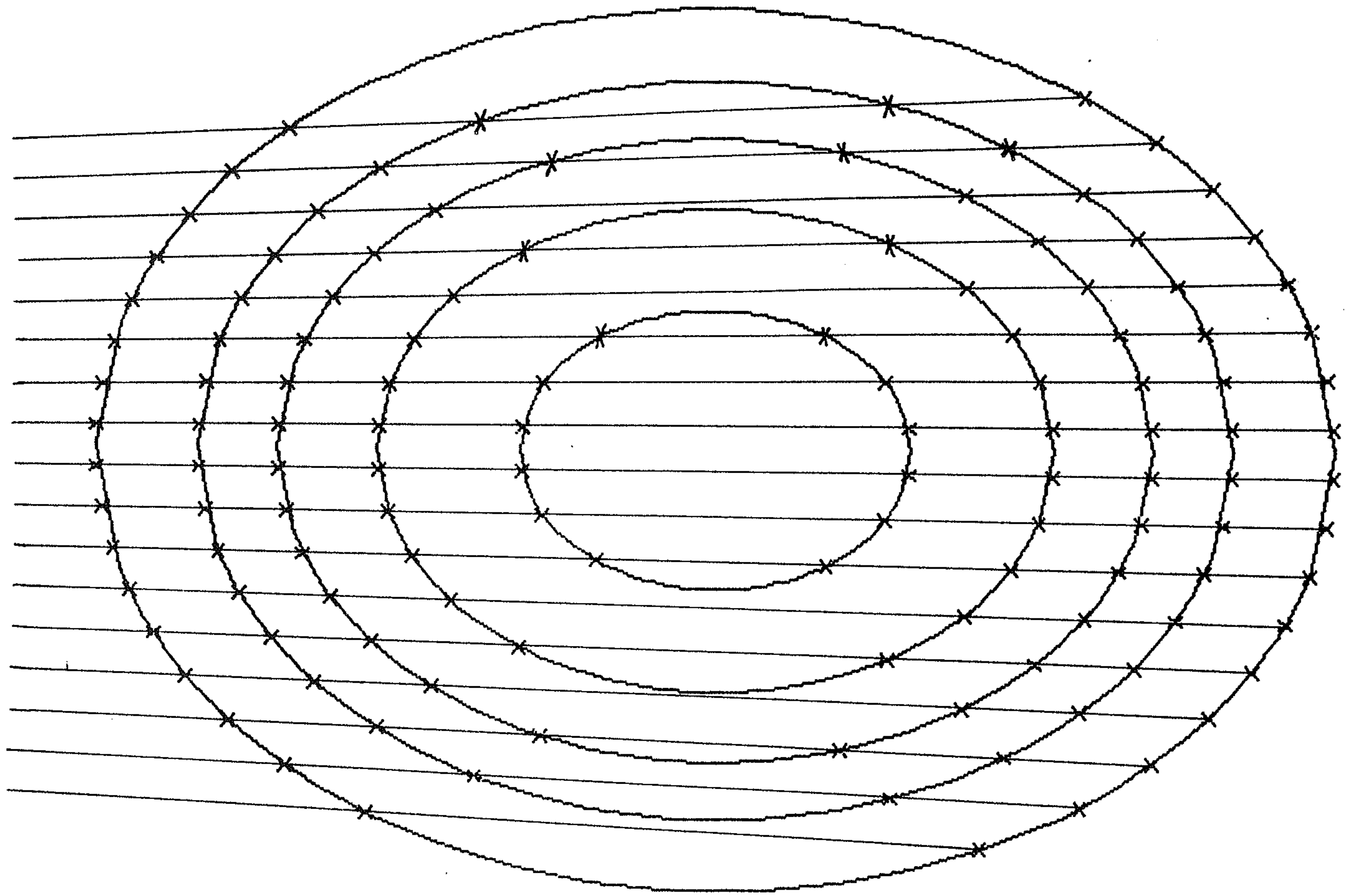

Figure 20 - Simulation of constant velocity ellipses in a round tube at a 45^{o} measurement angle. The distance from the scan axis to the tube center is 8 tube diameters. The straight lines indicate the beam path and the X s indicate constant velocity points.

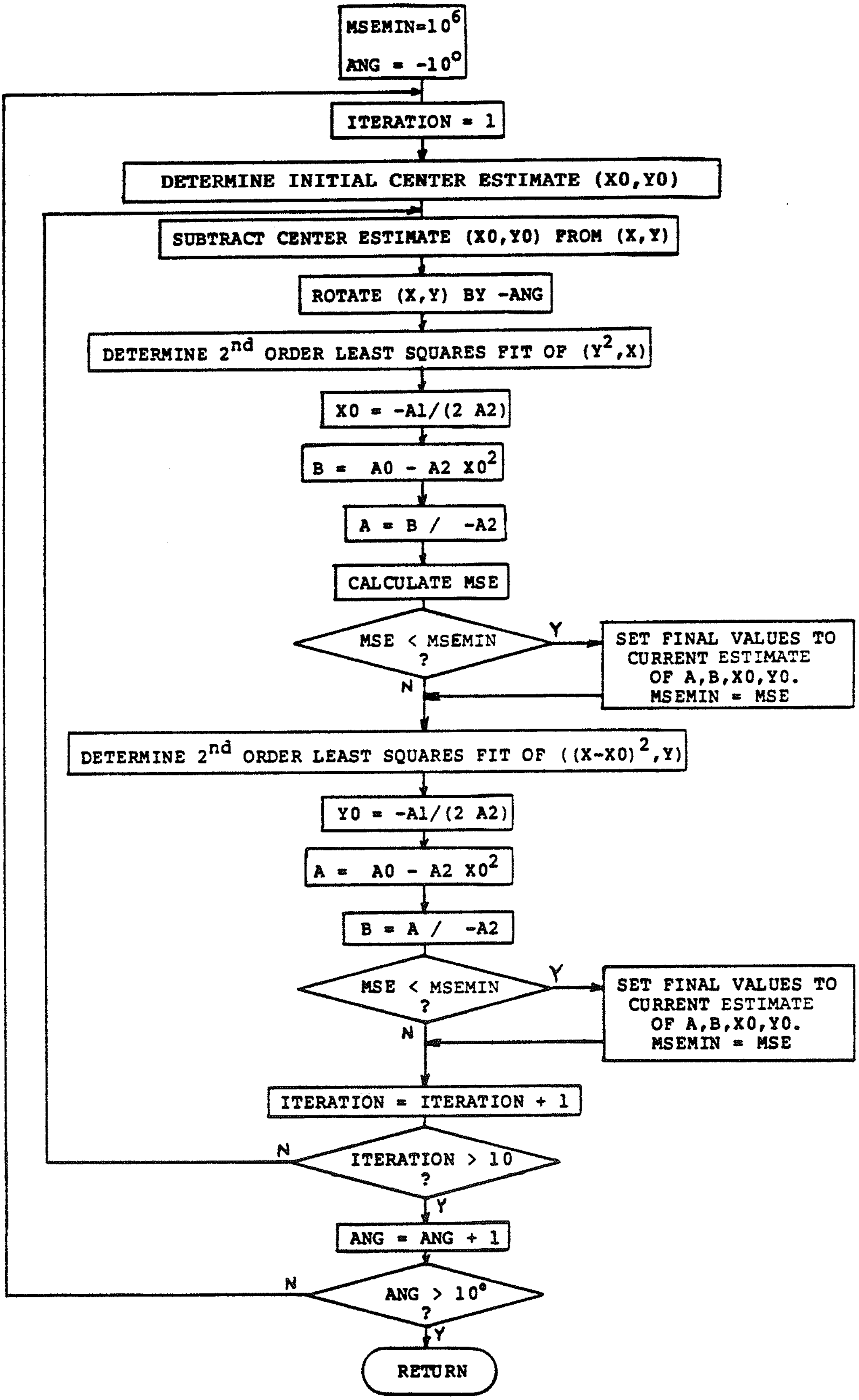

Figure 21 - Flow chart of elliptic fitting procedure.

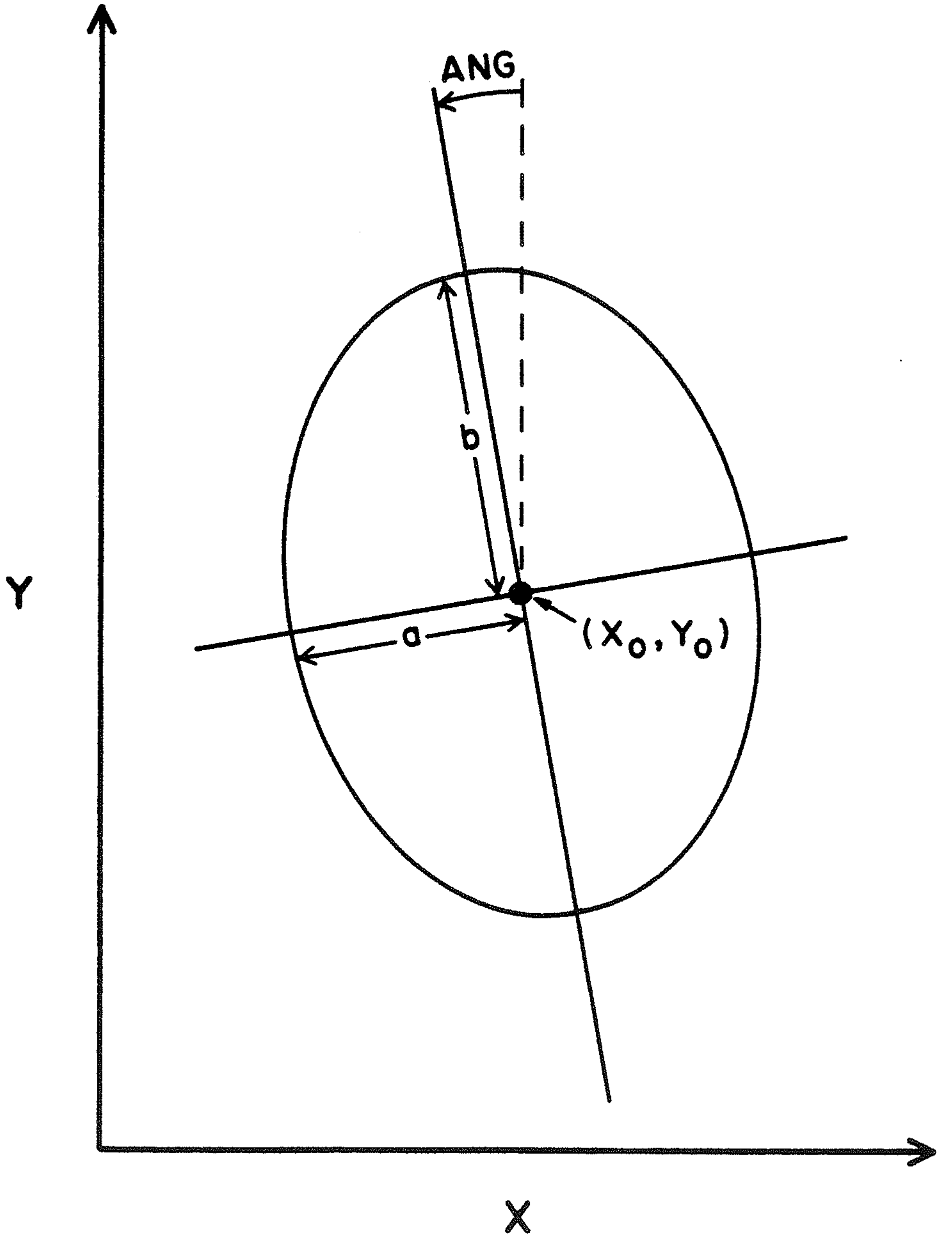

Figure 22 - Definition of the measurement coordinate system and the five parameters required to define a typical constant velocity ellipse.

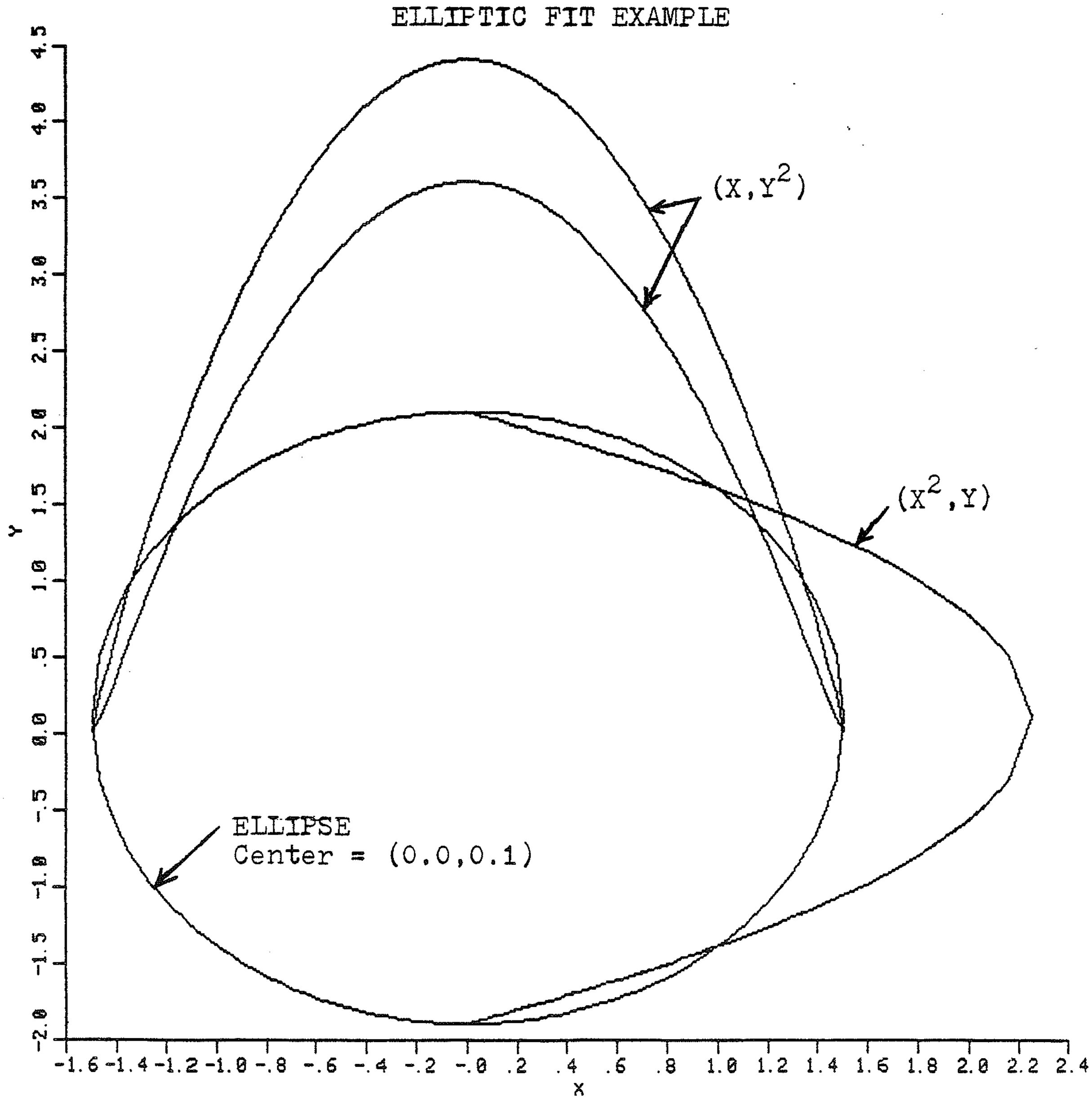

Figure 23 - Example of elliptic fitting showing the (x^2,y) curve and the (x,y^2) curve for a typical unrotated ellipse with center at (0.0,0.1).

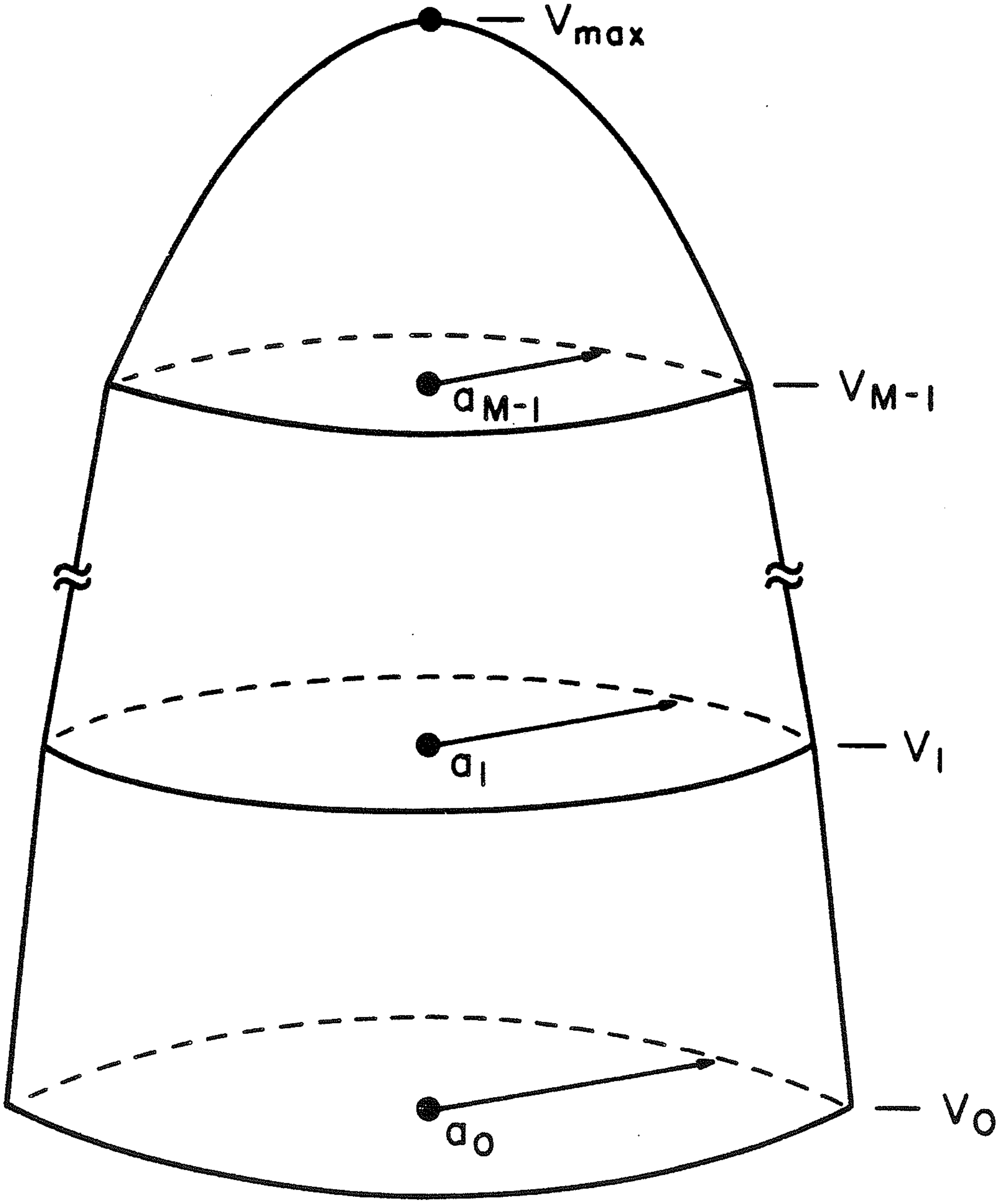

Figure 24 - Illustration of the volume flow integration method. The volume of each right circular conic section is added together in order to estimate the total volume flow inside the tube.

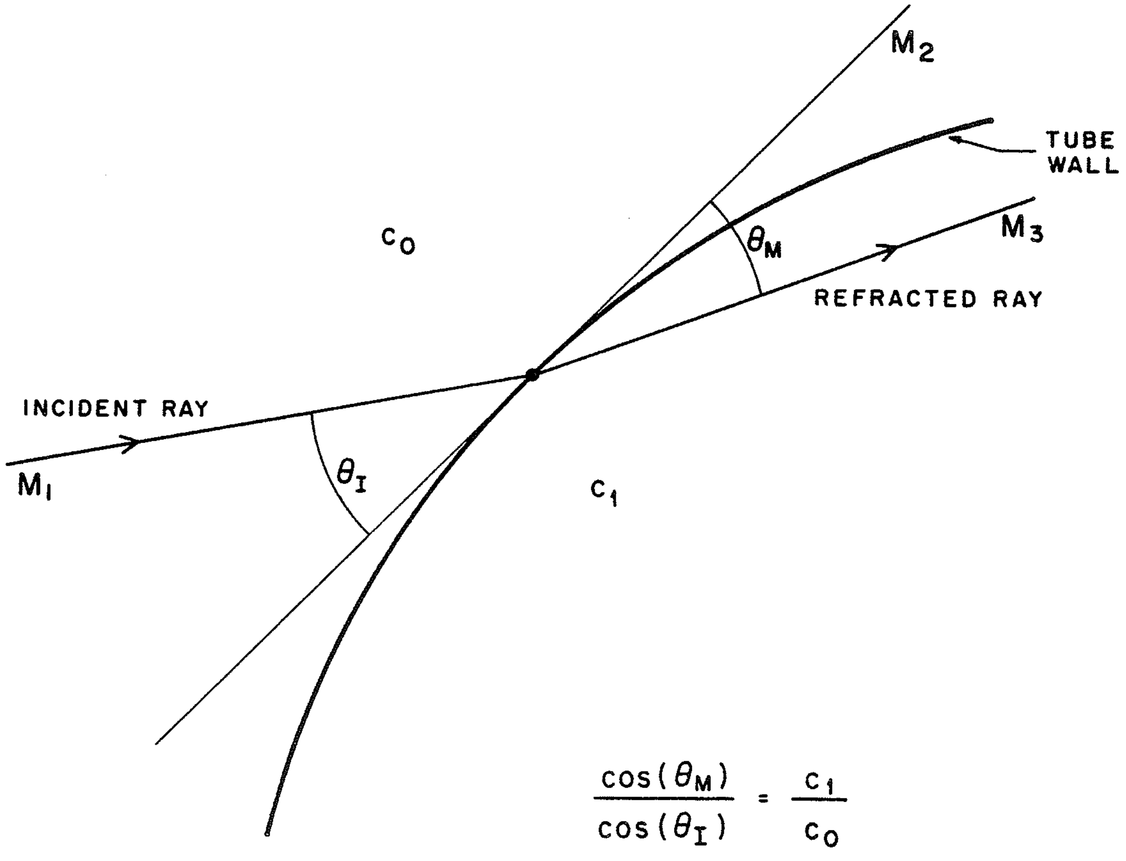

Figure 25 - Schematic representation of incident ultrasonic beam from the left passing through a section of a round tube and being refracted by the different speed of sound inside the tube. Snell's law relates the angles Θ_I and Θ_M as shown.

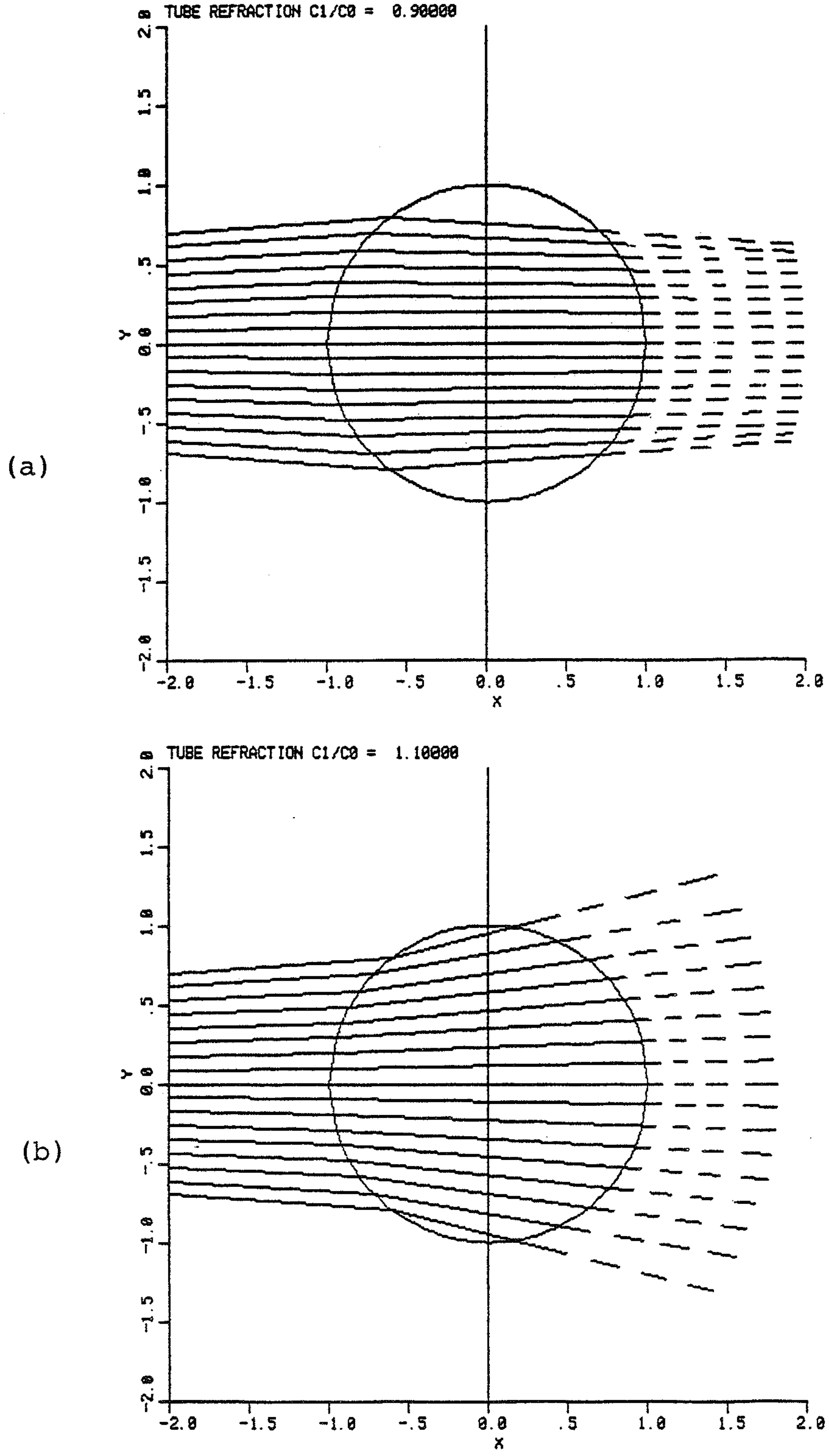

Figure 26 - Simulation of refraction of an ultrasonic beam as it passes through a round tube. The transducer beam is normal to the axis of the vessel.

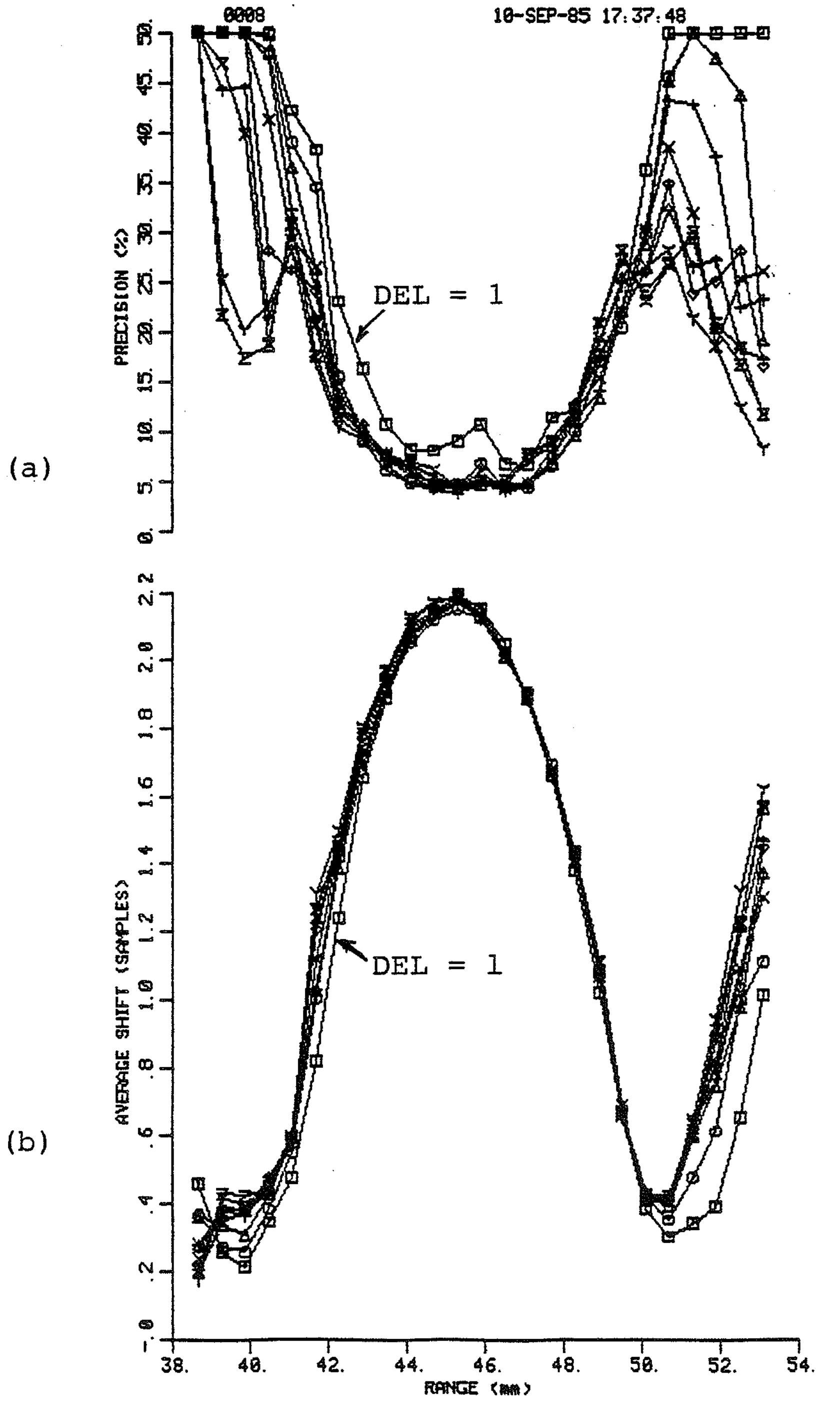

Figure 27 - Shift precision (a) and average sample shift (b) of received echoes versus range for ten different DEL values determined from a Sephadex^{R} experiment at a measurement angle of 45° using 384 echoes (PRF = 3125 Hz).

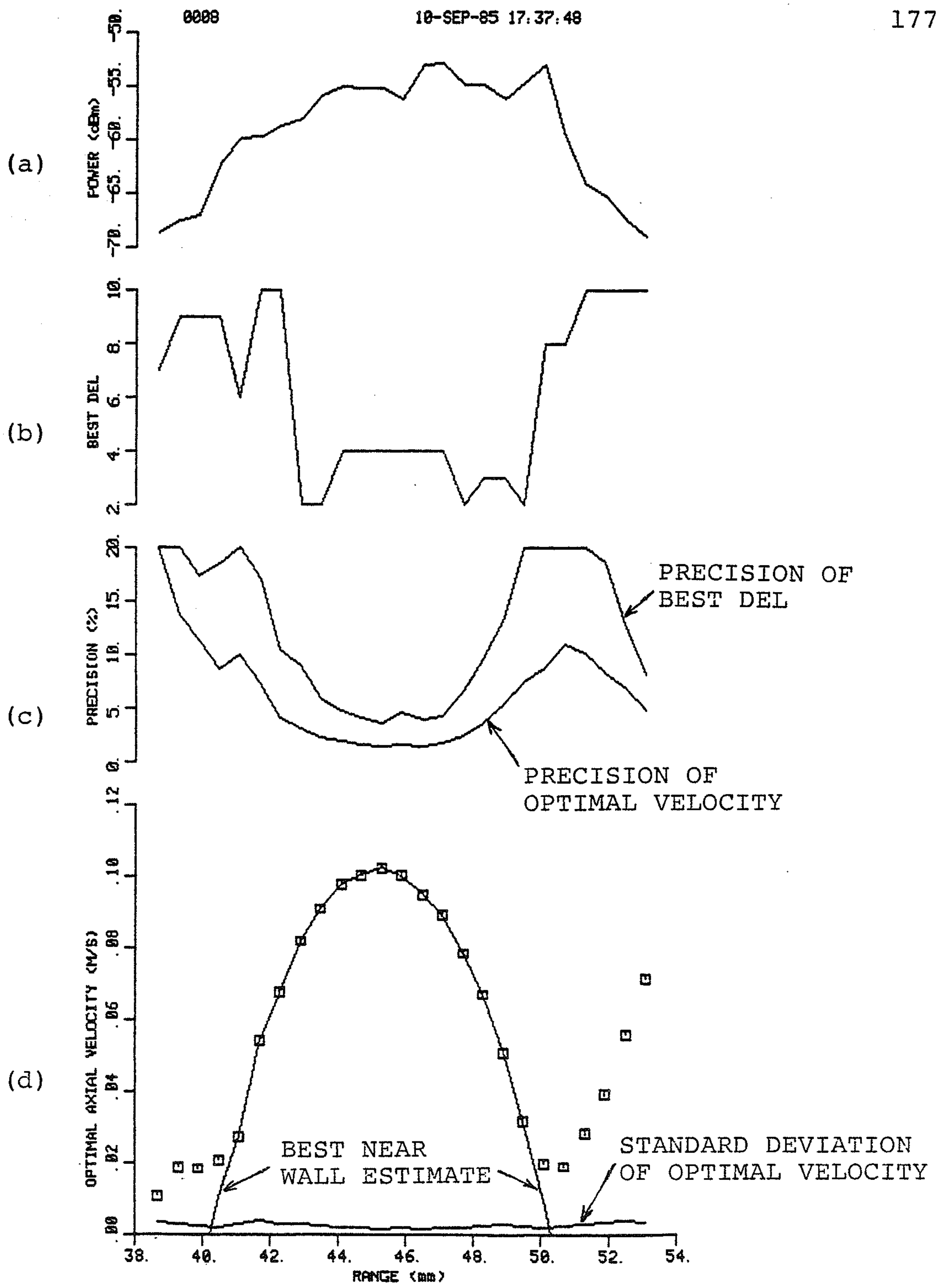

Figure 28 - Optimum axial velocity estimate data versus range for the data shown in Figure 27. The received input power in dBm of the sampled echoes versus range (a), the best DEL value (DEL with lowest variance) versus range (b), the precision of the optimal estimate and the precision of the best DEL value estimate versus range (c) and the optimal axial velocity estimate versus range (d) are shown.

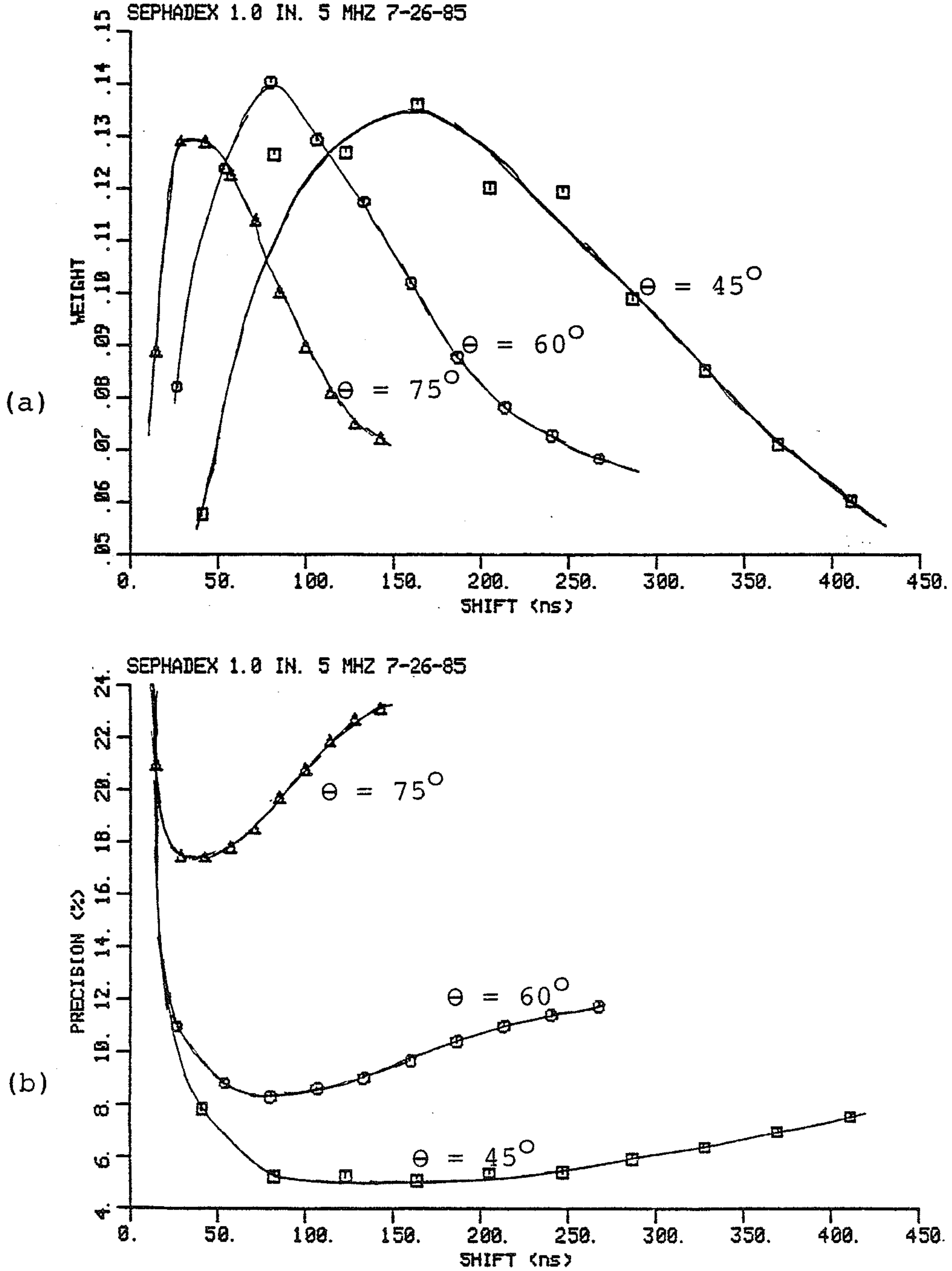

Figure 29 - Weighting function (a) and precision (b) of a midstream axial flow velocity measurement versus time shift and measurement angle for transducer one (5 MHz center frequency, 25.4 mm aperture). The trend in the experimental data is shown by the hand drawn solid lines.

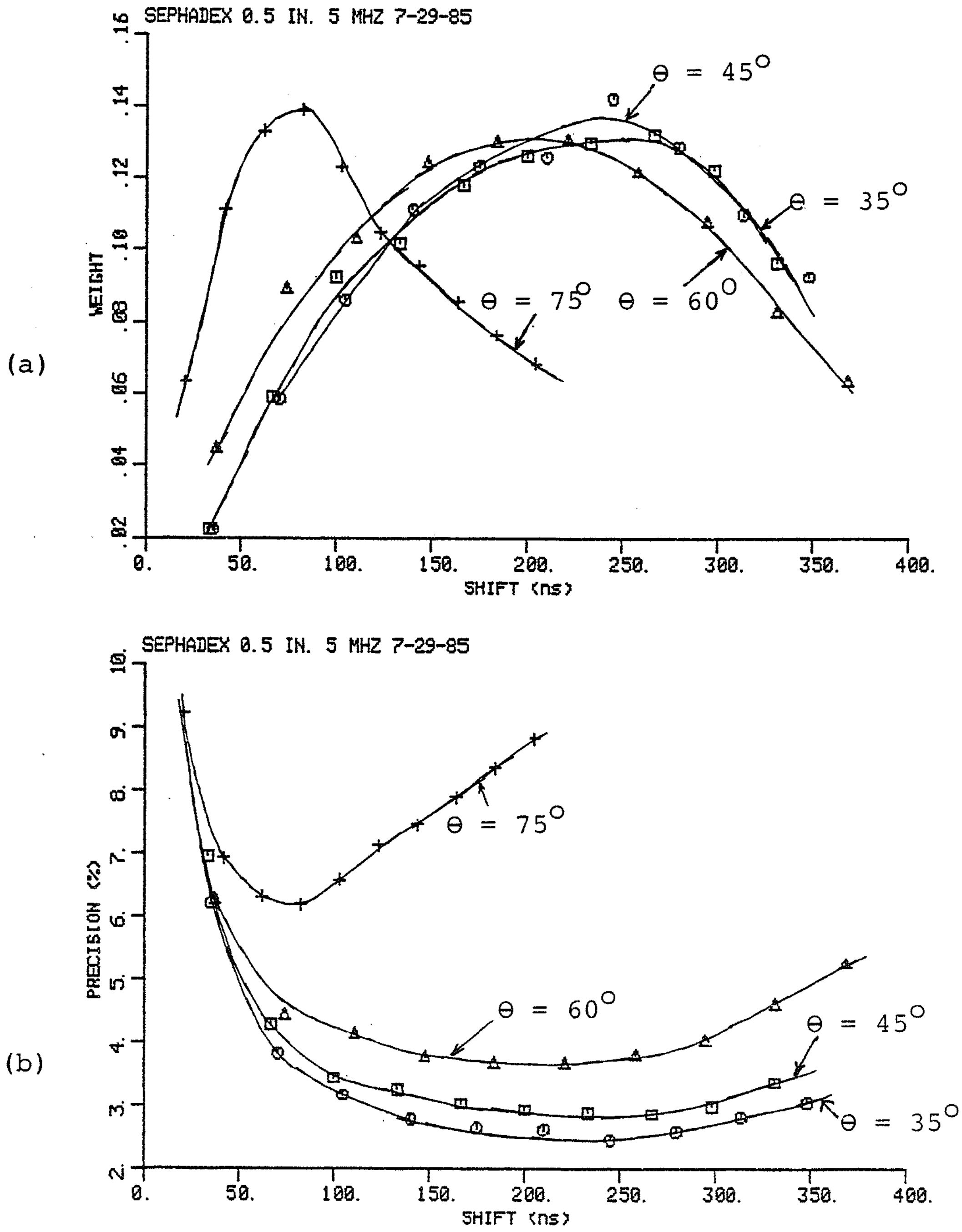

Figure 30 - Weighting function (a) and precision (b) of a midstream axial flow velocity measurement versus time shift and measurement angle for transducer two (5 MHz center frequency, 12.7 mm aperture). The trend in the experimental data is shown by the hand drawn solid lines.

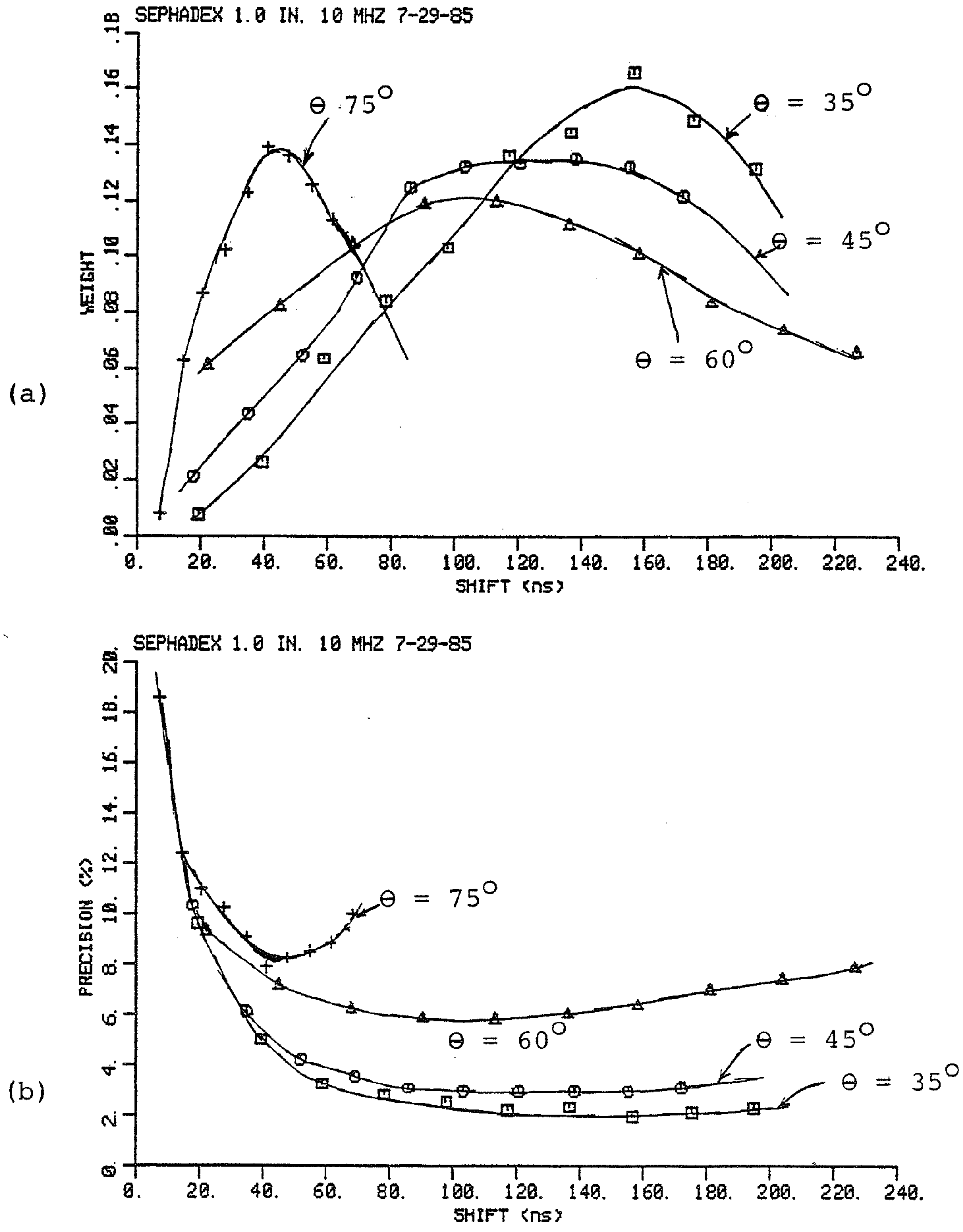

Figure 31 - Weighting function (a) and precision (b) of a midstream axial flow velocity measurement versus time shift and measurement angle for transducer three (10 MHz center frequency, 25.4 mm aperture). The trend in the experimental data is shown by the hand drawn solid lines.

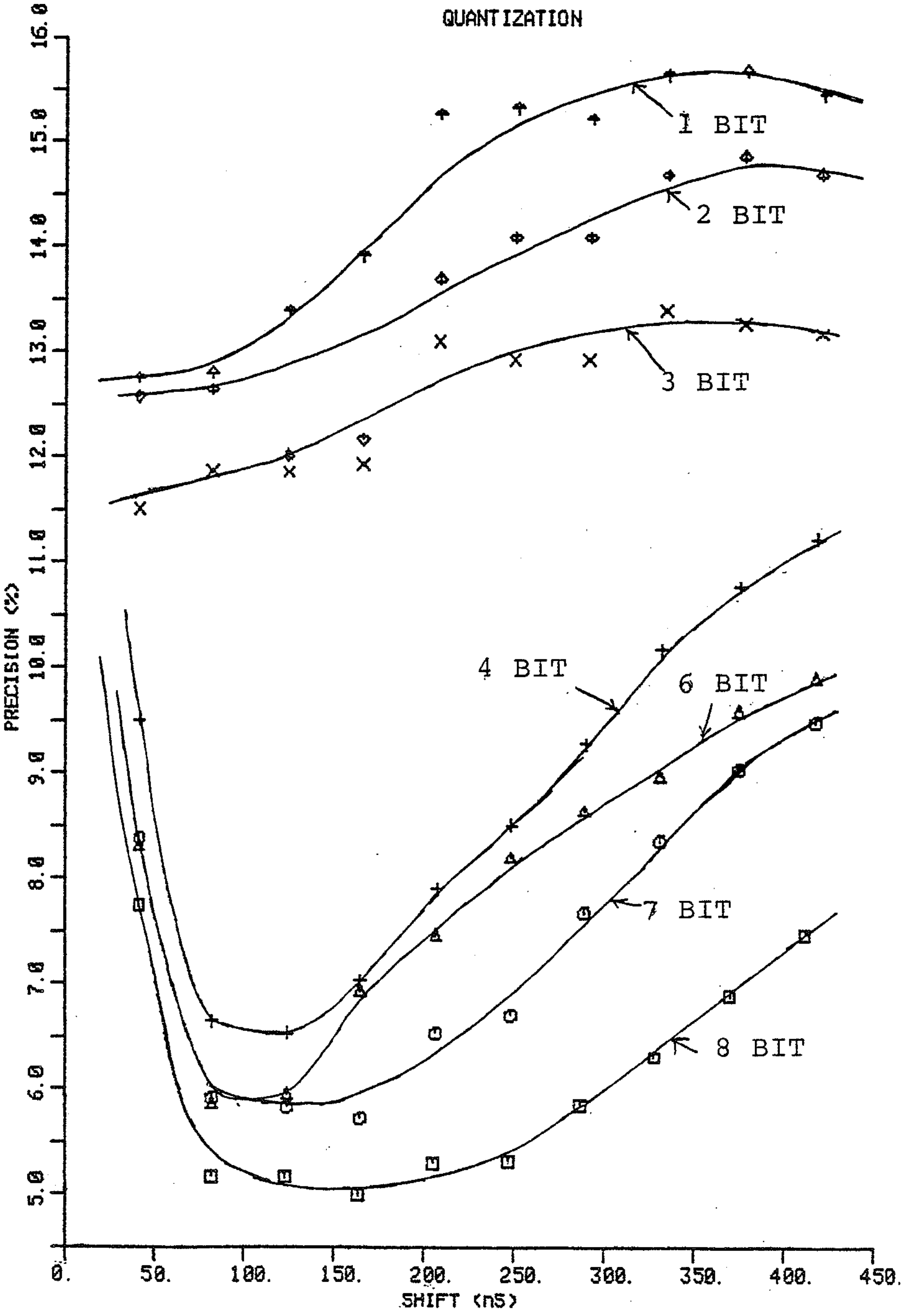

Figure 32 - Precision of a time domain flow measurement versus time shift and bits of quantization. The original data were sampled with 8 bits of quantization and the other reduced quantization measurements were obtained by rounding the 8 bit data. The trend in the experimental data is shown by the hand drawn solid lines.

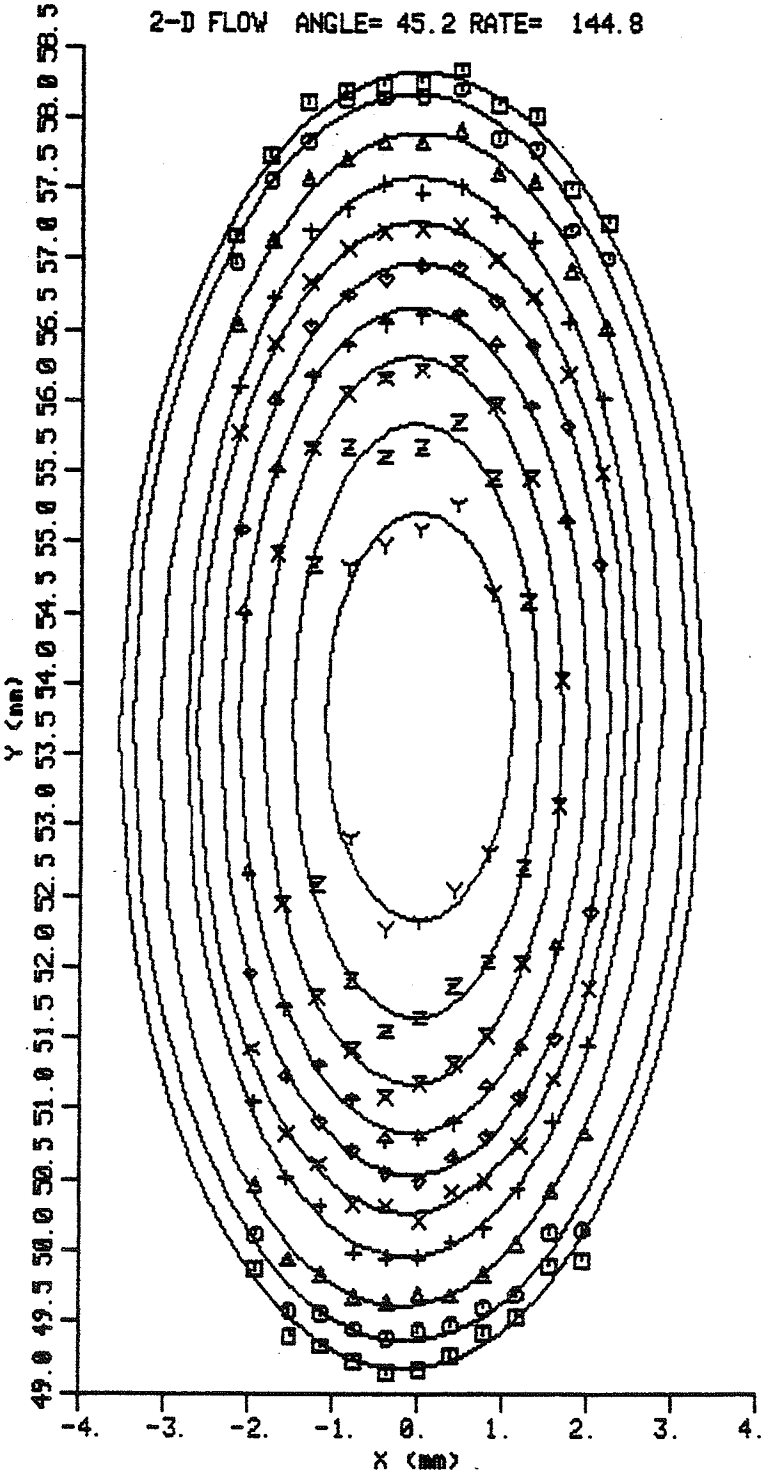

Figure 33 - Constant velocity ellipse data from a Sephadex^R experiment at a track setting of 45°. Eleven scan angles are shown for this data set (SEP095). The measurement angle and volume flow estimates are shown at the top of the graph.

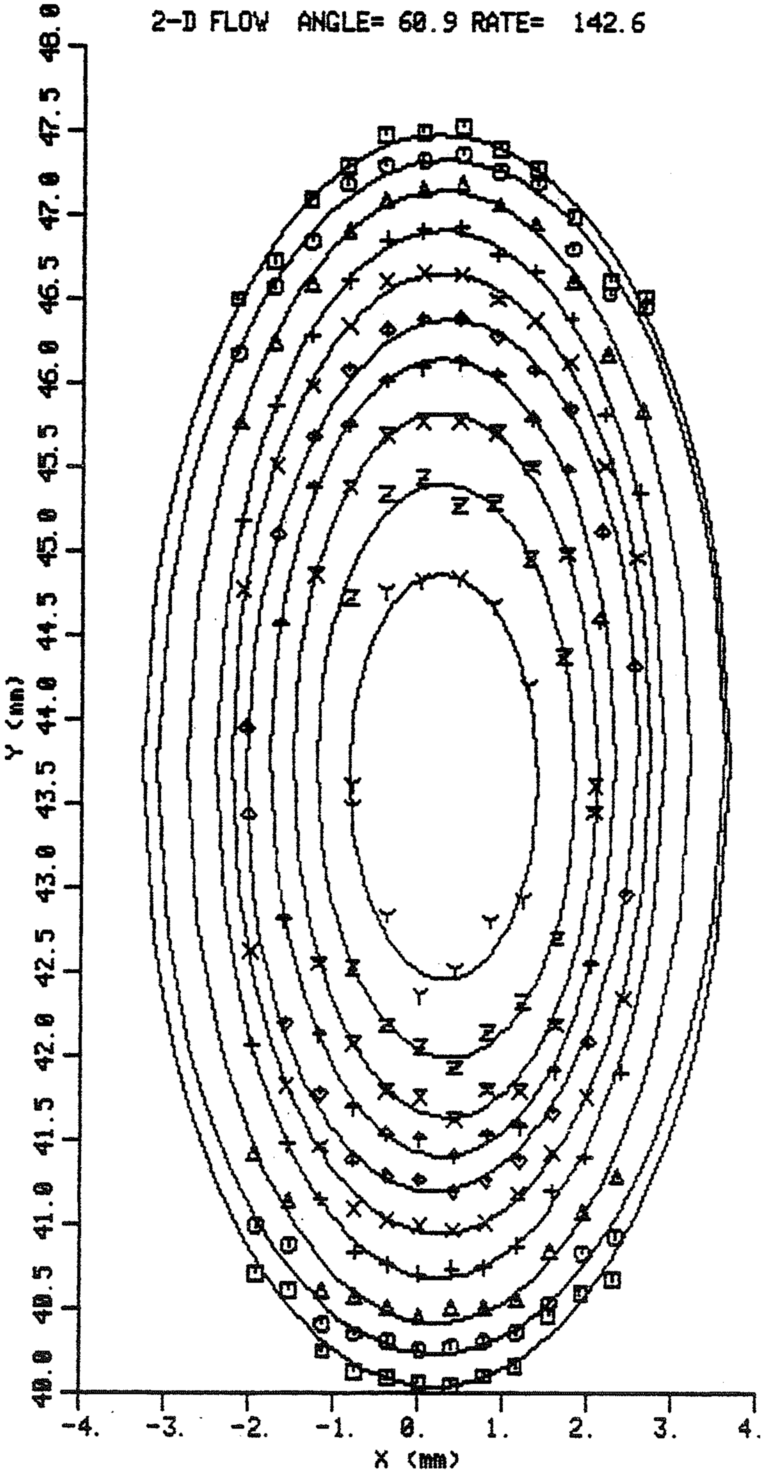

Figure 34 - Constant velocity ellipse data from a Sephadex^R experiment at a track setting of 60°. Twelve scan angles are shown for this data set (SEP102). The measurement angle and volume flow estimates are shown at the top of the graph.

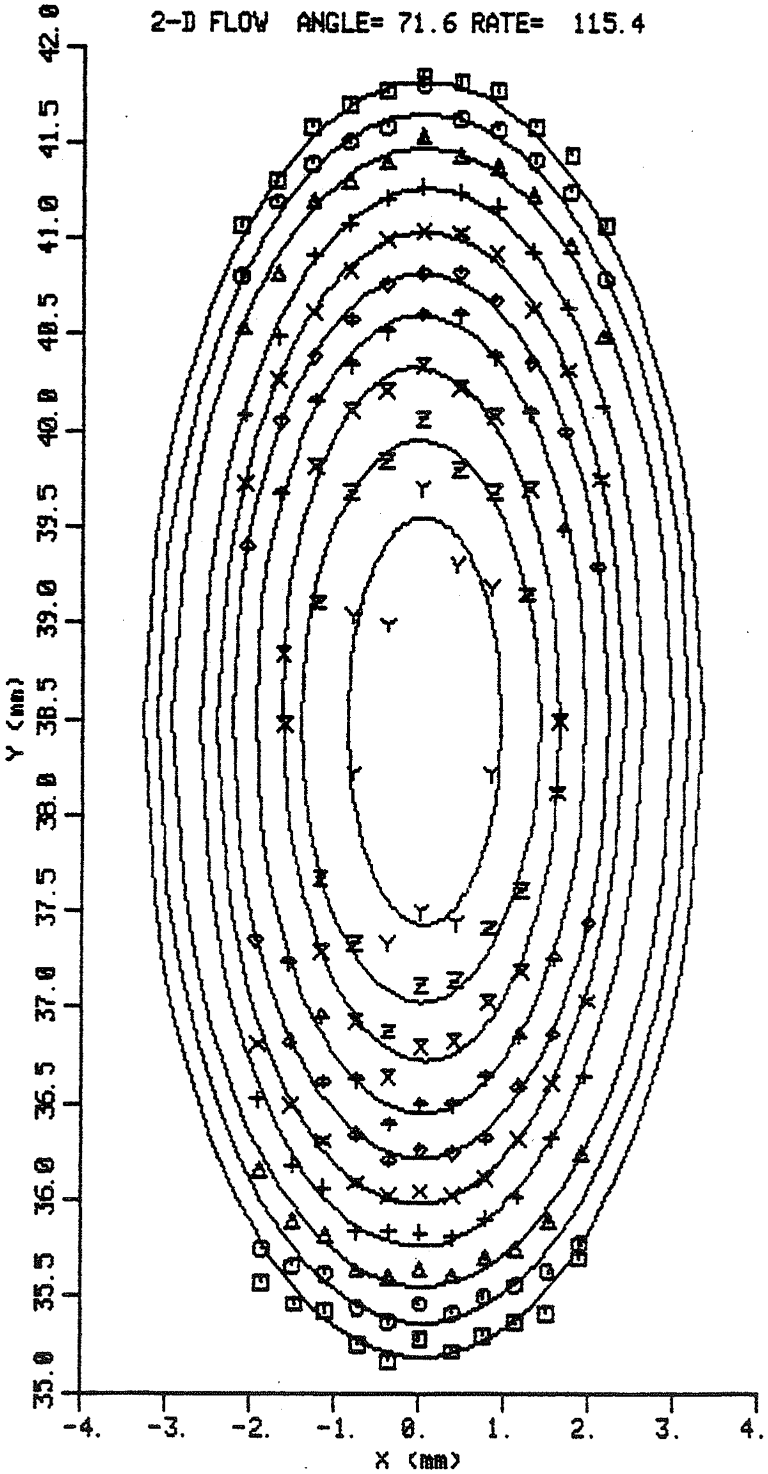

Figure 35 - Constant velocity ellipse data from two Sephadex^{R} experiment at a track setting of 75°. Eleven scan angles are shown for this data set (SEP101). The measurement angle and volume flow estimates are shown at the top of the graph.

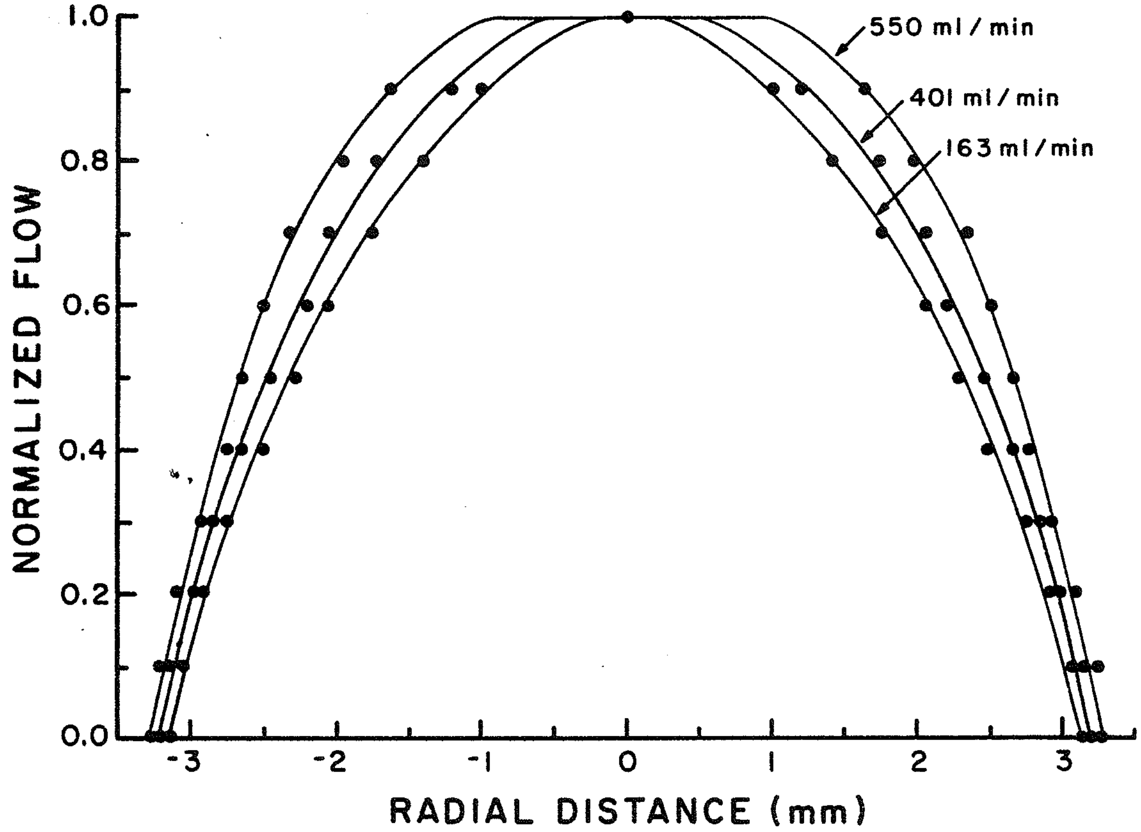

Figure 36 - Plot of measured axial flow velocity profiles obtained from three different volume flow experiments (JAN114, JAN116, and JAN117). The peak velocity is normalized to 1.0. The minor axes of ten constant velocity ellipses for each experiment are plotted versus the normalized flow velocity.

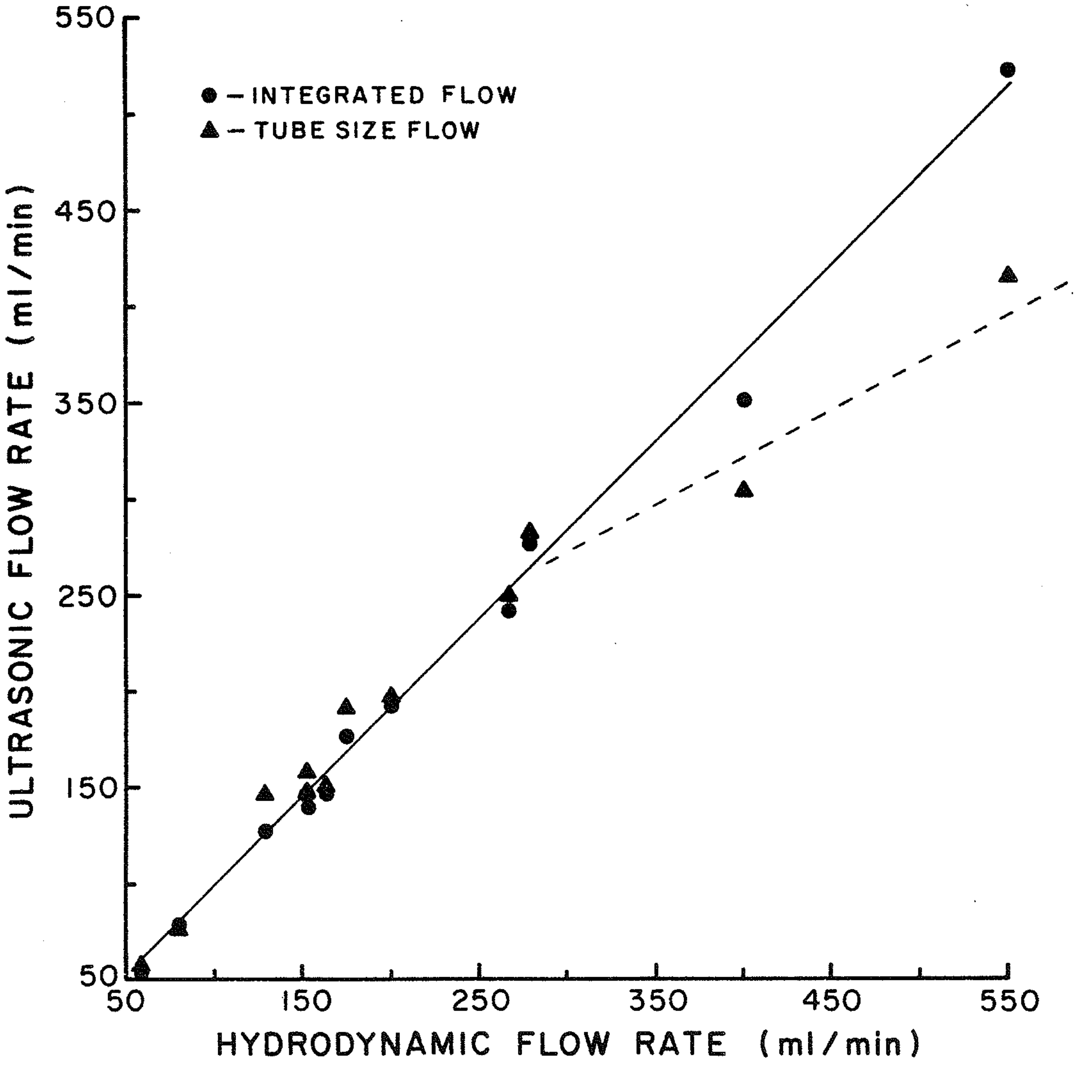

Figure 37 - Ultrasonically measured volume flow estimates versus the hydrodynamic volume flow measurement for twelve volume flow experiments at a 45^{o} measurement angle. The solid line shows the linear regression line for the INTEGRATED volume flow estimates. The dashed curve shows the trend of the TUBE SIZE volume flow estimates at flow rates above 300 ml/min where it deviates from the INTEGRATED estimate.

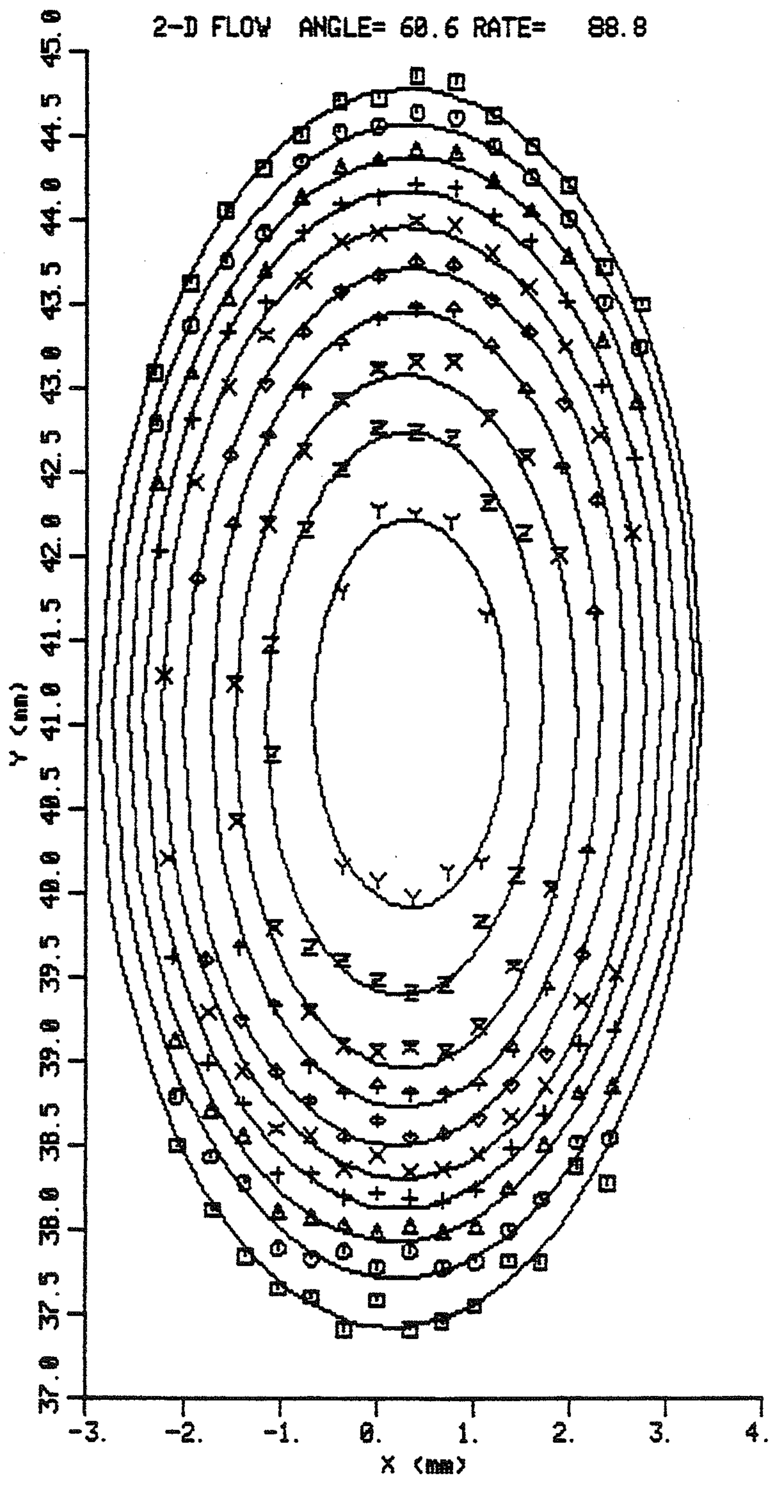

Figure 38 - Constant velocity ellipse data of flowing porcine blood at a measurement angle of 60°. Fourteen scan angles are shown in this data set. No compensation for refraction at the saline-blood interface caused the INTEGRATED flow estimate to be low by 18.9% (see JUL167 data set in Table 12).

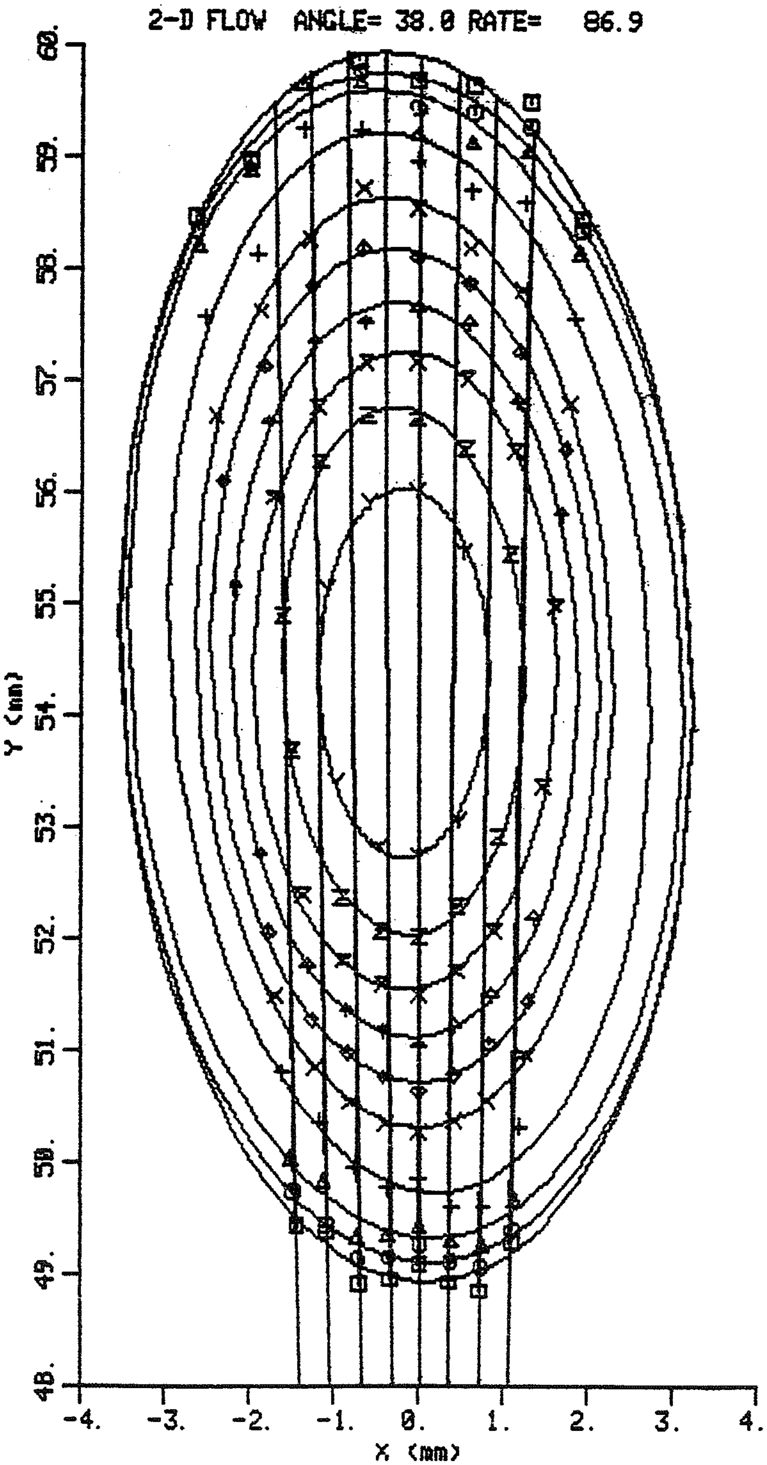

Figure 39 - Constant velocity ellipses resulting from a glycerin volume flow experiment (data set OCT021 in Table 12). The solid straight lines indicate the path of the beam without refraction. The speed of sound inside the tube (c_1) was assumed to be 1.7 mm/µs and c_0 was 1.5 mm/µs.

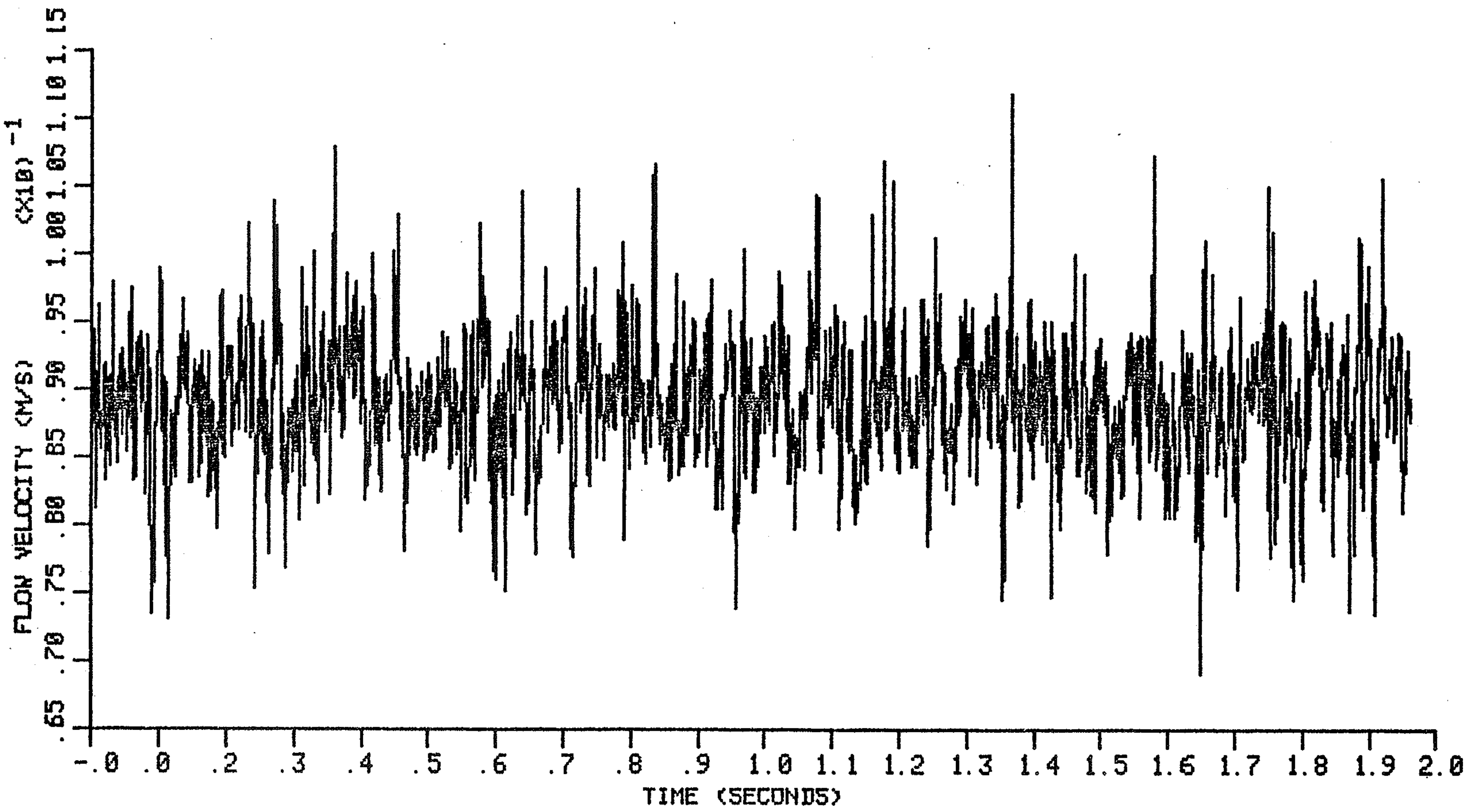

Figure 40 - Optimum axial velocity estimate of constant midstream flow of an aqueous suspension of Sepahdex^R at a measurement angle of 45^o. A total of 6134 velocity estimates are shown. (PRF = 3125 HZ).

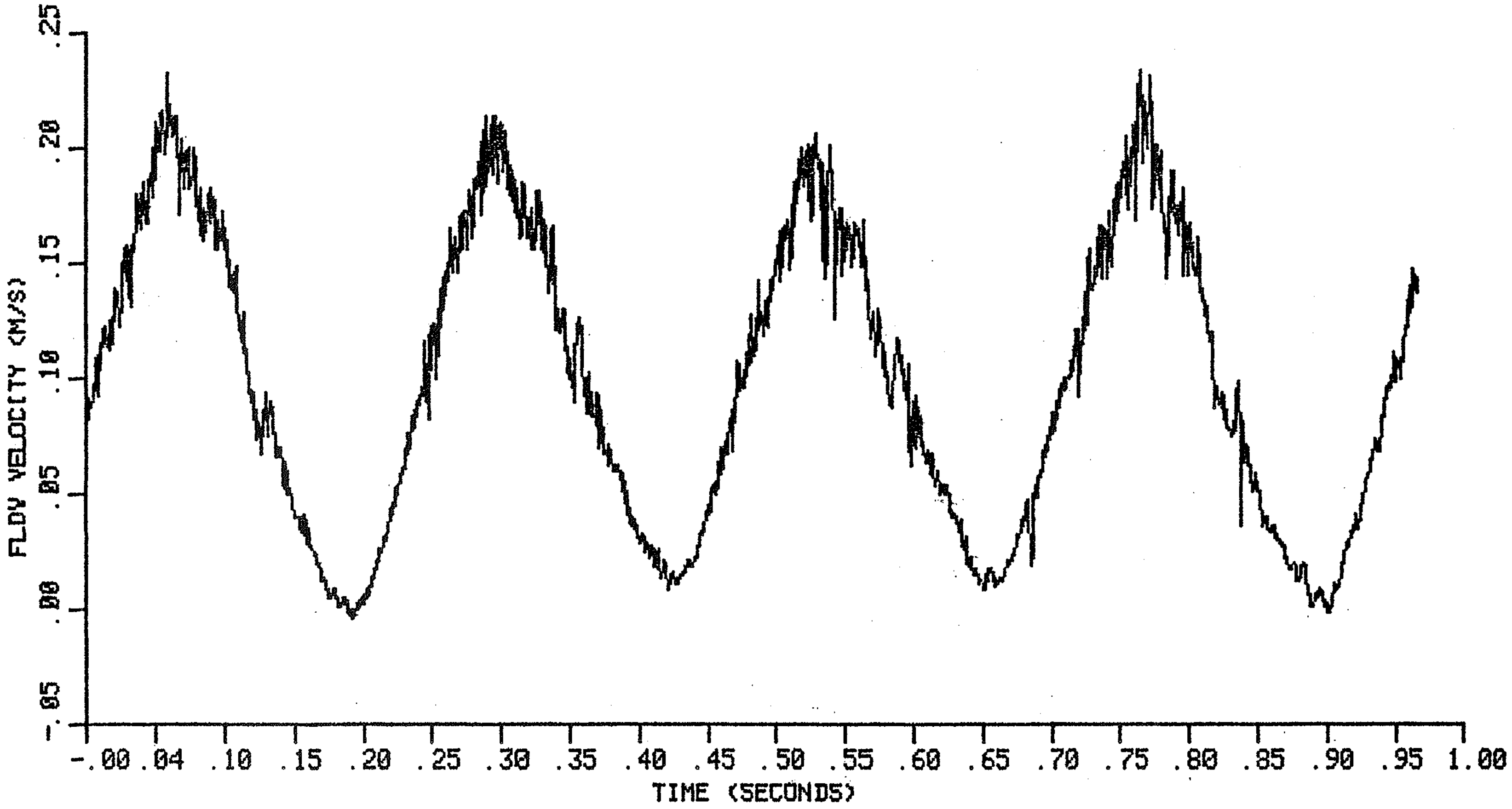

Figure 41 - Optimum axial velocity estimate versus time of pulsatile output of pump at a measurement angle of 45°. A total of 6134 velocity estimates are shown (PRF = 6250 Hz).

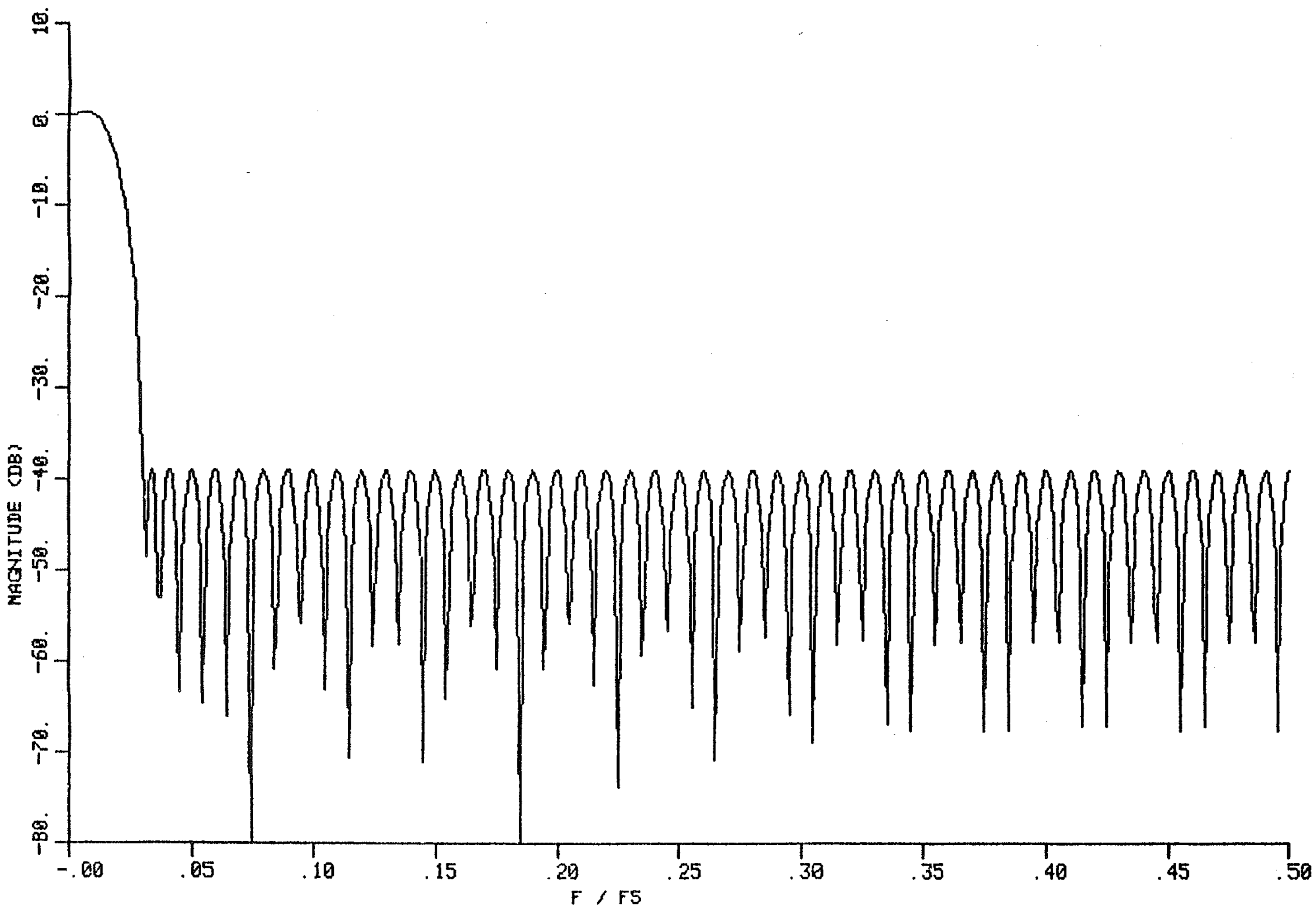

Figure 42 - Lowpass filter magnitude response of 101 point digital FIR filter designed to filter pulsatile flow measurements. The 3 dB cutoff frequency is 47 Hz when a sampling rate of 6250 Hz is used.

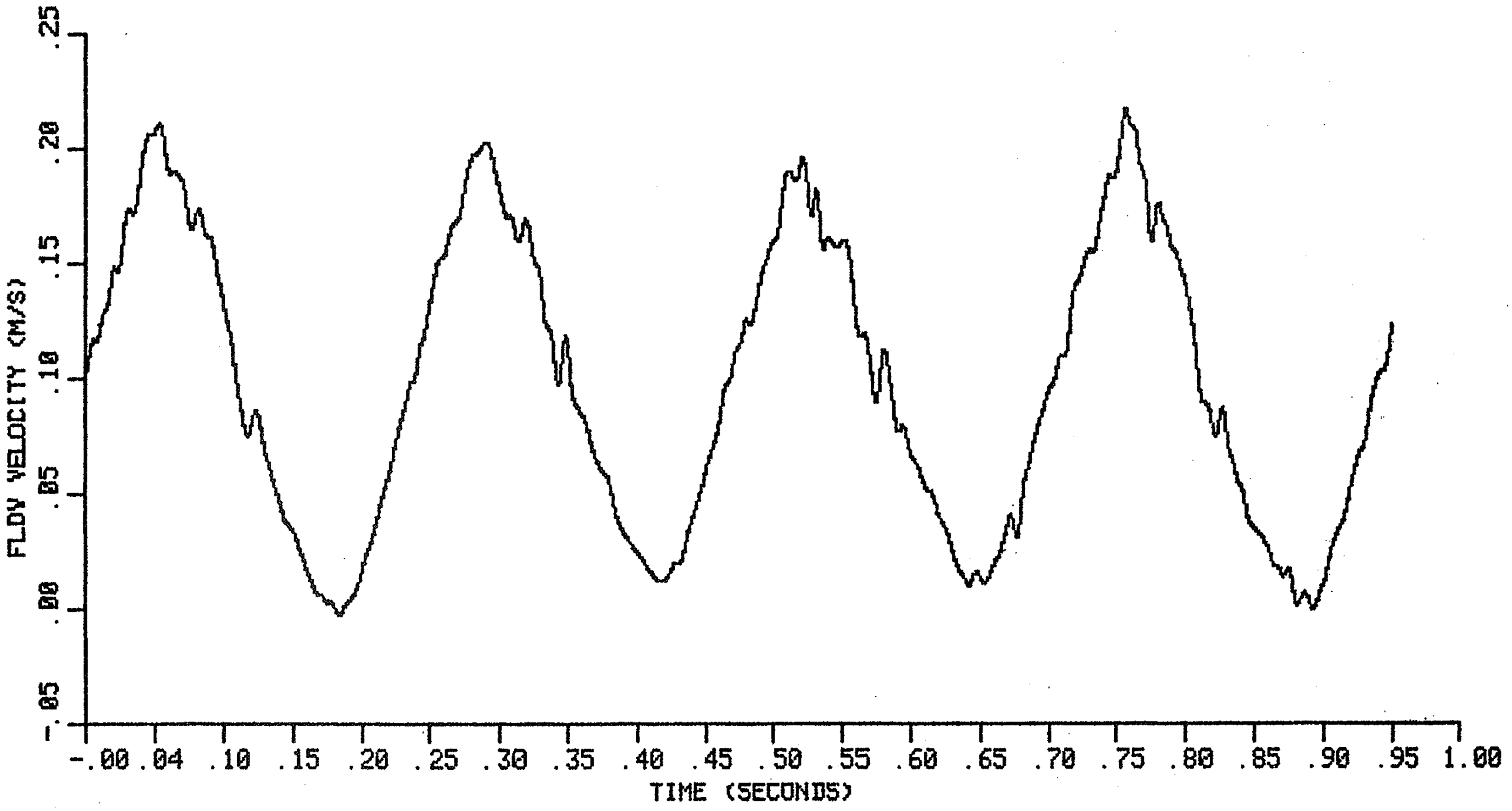

Figure 43 - Lowpass filtered axial velocity estimate versus time. The original axial velocity measurements (shown in Figure 41) were filtered using the filter response shown in Figure 42.

REFERENCES

[1] Hatle, L. and Angelson, B., Doppler Ultrasound in Cardiology: Physical Principles and Clinical Application, Lea and Febiger, Philadelphia, PA, 1982.

[2] Atkinson, P. and Woodcock, J. P., Doppler Ultrasound and Its Use In Clinical Measurement, Academic Press Inc., London, 1982.

[3] Kasai, C., Namekawa, K., Koyano, A., and Omoto, R., Real-Time Two-Dimensional Blood Flow Imaging Using an Autocorrelation Technique. IEEE Transactions on Sonics and Ultrasonics, vol. SU-32, pp. 458-464, 1985.

[4] Brandestini, M., Topflow - A Digital Full-range Doppler Velocity Meter. IEEE Transactions Sonics and Ultrasonics, vol. SU-25, pp. 287-293, 1978.

[5] Brandestini, M., Application of the Phase Detection Principle in a Transcutaneous Velocity Profile Meter. Proceeding 2nd European Congress on Ultrasound in Medicine, pp. 144-152, 1975.

[6] Grandchamp, P. A., A Novel Pulsed Directional Doppler Velocimeter, The Phase-Detection Profilometer. Proceeding 2nd European Congress on Ultrasound in Medicine, pp. 137-143, 1975.

[7] Baker, D. W., Pulsed Ultrasonic Doppler Blood Flow Sensing. IEEE Transactions on Sonics and Ultrasonics, vol. SU-17, pp. 170-185, 1970.

[8] Jethwa, C. P., Kaveh, M., Cooper, G. R., and Saggio, F., Blood Flow Measurements Using Ultrasonic Random Signal Doppler System. IEEE Transactions on Sonics and Ultrasonics, vol. SU-22, pp. 1-11, 1975.

[9] Angelson, B. and Kristoffersen, K., Discrete Time Estimation of the Mean Doppler Frequency in Ultrasonic Blood Velocity Measurements. IEEE Transactions Biomedical Engineering, vol. BME-30, pp. 207-214, 1983.

[10] Angelsen, B., Instantaneous Frequency, Mean Frequency and Variance of Mean Frequency Estimator for Ultrasonic Blood Velocity Doppler Signals. IEEE Transactions Biomedical Engineering, vol. BME-28, pp. 733-741, 1981.

[11] Skolnik, M. I., Radar Handbook, McGraw-Hill, New York, 1970.

[12] Foster, S. G., A Pulsed Ultrasonic Flowmeter Employing Time Domain Methods. Ph.D. Thesis in Electrical Engineering, University of Illinois at Urbana-Champaign, 1984.

[13] Newhouse, V. L., Bendick, P. J., and Varner, L. W., Analysis of Transit Time Effects on Doppler Flow Measurement. IEEE Transactions Biomedical Engineering, vol. BME-23, pp. 381-387, 1976.

[14] Brody, W. R. and Meindl, J. D., Theoretical Analysis of the CW Doppler Ultrasonic Flowmeter. IEEE Transactions Biomedical Engineering, vol. BME-21, pp. 183-192, 1974.

[15] Coghlan, B. A. and Taylor, M. G., Directional Doppler Techniques for Detection of Blood Velocities. Ultrasound in Medicine and Biology, vol. 2, pp. 181-188, 1976.

[16] Johnston, K. W., Maruzzo, B. C., and Cobbold, R. S. C., Doppler Methods for Quantitative Measurement and Localization of Peripheral Arterial Occlusive Disease By Analysis of the Blood Flow Velocity Waveform. Ultrasound in Medicine and Biology, vol. 4, pp. 209-223, 1978.

[17] Berry, S. M., O'Donnell, J. A., and Hobson, R. W., Capabilities and Limitations of Pulsed Doppler Sonography in Caroid Imaging. Journal of Clinical Ultrasound, vol. 8, No. 5, 1980.

[18] Hames, T. K. and Humphries, K. N., Application of Statistical Techniques to Data Obtained from Doppler Ultrasound Examination of the Extracranial Arteries. Ultrasound 82 Proceedings of the Third Meeting of the WFUMB, Pergamon Press, pp. 243-248, 1982.

[19] Campbell, W. B., Skidmore, R., Cole, S. E. A., Baird, R. N., and Woodcock, J. P., Differential Diagnois of Arterial Disease of the Lower Limb Using Doppler Ultrasound. Ultrasound 82 Proceedings of the Third Meeting of the WFUMB, Pergamon Press, pp. 257-262, 1982.

[20] Walton, L., Martin, T. R. P., Collins, M., Sherriff, S. B., and Barber, D. C., An Objective Feature Extraction Technique Applied to the Doppler Waveforms from the Groin: A Prospective Study. Ultrasound 82 Proceedings of the Third Meeting of the WFUMB, Pergamon Press, pp. 263-268, 1982.

[21] Doriot, P. A., Casty, A., Milakara, B., Anliker, M., Bollinger, A., and Siegenthaler, W., Quantitative Analysis of Flow Conditions in Simulated Vessels and Large Human Arteries and Veins by Means of Ultrasound. Proceeding 2nd European Congress on Ultrasound in Medicine, pp. 160-168, 1975.

[22] Dunn, F., Ultrasonic Attenuation Absorption and Velocity in Tissue and Organs. Proceedings First International Symposium on Ultrasonic Tissue Characterization, National Bureau of Standards Publication 453, pp. 21-28, U. S. Government Printing Office, Washington, D. C., 1976.

[23] Bamber, J. C. and Hill, C. R., Ultrasonic Attenuation and Propagation Speed in Mammalian Tissues as a Function of Temperature. Ultrasound in Medicine and Biology, 5, No. 2, pp. 149-157, 1979.

[24] Carstensen, E. L., Absorption of Sound in Tissues. Ultrasonic Tissue Characterization II, M. Linzer, ed., NBS 525, pp. 29-36, 1979.

[25] Dunn, F. and Brady, J. K., Temperature and Frequency Dependence of Ultrasonic Absorption. Proceedings of the 8th International Congress on Acoustics, vol. I, Goldcrest Press, Trowbridge, Wilts., p 366, 1974.

[26] Gammell, P. M., LeCroisette, D. H., and Heyser, R. C., Temperature and Frequency Dependence of Ultrasonic Attenuation in Selected Tissues. Ultrasound in Medicine and Biology, 5, pp. 269-277, 1979.

[27] Goss, S. A., Johnston, R. L., and Dunn, F., Comprehensive Compilation of Empirical Ultrasonic Properties of Mammalian Tissues. Journal of the Acoustical Society of America, 64, No. 2, pp. 423-457, 1978.

[28] Goss, S. A.. Johnston, R. L., and Dunn, F., Compilation of Empirical Ultrasonic Properties of Mammalian Tissues II. Journal of the Acoustical Society of America. 68, No. 1, pp. 93-108, 1980.

[29] Parry, R. J. and Chivers, R. C., Data of the Velocity and Attenuation of Ultrasound in Mammalian Tissues - A Survey. Ultrasonic Tissue Characterization II, M. Linzer, ed., NBS 525, pp. 343-360, 1979.

[30] Shirasaka, T., Sasaki, H., Seo, Y., Inuma, K., and Hongo, H., The Effect of Finite Bandwidth of Ultrasonic Pulse on Pulsed Doppler Frequency Spectrum. Abstracts of the Third Meeting of the WFUMB, paper 534, Pergamon Press, 1982.

[31] Olinger, M. D., Ultrasonic Blood Flow Imaging Using Correlation Processing. Ph.D. Thesis in Electrical Engineering and System Science, Michigan State University, 1981.

[32] Lunt, M. J., Accuracy and Limitations of the Ultrasonic Doppler Blood Velocity Meter and Zero Crossing Detector. Ultrasound in Medicine and Biology, vol. 2, pp. 1-10, 1975.

[33] Gerzberg, L. and Meindl, J. D., Power Spectrum Centroid Detection for Doppler Systems Applications. Ultrasonic Imaging, vol. 2, pp. 232-261, 1980.

[34] Kristoffersen, K. and Angelsen, B., A Comparison Between Mean Frequency Estimators for Multigated Doppler Systems with Serial Signal Processing. IEEE Transactions Biomedical Engineering, vol. BME-32, pp. 645-657, 1985.

[35] Ziemer, R. E. and Tranter, W. H., Principles of Communications, Systems, Modulation, and Noise, Houghton Mifflin Co., Boston, 1976.

[36] Ong, K. H. and Beck, M. S., Slurry Flow Velocity, Concentration and Particle Size Measurement Using Flow Noise and Correlation Techniques, Measurement and Control, vol. 8, pp. 453-461, November 1975.

[37] Helstrom, C. W., Statistical Theory of Signal Detection, Pergamon Press Ltd., Oxford, 1960.

[38] Woodward, P. M., Probability and Information Theory, With Application to Radar, Pergamon Press Ltd.. Oxford, 1953.

[39] Streeter, V. L., Fluid Mechanics, McGraw-Hill, New York, 1971.

[40] Kihuchi, Y., ed., Ultrasonic Transducers, Corona Publishing Co., Ltd., Tokyo, 1969.

[41] Vladimiresscu, A., Newton, A. R., and Pederson, D. C., SPICE Version 2F.1 User's Guide. University of California, Berkeley, CA, 1982.

[42] Embree, P. M., UDAS - Ultrasound Data Acquisition System, Internal BRL Report, University of Illinois at Urbana-Champaign, 1985.

[43] Rabiner, L. R. and Gold, B., Theory and Application of Digital Signal Processing, Prentice-Hall, Inc., Englewood Cliffs, NJ, 1975.

[44] Selfridge, A. R., Approximate Material Properties in Isotropic Materials. IEEE Transactions on Sonics and Ultrasonics, vol. SU-32, No. 3, May 1985.

[45] Walpole, R. E. and Myers, R. H., Probability and Statistics for Engineers and Scientists, MacMillan Publishing Co., New York, 1978.

[46] Carstensen, E. L., Li, K., and Schwan, H. P., Determination of the Acoustic Properties of Blood and its Components. Journal of the Acoustical Society of America. 25, No. 2, pp. 286-289, 1953.

[47] Carstensen, E. L. and Schwan, H. P., Acoustic Properties of Hemoglobin Solutions. Journal of the Acoustical Society of America. 31, No. 3, pp. 305-311, 1959.

[48] Silvey, S. D., Statistical Inference, Halstead Press, 1975.

[49] Knapp, C. H. and Carter, C., The Generalized Correlation Method for Estimation of Time Delay. IEEE Transactions Acoustics, Speech and Signal Processing, vol. ASSP-24, No. 4, pp. 320-327, 1976.

[50] McGill, K. C. and Dorfman, L. J., High-resolution Alignment of Sampled Waveforms. IEEE Transactions Biomedical Engineering, vol. BME-31, No. 6, pp. 462-468, 1984.

[51] Boucher, R. E. and Hassab, J. C., Analysis of Discrete Implementation of Generalized Cross Correlator. IEEE Transactions Acoustics, Speech and Signal Processing, vol. ASSP-29, No. 3, pp. 609-611, 1981.

[52] McClellan, J. H., Parks, T. W., and Rabiner, L. R., A Computer Program for Designing Optimum FIR Linear Phase Digital Filters. IEEE Transactions on Audio and Electroacoustics, AU-21, No. 6, pp. 506-526, 1973.

VITA

Paul Michael Embree was born September 27, 1959, in Reading, Pennsylvania. From 1977 to 1981, he attended Lehigh University in Bethlehem, Pennsylvania and was awarded a Bachelor of Science degree in Electrical Engineering in 1981.

From 1981 to 1986, Mr. Embree attended the University of Illinois at Urbana-Champaign. For the first year he was employed by Bell Telephone Laboratories, and later returned there briefly. He was awarded a Master of Science degree in 1982, and produced a thesis entitled "The Analysis and Performance of a Tunable State Variable Filter Employing Switched Resistor Elements."

From 1983 to 1986, Mr. Embree worked in the Bioacoustics Research Laboratory of the University of Illinois, on his doctoral dissertation and other ultrasonic research.